Correction of the Aberrations of the Eye using Adaptive Optics with Pupil Tracking

by Betul Sahin

Supervisors: Prof. Dr. Chris Dainty and
Fabrice Harms (Imagine Eyes®, Orsay, France)

A thesis submitted in partial fulfilment of the requirements for the degree of Doctor of Philosophy,

Applied Optics Group
School of Physics
National University of Ireland, Galway

August 2011

Abstract

Adaptive optics has long been used in the astronomical telescopes to acquire high resolution images via the real time correction of the rapidly changing wavefront aberrations. Human retinal images also suffer from rapidly changing aberrations due to, for example, eye movements, crystalline lens fluctuations or changes in the tear film. Several research groups in the world have used adaptive optics for different retinal imaging modalities and were able to acquire high resolution images of the human retina revealing the photoreceptor mosaic. Being able to image human retina in high resolution opens a new era in many important fields, such as pharmacological research for retinal diseases, researches in human cognition, nervous system, metabolism and blood stream to name a few. Having such a potential in medicine, there is not an available commercial adaptive optics retinal imaging system for clinical research and practice yet. The reasons are the complexity, cost and poor reliability of the available systems of the research groups. Here in this research our aim was to search a cost effective way of improving the adaptive optics correction of a compact adaptive optics retinal imaging system designed for clinical research. Based on the hypothesis that majority of the changes in the aberrations of the eye are due to eye movements, using the default eye camera that is used for the alignment of the eye in the retinal imaging system, the new method required no extra cost or hardware. It was possible to control the deformable mirror in real time based on pupil tracking measurements and correct for the aberrations of a moving model eye and *in vivo*. As an outcome of this research we showed that pupil tracking which is an indispensable tool for retinal imaging in high resolution can be effectively used as a part of the adaptive optics as a result of the fact that indeed eye movements constitute an important part of the ocular wavefront dynamics.

Acknowledgements

I would like to thank to my supervisors Chris Dainty, Fabrice Harms and Nicolas Chateau of Imagine Eyes giving me the opportunity to work on this project and for providing me with valuable guidance and support generously. I thank my colleagues at Imagine Eyes and its sister company Imagine Optic, for their warm welcome during my three years at their premises in France. I am grateful for the discussions with Xavier Levecq the co-founder of Imagine Optics, for the support of Jerome Lagrange of Imagine Optics who guided me in understanding and modifying the adaptive optics control software and to Barbara Lamory of Imagine Eyes who was responsible for the construction of the adaptive optics retinal camera. I also acknowledge the work of software engineers and intern students at Imagine Eyes (Maurice Navarro, Erwan Revert, Stephaine Berthier and Remi Gillet) who worked on the pupil tracking system, developed and made this research possible.

This research was funded by European Union, 6th Framework, Marie Curie Early Stage Training Studentships, under the project named, HIRESOMI. We are indebted many thanks to Prof. Adrian Podoleanu of the University of Kent, Canterbury, the coordinator of this project.

Contents

Acronyms

RMS Root Mean Square

CCD Charge Coupled Device

FFT Fast Fourier Transform

LED Light Emitting Diode

OLED Organic Light Emitting Diode

SLD Super Luminescent Diode

IM Interaction Matrix

WF$_{Ref}$ The reference measurement of the wavefront aberrations of the eye whose derivative is used in the control algorithm based on pupil tracking

WFPT Loop which incorporates the wavefront sensor and the pupil tracker only

AOPT Loop which incorporates the wavefront sensor, the deformable mirror, the pupil tracker and the control algorithm based on wavefront sensing

WFPTa Loop which incorporates the wavefront sensor, the pupil tracker and the deformable mirror that corrects the aberrations statically

AOPTL1 Loop which incorporates the wavefront sensor, the deformable mirror, the pupil tracker and the control algorithm based on pupil tracking

AOPTL2 Loop which incorporates the wavefront sensor, the deformable mirror, the pupil tracker and the control algorithms based on wavefront sensing and pupil tracking

Preface

This thesis aims to enhance the adaptive optics correction of a compact retinal imaging system designed for clinical research in a cost effective way; to determine if pupil tracking, which required no extra hardware, can be used to correct for the monochromatic ocular aberrations as a part of adaptive optics.

The first chapter of this thesis is an introduction to retinal imaging, ocular aberrations, adaptive optics and pupil tracking. In the second chapter the compact adaptive optics retinal imaging system that was used in the experiments is described (publication 5).

In the third chapter the pupil tracking system is described and its algorithm, performance in terms of accuracy, precision and time resolution was detailed (publications 1-4).

The fourth chapter introduces the adaptive optics control algorithms based on wavefront sensing and pupil tracking, then the calibration procedure, results of the simulations, and the first experiments done to correct for the aberrations of a static model eye were given (publications 6-8).

The sixth chapter first describes the software developed to control the adaptive optics instrumentation including pupil tracking and gives the results of real time corrections using both pupil tracking and wavefront sensing for a moving model eye and *in vivo* (publications 9-11). Finally the fifth chapter gives a discussion of the possible applications, improvements of the method and the future prospects.

Publications

1. B. Sahin, F. Harms and S. Berthier. Pupil tracking system for enhanced retinal imaging with adaptive optics. 1^{st} HIRESOMI Workshop, Porto, Portugal, October 2007.

2. B. Sahin, F. Harms, B. Lamory, *et al.* A pupil tracking system for adaptive optics retinal imaging. Proc. SPIE, Vol. 6991 (2008)

3. B. Lamory, B. Sahin, F. Harms, S. Berthier. Performance assessment of a pupil tracking system for adaptive optics. ARVO, Fort Lauderdale, Florida, USA, May 2008.

4. B. Sahin, F. Harms, B. Lamory. Performance assessment of a pupil tracking system for adaptive optics retinal imaging. In 1^{st} *Canterbury Workshop on Adaptive Optics and Retinal Imaging*, Proc. SPIE, Vol. 7139 (2008).

5. B. Sahin, F. Harms, B. Lamory. A new adaptive optics flood illumination retinal imaging system. EOS Annual Meeting, Paris, France, 29 September-2 October 2008.

6. B. Sahin, F. Harms, B. Lamory, *et al.* Evaluation of a coupling algorithm between a pupil tracker and an adaptive optics retinal imaging system. 7^{th} Workshop on Adaptive Optics in Industry and Medicine, Shatura, Russia, 20-(09.

7. B. Sahin, F. Harms, B. Lamory, *et al.* Evaluation of a coupling algorithm between a pupil tracker and an adaptive optics retinal imaging system. 3^{rd} HIRESOMI Workshop, Galway, Ireland, 13-15 July, 2009.

8. B. Sahin, F. Harms, B. Lamory, *et al.* Improved adaptive optics control system using pupil tracking for high-resolution retinal imaging. ARVO, Fort Lauderdale, Florida, USA, May 2010.

9. B. Sahin, F. Harms, B. Lamory, *et al.* Correction of the eyes aberrations with adaptive optics and pupil tracking. 4^{th} HIRESOMI Workshop, Paris, France, 15-16 July 2010.

10. B. Sahin, F. Harms, B. Lamory, *et al.* Correction of the eye's aberrations with adaptive optics and pupil tracking. EMVPO 2010, Stockholm, Sweden, 22-24 August 2010.

11. B. Sahin, B. Lamory, Xavier Levecq, *et al.* Retinal imaging system with adaptive optics enhanced with pupil tracking. In *BIOS*, Proc. SPIE, Vol. 7885 (2011).

12. A. Garcia-Rissmann, C. Kulcsar, H-F. Raynoud, Y. El Mrabet, B. Sahin and B. Lamory. Adaptive prediction of human eye pupil position and effects on wavefront errors. In *BIOS*, Proc. SPIE, Vol. 7885 (2011).

بسم الله الرحمن الرحيم

Chapter 1

Introduction

In this chapter, we first discuss the challenges of retinal imaging at high resolution, then, adaptive optics and its applications in ophthalmology with the current handicaps, and finally the reasons for using pupil tracking.

1.1 High resolution imaging of the human retina

The human eye has the versatility of being an optical device made up of living cells; proteins, connective tissue and yet transparent [1]. It is a rather simple optical system with exceptional functionality. Although, there are many examples of vision in nature that are better in terms of different functionalities, the human eye best responds to the needs of the human beings in a vast variety of conditions as a whole.

Electromagnetic radiation has long been used as a medical imaging tool for different parts of the human body as long as the penetration through the tissue permits. Visible and infrared light being harmless, cannot penetrate the body tissue more than a few millimetres except for the case of the eye. The back of the eye which constitutes the veins and the arteries and the retina as an extension of the brain, is easily accessible *in vivo* using visible light. Imaging the back of the eye through the optics of the eye in high resolution has a lot of applications yet to be discovered; there is no other example of an imaging tool that can reveal

metabolism and blood stream or nerve cells intact and *in vivo* in such a way [2, 3, 4].

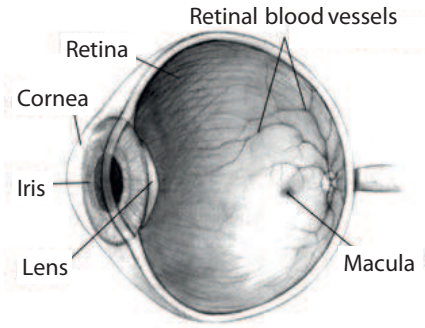

Figure 1.1: The eye; optics and the retina at the back of the eye (courtesy of *National Eye Institute, USA*).

The retina at the back of the eye is a complex multilayered structure, see Figure 1.1. Refracted by first the cornea and then the crystalline lens, the stream of photons crosses the vitreous body and proceeds through the various layers of the retina until it reaches the segment of photoreceptor cells; rods and cones. The photons that are absorbed by the visual pigments in the photoreceptor cells trigger a chain of events employing the neural network and the brain and are perceived as vision. The remaining photons which are not absorbed and backscattered, provide the means of imaging the layers of the eye, especially the photoreceptors, in vivo and non-invasively [5].

Helmholtz first developed the tool to view the retina and named it as the ophthalmoscope in 1851. The main problem in seeing the back of the living eye was that its reflectance is only 0.1 to 10 % depending on the wavelength and the pupil restricts the amount of light that can exit the eye by another factor of a hundred [6]. In 1979 Robert Webb developed the scanning laser ophthalmoscope[1] which provided higher contrast and sensitivity and in addition the ability to view different layers of the retina with the use of a confocal pinhole. After that with the advent of optical coherence tomography[2] axial resolutions as high as a few micrometers

[1] uses a confocal pinhole, horizontal and vertical mirrors to scan a specific region of the retina

[2] interferometric technique to strip off the scattered light from the reflected, for high signal to noise ratio

in vivo was achieved [6]. The tools above provided good axial resolution but a low transverse resolution. The microscopic structures of the retina, *e.g.*, photoreceptor cells, were far away from being seen. For this goal to be achieved it was necessary to measure the higher order aberrations of the eye and correct them [6].

Astrophysics searches for the reality of the outer universe in macro scale, where retinal imaging looks into our inner universe to the micro scale, both using similar tools and facing similar problems. Therefore improvements in retinal imaging and astrophysics being parallel in the last century was not a coincidence: images of the universe became more and more clear in the last century and so did the retinal images. Adaptive optics was the latest breakthrough that removed some of the blur from both astronomical and retinal images, see Figure 1.2.

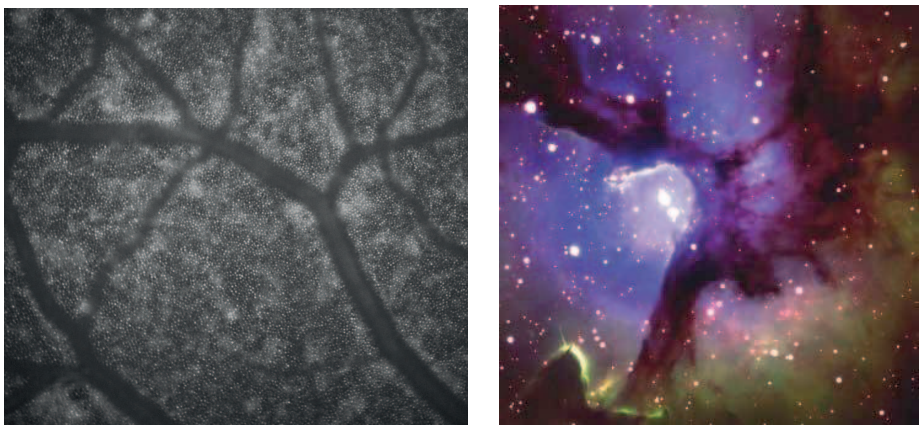

Figure 1.2: Looking up to the sky underneath a tree in starry night or human cone photoreceptors as the blood vessels are superimposed on them (left)(courtesy of Imagine Eyes), central region of the Trifid Nebula from the Gemini North 8-meter Telescope on Mauna Kea, Hawaii (right) [7], where both images were acquired with the help of adaptive optics.

Similar to the astronomical images, the retinal images suffer from blur caused by non corrected optical aberrations. Those aberrations change over time and a static correction using refractive optics is not possible. The changes in the aberrations either have to be predicted (if possible) or have to be measured and corrected for dynamically. Different dynamics govern the changes in the aberrations in the atmosphere and in the eye, therefore adaptive optics technologies for them have slightly varied; the adaptive optics for retinal imaging uses components that are

medically safe and suitable for clinical use and that can correct for larger aberrations, while astronomy uses faster components and a guide star [8].

The fainter constituents of the retina such as rod photoreceptor cells and ganglion cells are harder to image; scattering and speckle have to be overcome, the techniques of which are not the subject of this thesis [9, 10].

In the following sections the ocular higher order aberrations and adaptive optics for vision science will be discussed.

1.2 Higher order aberrations of the eye

Vision is accomplished as a coordination of the muscles, the (adaptive) optics of the eye and the nerve cells in the retina. The refractive elements of the eye, the cornea and the crystalline lens, are not rotationally symmetric [11]. Furthermore the optical axis of these elements are not the visual axis that is used for central vision; the fovea, where the acute vision takes place, is typically 5° away from the optical axis. Any man made optical device arranged this way would result in images that suffer from serious blur.

This peculiar and not yet fully understood arrangement indicates an adaptive aberration compensation system, because our vision is much more acute than it is expected under these conditions [12]. This is probably due to a compensation mechanism in the nerve system and in between the optical elements. The most well known example of adaptive compensation in the eye is the accommodation ability of the lens for viewing targets from infinity to $\sim$ 10 cm (for the young adult eye). Indeed in the case of defocus, the gradient index crystalline lens functions as a refractive phase corrector and compensates for the wavefront error mechanism of which is an active research area. It would be beneficial if such a mechanism existed to compensate for the other higher order aberrations.

Clinicians routinely correct refractive errors of defocus and astigmatism by spectacles. More complex and subtle higher order aberrations were ignored until

refractive surgery and corneal shaping came into practice [13]. Among the methods to measure the higher order aberrations of the eye objectively, Shack-Hartmann, whose principles will be detailed in the Section 1.3, is the most used one.

First measurements of the high order aberrations of the eye using a Shack-Hartmann wavefront sensor was made by Liang *et al.* [14]. In their paper they highlighted that the magnitude of the diffraction effects and the higher order aberrations; the two factors that degrade the resolution of the vision, are related to the pupil size differently. A large pupil does not mean a diffraction limited image because it is accompanied by an increase in high order aberrations which degrade image quality significantly: as a result in humans a pupil of $\sim$2.4 mm pupil is ideal to resolve small details. They observed that both eyes have the same pattern of high order aberrations and suggested that therefore the existence of high order aberrations may not be a coincidence [14].

1.2.1 Representation of ocular aberrations

Aberration in an optical system can be defined as the optical deviation of a wavefront from a reference plane or spherical wavefront, and as a result, the failure of the system to produce an ideal image [15, 6]. There are two common methods of representing ocular aberrations in a two dimensional surface; discrete or analytical. The two methods have their strengths and weaknesses depending on the application. The discrete representation gives a topographic view; it is rough and its resolution depends on the data points. On the other hand, an analytical representation has theoretically infinite resolution and the magnitude of each ocular aberration can be derived independently. Also being easier to compute and manipulate, analytical functions were found to be the most convenient way of representing the ocular aberrations, especially the orthonormal Zernike polynomials [16]. Using Zernike polynomials, the aberrations may be decomposed into a set of basis functions using which any two dimensional function $W(\rho, \theta)$ can be

represented with an infinite set without an error,

$$W(\rho,\theta) = \sum_{i=0}^{\infty} c_i Z_i(\rho,\theta), \tag{1.1}$$

where ρ and θ are variables in polar coordinates and c_i is the expansion coefficient of the i^{th} basis function Z_i. Since it is not possible to calculate all the coefficients up to infinity, a convenient number of coefficients, J, are chosen depending on the aberrations and the application.

Zernike polynomials can be written either in single-index, Z_i, or double-index, Z_n^m, form where m and n represent radial and azimuthal order respectively. Table 1.1 shows the Zernike polynomials and the aberrations that they represent up to 4^{th} radial order.

i	n	m	Zernike Polynomials	Name
0	0	0	1	piston
1	1	-1	$2\rho sin\theta$	y-tilt
2	1	1	$2\rho cos\theta$	x-tilt
3	2	-2	$\sqrt{6}\rho^2 sin2\theta$	y-astigmatism
4	2	0	$\sqrt{3}(\rho^2-1)$	defocus
5	2	2	$\sqrt{6}\rho^2 cos2\theta$	x-astigmatism
6	3	-3	$\sqrt{8}\rho^3 sin3\theta$	y-trefoil
7	3	-1	$\sqrt{8}(\rho^3-2\rho)sin\theta$	y-coma
8	3	1	$\sqrt{8}(\rho^3-2\rho)cos\theta$	x-coma
9	3	3	$\sqrt{8}\rho^3 cos3\theta$	x-trefoil
10	4	-4	$\sqrt{10}\rho^4 sin4\theta$	y-quadrafoil
11	4	-2	$\sqrt{10}(4\rho^4-3\rho^2)sin2\theta)$	y-secondary astigmatism
12	4	0	$\sqrt{5}(6\rho^4-6\rho^2+1)$	spherical aberration
13	4	2	$\sqrt{10}(4\rho^4-3\rho^2)cos2\theta)$	x-secondary astigmatism
14	4	4	$\sqrt{10}\rho^4 cos4\theta$	x-quadrafoil

Table 1.1: The Zernike polynomials up to $n = 4^{th}$ radial order where i and m are single-index number and azimuthal frequency respectively.

In this context the first three radial orders, n=(0, 1, 2), are called low order aberrations and radial orders three and above are called higher order aberrations [17].

The orthonormality, *i.e.*, the orthogonality and normality of the Zernike polynomials implies that, first whatever J, the chosen number of coefficients is, the

value of the i^{th} coefficient of the expansion does not change which means that any number of additional expansion terms can be added without an impact on those already computed. Second, the entire value of any wavefront is fixed and is equal to the coefficient c_0, third, as the coefficients do not depend on the chosen number of expansion J, as the J increases, low order terms are balanced with high order terms, fourth, all the polynomials except the first one have zero mean, and finally, since the mean of each polynomial is zero, RMS of the wavefront is equal to its standard deviation and the total wavefront RMS can be calculated by,

$$\sigma = \sqrt{c_1^2 + c_2^2 + \ldots + c_J^2} \tag{1.2}$$

where J is the number of polynomials used in the Zernike expansion and c_i is the i^{th} coefficient [18].

Since there were many types of measurement systems and representation methods, the Optical Society of America published a standard for reporting ocular aberrations [19], although there are still ambiguities such as for example how many Zernike orders are sufficient to represent ocular aberrations [20]. The Zernike polynomial representation is useful but is not efficient in a number of cases, *e.g.*, for a non-circular pupil [17]. The impact of non-circular pupils in our measurements will be discussed in the results chapter where both zonal (discrete) and modal (Zernike) reconstruction was used to calculate the wavefront RMS. Furthermore, Zhu *et al.* [21] stated that Zernikes were not sufficient to describe the irregular surface of the cornea, and Smolek *et al.* [20] were concerned with the Zernike fitting error due to the aberration balancing property of the Zernikes as discussed above; for instance, a spherical aberration may induce a negative defocus and result in an underestimation of the defocus of the eye.

1.2.2 Measurements of higher order ocular aberrations

Higher-order aberrations in healthy eyes were measured by different authors using Shack-Hartman sensors or laser ray tracing[3] [22, 23, 24]. One of the motivations was that if the normal magnitudes of higher order aberrations for healthy eyes were known, this would help differentiate healthy and diseased states of the eye.

A good agreement was found in types and magnitudes of higher order aberrations seen among the population although it has to be taken into account that the measurements were done with different pupil sizes and light sources [25]. No significant relationship was found between higher order aberrations and lower refractive errors, *i.e.*, myopia and hyperopia [26, 27]. It was found that the higher order aberrations had similar magnitudes and tended to have zero mean statistically except for spherical aberration which was also found to be less in Asians [27]. A study made among subjects with keratoconus (a disease that results in corneal shape distortions), showed that they can be differentiated from normal eyes at an early stage as because of the shift of the corneal cone they have distinctive coma like aberrations [28].

The aberration profile of the cornea can be estimated from its shape based on the reflections of series of concentric rings from the cornea by a corneal topographer. The higher order aberrations solely due to the lens of the eye was estimated by subtracting the corneal aberration measurements from the total aberration measurements of the eye done by a Shack-Hartmann wavefront sensing or by laser ray tracing. The results were surprising; the cornea and the lens had opposite signs of spherical aberration and coma. It was suggested that the lens compensated for the aberrations caused by cornea and both formed an aplanatic optical system [26, 29, 30]. Salmon *et al.* [13] explained this phenomenon differently by the angular misalignment between the line of sight and the pupillary axis[4] which is used in the corneal topography measurements.

[3] a set of laser pencils is delivered in a sequence; in the presence of aberrations the spots are displaced from their reference positions

[4] a line perpendicular to the surface of the cornea passing through the center of the pupil

Any objective ocular aberration measurement method uses the light that passes through the optical system twice; first the light is sent to the retina, then the reflected back light is used to estimate ocular aberrations. The error due to this double pass is ignored assuming that the retina is not a mirror but is a perfect diffuser and therefore the second pass is independent from the first pass (also a narrow input beam is used) [31, 32]. The accuracy of aberration measurements are also confined by the anisoplanatism (i.e., being spatially variant) of the aberrations of the eye [8]. The beacon of wavefront sensing light reflecting back from the retina is confined to a field which does not fully represent the aberrations in a wide field. The isoplanatic patch of the eye in which wavefront measurements are accepted to be accurate was measured to be the central $\sim$2 degrees [33, 34, 35, 36]. Another factor that causes error in wavefront measurements is the scatter and the speckle from different layers of the retina increasing by the visual field and by age that decrease the contrast of for example Shack-Hartmann images [37, 9].

In the course of this thesis we will be discussing the monochromatic aberrations of the eye. There are also chromatic aberrations which degrade the retinal image: when a polychromatic light source is used, several monochromatic images at different wavelengths are superimposed on the image affected by the eye's chromatic difference of defocus [32]. Aphakic eyes (i.e., the physiological eye that has its natural lens removed) showed improvements in vision when intraocular lenses were designed to correct for achromatic aberrations [38]. In the retinal imaging system achromatizing lenses are used.

Another motivation for the measurement of higher order aberrations among the population was to achieve super acuity by correcting the higher order aberrations. This was not found feasible, because it was found that aberrations were small across central 2 mm diameter of the pupil and increased rapidly towards the edge of the dilated pupil; in the day vision where the pupil has $\sim$ 3 mm diameter the high order aberrations had little or no effect [39].

1.2.3 Dynamics of the higher order aberrations

Higher order aberrations are usually attributed to the shape and position of the lens and the surface of the cornea [40]. There is not a single high order aberration profile of the eye; being a living system, optics of the eye is under the effect of countless factors. To name a few, firstly, measured aberrations change due to eye movements. Second, the crystalline lens fluctuation is the reason for an important part of the changes in defocus and high order aberrations. Then comes the tear film, a three layered structure comprised of lipids, water and mucus, which covers the eye's outer surface, which thins due to evaporation and eventually breaks up followed by a blink [41]. The changes in ocular aberrations due to the tear film was reported to constitute 4 - 28% of the total aberration changes [42]. Leahy *et al.* [43] measured the blink interval to be 250 ms but reported that the transition interval of the blink which constitutes the tear film break-up, the eye movement, the blink and finally the tear film build-up lasted up to a second or more.

The higher order aberration profile of the eye is not the same over the visual field: they are found to be higher in the periphery. However, the periphery of the eye is very different than the macula[5]; there are less cones and they have increasingly larger diameters and therefore the resolution is already low [44]. Pressure of the eye's muscles as we change our gaze and even the eyelid pressure changes the high order aberrations of the eye [45].

The bandwidth of the changes in the aberrations were found to be up to 70 Hz, as measured by a 300 Hz bandwidth wavefront sensor [46], which is reasonable considering high frequency components of the eye movements are at $\sim 88 \pm 4.5$ Hz [47]. Like all the physiological data, ocular aberration time series are chaotic and non-stationary, having a varying frequency content. In addition to those it is not possible to do data recordings for sufficiently long times as a result of which power spectral analysis has difficulty revealing the true nature of the data.

Iskander *et al.* [48] introduced time-frequency analysis which demonstrated

[5] $\sim$ 5 mm diameter area in the retina responsible from acute vision, also includes fovea of ~ 1.5 mm and foveola of ~ 0.35 mm diameter

the change of frequency content as a function of time and its relation with the cardiopulmonary system. Hampson *et al.* [49] confirmed that there are more than one mechanism contributing to the aberration dynamics of the eye and some of them are common or there is a nonlinear relationship between them after, a coherence function analysis was used to determine the common frequency components between the aberrations within subjects. Hampson *et al.* [50] also recently proposed using wavelet based fractal analysis which is a relatively new technique and confirmed the multifractal (i.e., having repeating self similarity at different scales) and antipersistant nature of the ocular dynamics, the latter of which means that the time series tends not to continue in the same direction but turns back on itself giving a less smooth signal.

1.3 Adaptive optics for retinal imaging

The technique of compensation for the changing aberrations in an optical system dynamically with the help of relevant hardware and software is called adaptive optics. The first static correction of the high order aberrations of the eye with a deformable mirror and a wavefront sensor was made by Liang *et al.* [51]. This was followed by dynamic corrections which resulted in a greatly improved resolution in retinal images [52, 53, 54].

An adaptive optics system for retinal imaging is made up of a wavefront sensor, a wavefront corrector and a control algorithm, in addition a light source for wavefront sensing, optical elements for conjugation between the components and other optical elements where necessary, see Figure 1.3.

The wavefront sensor measures the aberrations of the incoming wavefront and the wavefront corrector reshapes it according to the commands calculated by the control algorithm based on wavefront sensor measurements. The loop is iterative and the initially aberrated wavefront approaches a plane wavefront after several iterations.

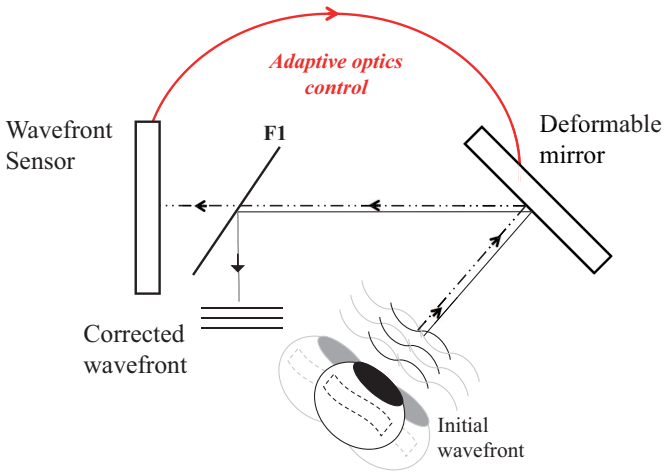

Figure 1.3: Schematics of an adaptive optics system for retinal imaging where the light beams for wavefront sensing and imaging that are reflected off the retina were represented by dashed and solid lines respectively and F1 is a short pass or long pass filter. The aberrated wavefront is reflected from the initially plane deformable mirror, then the wavefront sensor measures the aberrations and the control algorithm calculates the commands for the desired shape and the mirror reshapes the imaging beam (optics necessary to conjugate the wavefront sensor and the deformable mirror to the eye's pupil are not shown for simplicity).

Among the available sensing methods, the Shack-Hartmann technique is the most frequently used one in ocular adaptive optics. It is based on the measurements of the local wavefront slopes using a two dimensional lenslet array, see Figure 1.4. The dynamic range of aberration measurements, θ_{max} and the sensitivity of the

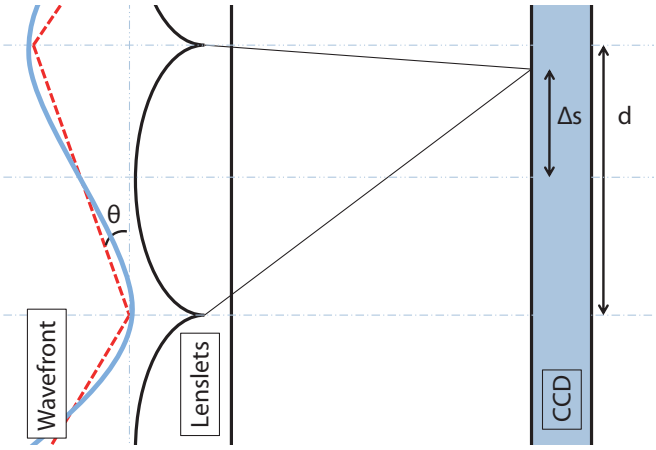

Figure 1.4: Incident wavefront on the lenslet array is evaluated locally where d is the diameter of the lenslets. The local wavefront which is tilted by θ is focused at a point Δs away from the optical axis of the lenslet on the face of the CCD (local slopes of the wavefront are exaggerated.)

measurements, θ_{min} are given by the equations below,

$$\theta_{max} = \frac{\Delta s_{max}}{F} = \frac{d/2}{F}, \tag{1.3}$$

$$\theta_{min} = \frac{\Delta s_{min}}{F}, \tag{1.4}$$

where F is the focal length of the lenslets, d is the diameter of the lenslets and Δs_{min} depends on the pixel size and noise characteristics of the CCD camera. A lenslet array with smaller focal length will result in a larger dynamic range with the cost of a decrease in the sensitivity. The number of lenslets plays an important role in the estimation of the wavefront; a large number of lenslets means a better resolution but requires more light returning from the retina as the total power will be shared over all lenslets, and more time for calculations [55].

In their paper Moreno-Bariusso *et al.* [56] compared three methods that are used to measure the ocular aberrations: laser ray tracing, the spatially resolved refractometer, and the Shack-Hartmann sensor. Among those the laser ray tracing and Shack-Hartmann sensor are objective and the spatially resolved refractometer, which is a psychophysical method, is subjective. They demonstrated experimentally the equivalence of the three methods, underlining their advantages for different applications. In the laser ray tracing method which is sequential, the entire area of the CCD is used for each spot. On the other hand, in Shack-Hartmann sensing all the spots are acquired at once, which is a source of error for large aberrations. Laser ray tracing is too slow to take part in the correction of rapidly changing aberrations and the spatially resolved refractometer, which is based on the response of the subject at each retinal spot, is not applicable, as a result the Shack-Hartmann sensing is the preferred choice for the ocular adaptive optics applications. It has to be emphasized that all of the three methods depend on the reflective properties of the retina and work ideally with healthy human eyes.

Wavefront sensors are useful but not obligatory in all adaptive optics systems. In the case of laser systems, microscopes [57], air turbulence, heat or specimen

induced wavefront aberrations in the optical path or biological imaging where photo bleaching, photo toxicity, time resolution and scattering are limiting factors, it is preferred to not to use a wavefront sensor [58, 59]. The aberration correction is performed by adapting the wavefront corrector such that a certain performance metric (*e.g.*, the light intensity measurement or the sharpness of the image) reaches its maximum in the absence of the aberrations [60].

In contrast to wavefront sensors, a wavefront corrector is obligatory in all adaptive optics systems. The two main types of wavefront correctors are first, ones based on refractive properties of the material, *e.g.*, liquid crystal phase modulators (and human eye crystalline lens) and second, ones based on reflection, *i.e.*, the deformable mirrors [61]. Liquid crystal phase modulators have high resolution but require polarized light, have moderate absorption, a relatively slow response time and chromatic aberration affects (when they are used in phase-wrapping mode) [62, 63].

Deformable mirrors can be segmented or continuous surface where because the spacing between the segments is a source of error, continuous surface mirrors are the preferred choice both in astronomy and ocular applications. Membrane deformable mirrors can be based on electric or magnetic force [64]. Modes of the membrane mirrors depend on the reflective surface properties and number of actuators and any surface represented as a linear combination of these modes will be perfectly produced by adequate commands [62]. More than one deformable mirror can be used in an adaptive optics system; optically conjugated to different altitudes in the atmosphere as used in the astronomy [8] or conjugated to the eye's pupil, sharing the low and high order aberrations; *i.e.*, woofer and tweeter [65].

Although not dynamic and limited by the accommodative state and visual field of the eye, a (custom made) phase plate can also be used as a wavefront corrector and it is claimed that up to 80% of the aberrations can be compensated [66]. Another type of wavefront corrector that has to be mentioned which is still

in development is ferrofluid[6] mirrors which can be reshaped via application of a magnetic field [67]. The ferrofluid mirrors are constrained to remain horizontal but can provide several tens of microns deformation. They work at low frequencies (10 Hz) at the moment and high reflectivity can be achieved using silver nanoparticles [68].

Adaptive optics has been integrated into many imaging modalities such as microscopy [69], photoacoustic imaging [70], fluorescence imaging [71] as well as flood illumination fundus cameras, scanning laser ophthalmoscopes, optical coherence tomography systems, and increased the resolution and signal to noise ratio significantly. In retinal imaging, with the resolutions reached it is possible to image photoreceptor morphology and function in three dimensions, vessel networks and blood flow in the retina, weakly scattering cellular structures *e.g.*, ganglion cells, retinal pigment epithelium cells [72, 73, 74, 75, 76, 77, 78, 79]. A visual simulator also is an application of ocular adaptive optics, using which it is possible to generate desired aberrations and do functional vision tests [80, 81].

After the higher order aberrations are corrected for, among the imaging modalities, it is acknowledged that speed of the image exposure is the key factor to acquire high resolution images because images suffer from motion blur due to eye movements [82, 83]. Trained and well fixating eyes give better results even though the head of the subject is secured using a chinrest or a bite bar. Fixational eye movements have to be compensated for either by predicting, or by measuring, or by being faster than them during image exposure [78, 82, 83].

1.4 Fixational eye movements

Eye movements are due to the action of a group of six muscles; four of them are responsible for four directions, up, down, right and left, the remaining two are oblique and generate torsion, see Figure 1.5.

Our eyes are never still even during fixation because, 'the visual system has a

[6] nanoscale ferromagnetic particles suspended in a carrier liquid

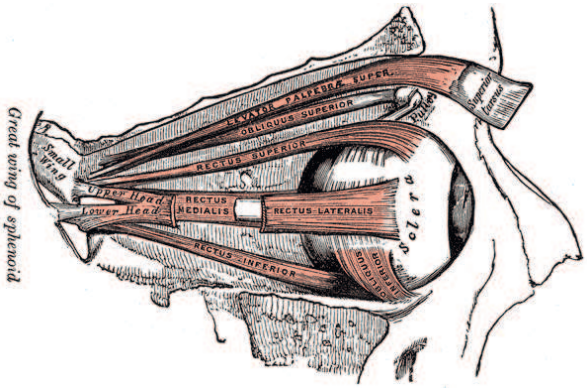

Figure 1.5: The eye and the six main muscles that are responsible for movements to four main directions and torsion (courtesy of *fullwiki.org*).

built in paradox - we must fix our gaze to inspect the details but if we were able to fixate perfectly the entire world would fade from view' [84]. In spite of this continuous jittery and restless imaging, we do not even notice that our eyes are moving; if there was not a compensation for eye movements we would see a blurred scene which is the case for a photograph taken by a shaking CCD camera.

Neurologists explain the reason for this continuous motion by neural adaptation; eye movements during fixation are necessary to overcome loss of vision because steady illumination produces weak neural responses where abrupt changes in illumination across space and time generate strong responses [84]. Another advantage of eye movements is that by this way, rather than devoting all resources to processing it all, the visual system inspects small portions of the visual world in a rapid sequence. Another important function of the eye movements is their averaging of the light over a wide field, reducing the risk of retinal damage under strong illumination [85]. Nevertheless eye movements may also serve for the adaptive compensation of the aberrations in the eye as it was observed that peripheral aberrations induce accommodative response [86]. During fixation multiple copies of the object on the retina are created by the eye movements [87] spanning a field of view that might be necessary to sense the aberrations in a wide field, the simplest of which is the defocus. Some studies showed high prevalence of myopia in certain occupational groups [88] and perhaps a relationship between eye movements and

the process of emmetropization[7] would be discovered in the close future .

Three main types of eye movements are agreed to occur in humans during visual fixation: tremor, drifts and micro saccades [84], see Figure 1.6.

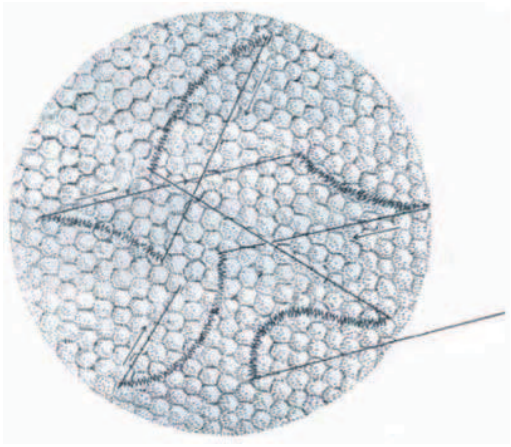

Figure 1.6: Fixational eye movements carry the image across the retinal photoreceptors (50 μm diameter patch of the fovea shown here). High-frequency tremor is superimposed on slow drifts (curved lines). Micro saccades are fast jerk-like movements, which generally bring the image back towards the centre of vision (straight lines)(courtesy of Prichard *et al.*) [89].

Tremor is a wavelike motion of the eyes at $\sim 88 \pm 5$ Hz and is generally thought to be independent in the two eyes [47]. Tremor amplitudes are approximately equal in size to the diameter of a cone in the fovea. Drifts are slow motions of the eye that occur in-between micro saccades. During the drifts the fixation point moves across a dozen photoreceptors. Drifts have been reported to be conjugate, *i.e.*, they exhibit a relationship in the two eyes. Micro saccades are small, fast, jerky eye movements that correct for displacements in eye position produced by drifts and return the eye back to the fixation target. The fixation point is carried across a range of several dozen to several hundred photoreceptor widths in approximately 25 ms. Micro saccades are also found to be conjugate [84]. Micro saccades can be suppressed for certain tasks and they are controlled by the same part of the brain that controls the voluntary saccades (i.e., fast movement of the eye) [90].

[7]by which the refraction and the axial length of the eye tend to balance each other to produce emmetropia, *i.e.*, opposed to hypermetropia, myopia and astigmatism.

1.5 Eye Tracking

Eye tracking is measuring either the point of gaze or the rotation of the eye with respect to the measuring system. Eye tracking can be done either invasively by search coils[8] or electro oculography[9], or non-invasively using optics and video cameras [91]. In the last century eye tracking was mostly used as a tool to study the cognitive processes of human activities. More recently the integration of video eye tracking into human computer interactions has become an active area of research [92].

Video eye tracking can be done with visible or infrared radiation. In visible spectrum eye tracking, the ambient light reflected from the eye is captured and the contour between the iris and the sclera (white and opaque outer layer of the eye) is tracked. In infrared eye tracking, the pupil is the source of contrast in the image. Although the sclera and iris both strongly reflect infrared, only thesclera strongly reflects visible light and therefore it is used in visible spectrum imaging. Infrared eye tracking is more advantageous for several reasons. First, infrared radiation is not perceivable by the subject and does not cause discomfort. Second, the pupil contour is smaller and more sharply defined than the contour between the iris and the sclera and it is less likely to be occluded by the eyelids [93].

Infrared video eye tracking has two approaches - active and passive or, in other words, bright and dark pupil tracking. In active infrared eye tracking, the pupil is illuminated with a source on the axis of the camera and the eye where the light is reflected back by the photoreceptors and the pupil is the brightest part of the image [94, 95, 96]. In the passive approach, an off-axis source illuminates the pupil and the pupil appears to be the darkest part of the image. In this case the first surface reflection of the illumination source off the cornea is visible.

When the light is shone into the eye it is reflected not only at the front surface of the cornea but also at the back of the cornea and at the front and back of the

[8] coils embedded in the tightly fitting contact lens that adheres to the eye
[9] measuring the resting potential of the retina using a pair of electrodes

crystalline lens. These four reflections are called Purkinje images and the technique that uses the relative position of the first and fourth Purkinje images to estimate the rotation of the eye is called dual-Purkinje-image eye tracking. This method can have $<1'$ precision, span a $\pm 20^\circ$ field of view and can be as fast as 400 Hz (Crane and Steele, 1985; Muller et al., 1993). Information regarding the rotation of the eye is useful and integrating such a system in the retinal imaging system is our future goal.

Video eye tracking has a wide range of applications. In terms of a subject's integration into the system, video eye tracking can be classified into three: head-supported, head-mounted and remote eye tracking systems. The head-supported systems use a chin rest to stabilize the subject's head. Even though the subject has a restricted freedom of movement, these systems can not preclude minute head movements of the subject. In head-mounted systems, the imaging system is mounted on the subjects head by means of a helmet [93, 97, 98]. Remote eye tracking is the most challenging of the three and has applications in areas of human computer interaction, security, and others. In this case, the subject is restricted to a relatively confined area but is free to move [99, 100, 101, 102, 103, 104, 105, 106, 107]. Eye tracking also plays an important role in refractive eye surgeries.

The difference between an eye tracking and a pupil tracking system is that a pupil tracker only follows the center of the pupil in the video of pupil images whereas an eye tracker provides information on the rotation of the eye [108, 109]. Commercial eye trackers aim to track the eye movements in a wide field of at least $\pm 40^\circ$ where the pupil tracker that will be described here seeks only to follow fixational eye movements which span $\sim \pm 10^\circ$ of visual field.

1.6 Pupil tracking for adaptive optics

Adaptive optics consists of any tool that can be helpful in compensating for the changing aberrations. Based on the hypothesis that a significant part of the aber-

ration changes with respect to the wavefront sensor are due to eye movements, in this research our aim was to use pupil tracking as a part of the adaptive optics system.

In retinal imaging, a single frame acquired in a short exposure time may be without any motion blur caused by eye movements but has a high level of noise due to the scatter from different layers of the retina and detector noise. If many images are acquired in a sequence there is a good chance that there will be images exposed during a micro saccade and show nothing but blur. When those images are eliminated and the remaining images without motion blur are averaged with a registration program which aligns them using cross correlation[10], the signal coming from the cones add up and the background noise is averaged out; as a result the signal to noise ratio of the final composite image of many different frames is higher. This is possible because the cones are common but the background noise is not common in all the images, so when they are summed up, the resulting composite image will have a more homogenous, low frequency noise in the background and brighter cones. The low frequency noise then, can be eliminated by applying Fast Fourier Transform and appropriate mathematical filters [110].

Figure 1.7 shows a different approach in which there was an active retinal tracker to compensate for eye movements during image exposure [111].

In Figure 1.7 - a, the sequence of 52 images acquired without retinal tracking were averaged including the images with motion blur. Figure 1.7 - b shows that if a tracker compensates for the eye movements during exposure of the image, the averaged composite image of 67 frames without image registration or exclusion of any frames can result in a better image where cone mosaic is revealed. In addition to retinal tracking during image exposure, if image registration is applied to the same sequence of frames to compensate for the tracking errors, the result is much more better, Figure 1.7 - c. Figure 1.7 - d compares the line profiles of three cones indicated in (c) with the same cones of a single frame of the sequence of acquired

[10] a measure of the similarity of two wavefronts

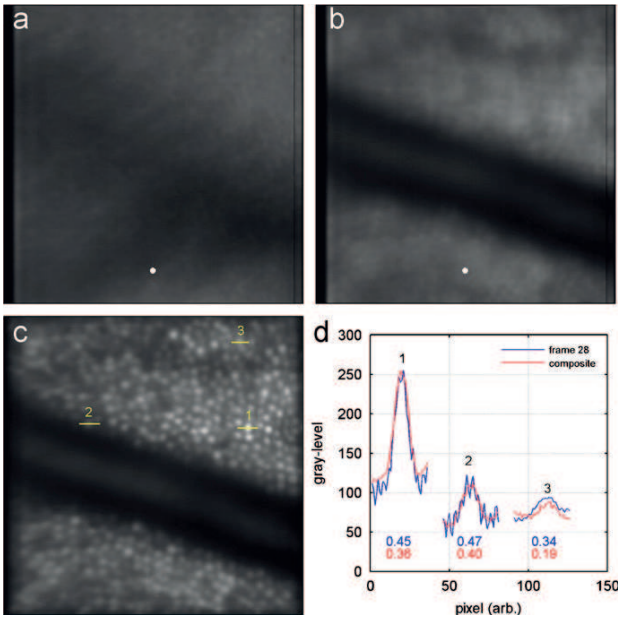

Figure 1.7: Images acquired by a scanning laser ophthalmoscope equipped with adaptive optics and retinal tracking (courtesy of Hammer *et al.* [111]). (a) Co-addition of images that were acquired without tracking (52 frames), (b) with tracking (67 frames), and (c) with both tracking and image registration (67 frames). (d) Comparison of line profiles of three cones that were indicated in the composite image (c) with a single frame which was not shown here.

67 images. Although the single frame that is compared is not shown here, in the Figure 1.7 - d it can be seen that the cones of the average of the 67 images have smoother line profiles [111]. In their recent paper Ferguson *et al.* [65] further confirmed that real time tracking could significantly improve stable overlap and efficiency of sequential adaptive optics scanning laser ophthalmoscope image capture by limiting the magnitude of eye movement excursions. Integration of adaptive optics to the retinal imaging modalities reduced the transversal pixel size making image quality more vulnerable to eye movements as pointed out by Podoleanu *et al.* [112] in their review on combinations of retinal imaging techniques. Trackers can be used to compensate for the eye movements real time as well as the movements can be predicted in healthy eyes as Aurea *et al.* [113] showed in their recent study.

There have been several studies on dynamics of the ocular aberrations to estimate the necessary rate of an adaptive optics system to compensate efficiently; however, very little attention was given to the effect of eye movements on those

changes. Aberration changes mainly were described by tear film or lens fluctuations as correlated with periodic cycles of the cardiopulmonary system[11] [52, 114, 21, 48, 42]. In general it was found that the magnitude of the fluctuations diminished with the increasing order of the aberrations in terms of Zernike polynomials [40, 115]. In their paper Hofer *et al.* [52] proposed that an adaptive optics system which worked at a closed loop rate of 2Hz would be sufficient to produce images with high resolution and faster systems would not be beneficial. This was probably due to the fact that they were concentrating on a low order aberration which dominated any other higher order aberrations, the defocus which was a result of the crystalline lens fluctuations at the heart rate. Later on Santana *et al.* [114] argued that faster adaptive optics would be beneficial.

High resolution retinal imaging systems with adaptive optics have not yet been available for clinical use because of the high cost and complexity of the systems. Efficiency of the adaptive optics depends highly on the alignment of the subject's eye with respect to the system and this becomes the weak point of device, which has to be reliable. Best results of current adaptive optics systems were acquired with subjects who can fixate their eyes well and using not only a chinrest but also a bite bar to stabilize the head movements. In comparison to the young and healthy test subjects of the research systems, in the clinic the subjects are from all ages of which the children and elderly find it hard to fixate and uncomfortable to use a bite bar. Also in some of the diseased conditions of the eye, eye movements become much more extreme and make it harder to correct for the aberrations, *e.g*, age related macular degeneration.

Effect of translations on the high order aberrations with respect to a measuring system, have been studied for different purposes. For instance Guirao *et al.* [116, 117] looked into the effect of decentrations of a contact lens when it is used to correct for not only primary but also high order aberrations. They pointed out that higher order aberrations are more sensitive to shift and they generate lower

[11] consists of the heart and the lung

order aberrations. They proposed a selective correction of higher order aberrations, meaning to compensate for the higher order aberrations that would not produce more aberrations when they are decentered. Another interesting study on decentrations was concerning myopic post-lasik refractive surgery subjects by Moreno *et al.* [118]. They highlighted the importance of eye tracking during lasik operations and showed that coma aberrations were induced post-surgery in linear relation with the error of the refractive correction *i.e.* the decentration of the formed pattern on the cornea.

In contrast to using retinal tracking to stabilize the retina during retinal image exposure as shown above, our approach is to use pupil tracking as a part of the adaptive optics system; to stabilize the pupil with respect to the deformable mirror during the correction of the eye's aberration, see Figure 1.8.

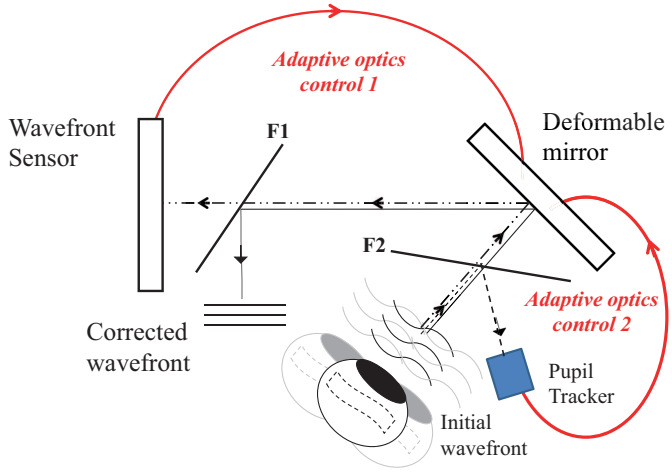

Figure 1.8: Schematics of a basic adaptive optics system with pupil tracking as adapted from Figure 1.3 with the addition of the pupil tracker, a second filter (F2) and the control algorithm based on pupil tracking that updates the deformable mirror.

Although a pupil tracker can be used in many different ways in an adaptive optics system, the aim of this research was to update the deformable mirror with the information coming from the pupil tracker and compensate for the shift of the pupil that happened during the wavefront sensing. The wavefront sensor measurement takes a certain time, but by this way the deformable mirror is aware of the pupil and the wavefront shift in between the start of the exposure of the wavefront

sensing camera and the outcome and it can update the measurement and produce a shifted correction, Figure 1.9.

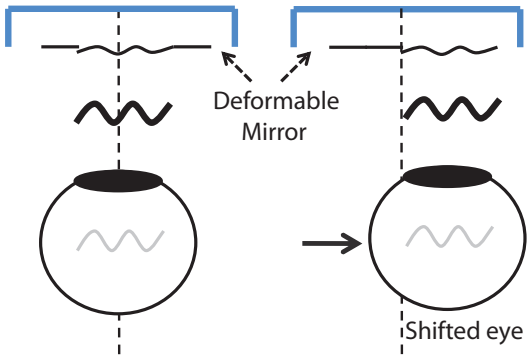

Figure 1.9: The deformable mirror corrects for the aberrations of the eye (left) and updates the previous correction when the eye is translated (right).

A commercial clinical device has to be cost effective and optical technology has always been a matter of trade off between speed and precision. The pupil tracker in a retinal imaging system with adaptive optics does not require any extra hardware; it uses the standard camera that is used for the alignment of the eye with respect to the system. Using a fast pupil tracker may help compensate for changes in the aberrations using a not-so-fast wavefront sensor which has a high precision.

Chapter 2

The Adaptive Optics Flood Illumination Retinal Camera

The adaptive optics retinal camera is a compact flood illumination system[1] that produces high resolution images of the human retina and is designed for clinical research, see Figure 2.1 [4, 119, 120, 121, 122].

Figure 2.1: The adaptive optics flood illumination retinal camera is comprised of the instrument head, patient chinrest, the power supply for the deformable mirror (small box on the table) and a PC running on Windows XP installed with the retinal imaging software. On the computer screen of the retinal camera the image provided by the pupil camera that is used for eye alignment and the image of the retina in real time can be seen.

Viard *et al.* [122] described the system in detail in their recent work: the

[1] the light is sent at once in a large field of view and reflections from all the layers of the retina are received

system is comprised of seven different optical paths: four for illumination, one for analysis and two for imaging as illustrated in Figures 2.2 and 2.4.

As described in Figure 2.2, for illumination, an 850 nm LED (R-IL) is used to provide a uniform $4° \times 4°$ flood illumination field on the retina, a 750 nm super luminescent diode (A-IL) is used to create a point source on the retina for wavefront sensing and an array of ten 850 nm LEDs to illuminate the iris uniformly are used, where an organic light emitting diode miniature monitor (FIX) served as the fixation target.

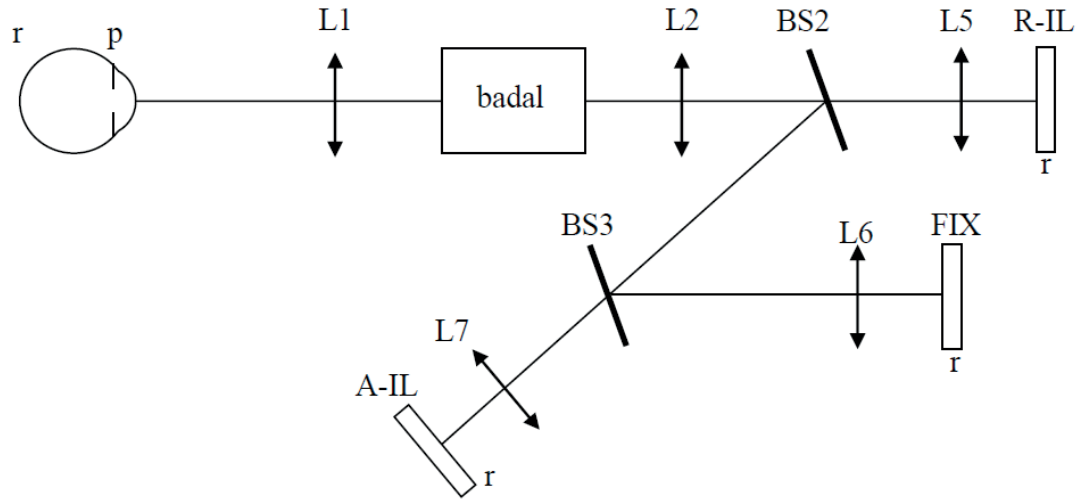

Figure 2.2: Illumination system of the retinal camera where the illumination source for the retinal imaging (R-IL), illumination source for wavefront sensing (A-IL), fixation target (FIX), Badal, lenses (L), beam splitters (BS), retina (r) and pupil (p) are shown as appropriate [122].

Total irradiance during imaging was measured as 2.4 $\frac{mW}{cm^2}$ on the cornea and 0.09 $\frac{W}{cm^2}$ on the retina certifying this system as a group I device (no potential hazard) under ISO 15004-2:2007 [123], see Appendix B.

A low noise CCD camera (R-CCD) which had 1392×1040 pixels imaging area was used where one pixel on the camera plane corresponded to 1.6 μm on the retina, see Figure 2.4. The exposure time of the camera is 9 ms and it takes 105 ms in total to acquire a retinal image. The image beam reflects off the magnetic deformable mirror (mirao 52e, Imagine Eyes, France) which is conjugated with the pupil before reaching the CCD for adaptive optics correction.

The control of the surface of the deformable mirror is accomplished by sending appropriate voltages to each actuator as calculated by the control algorithm based on wavefront sensing which assumes a linear response of the membrane. The 52 actuators are placed in an $\sim$ 17 mm diameter area where the mirror surface covers an area of 15 mm diameter. In this prototype the deformable mirror had the diameter decreased with a diaphragm further to $\sim$ 12 mm with a goal to test the effect of pupil size to the image resolution, see Figure 2.3. Reducing the area of the mirror decreases the amplitude and stroke of deformation and also the resolution because of the less number of actuators. The relationship between the applied current and the force exerted on the membrane is linear. The deformable mirror can work with bandwidths up to 200 Hz.

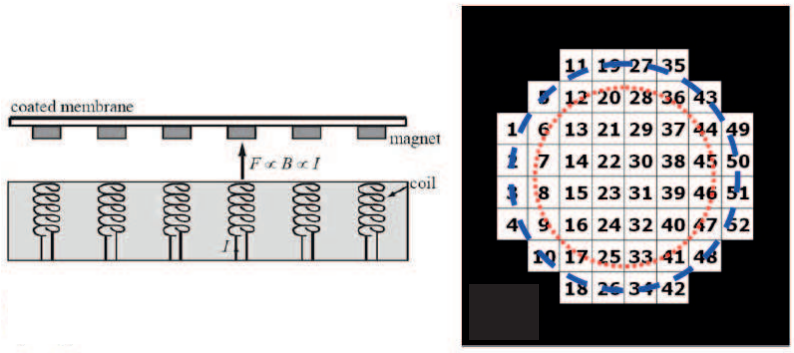

Figure 2.3: Magnets are glued under the membrane mirror which is above the coils that (when given the appropriate voltages) generate magnetic fields, pushing or pulling the magnets (left). The coils or actuators are distributed on a circular area of $\sim$ 17 mm diameter; dashed line shows the mirrored area, dotted line is the mirror area used for the experiments with the help of a diaphragm, courtesy of Fernandez *et al.* [62].

Execution of an adaptive optics loop proceeds as follows: first the measured wavefront is compared to the selected target wavefront and the difference, called residual, is multiplied by the control matrix, obtaining a set of voltage increments. These increments are added to the previous applied voltage set. Before summation, the increments are attenuated by a gain factor, preventing overshooting of the signal which might cause instability and divergence. Working with increments prevents divergence due to a wrong wavefront measurement, perhaps produced by blinking etc. The procedure is repeated continuously, in closed-loop, until the

residual is stabilized to the smallest possible value.

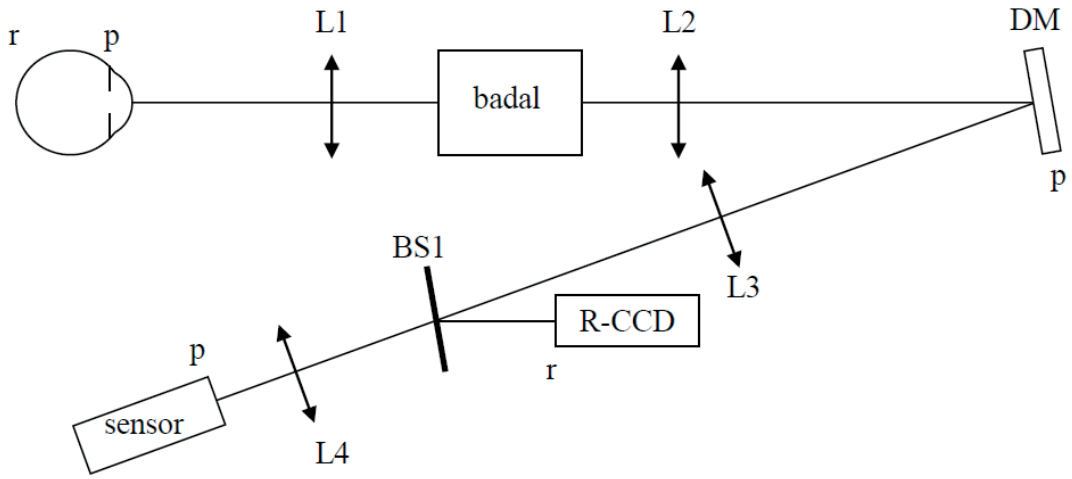

Figure 2.4: Imaging system of the retinal camera where the deformable mirror (DM), the wavefront sensor (sensor), CCD camera for retinal imaging (R-CCD), Badal, lenses (L), beam splitters (BS), retina (r) and pupil (p) are shown as appropriate [122].

The reflection of SLD at 750 nm from the retina is analysed by the wavefront sensor (HASO 32-eye, Imagine Eyes, France) as seen in Figure 2.4. It measures the slopes of the aberrated wavefront over an array of 32×40 lenslets separated by 114 microns with a 4.6 x 3.6 mm^2 area on the CCD. The reflection of the light source off the cornea is prevented by off axis illumination and its large dynamic range of $\pm$20D is largely due to the short focal length of the lenslets.

Imaging of the pupil is done using a CCD and a frame grabber. Each of the optical paths has a Badal system to compensate for the eye's refractive error from -10 D to + 8 D, leaving the deformable mirror stroke fully available to compensate for astigmatism up to 5D, strong eye optical defects and to focus the image at different layers of the retinal microstructure.

Figure 2.5 shows the system with an emphasis on adaptive optics components. In an ordinary adaptive optics system there are three interacting elements; the wavefront sensor, the deformable mirror and the control algorithm based on wavefront sensing. In this retinal camera there will be two more adaptive optics components; the pupil tracker and the adaptive optics control based on pupil tracking, see Figure 2.5.

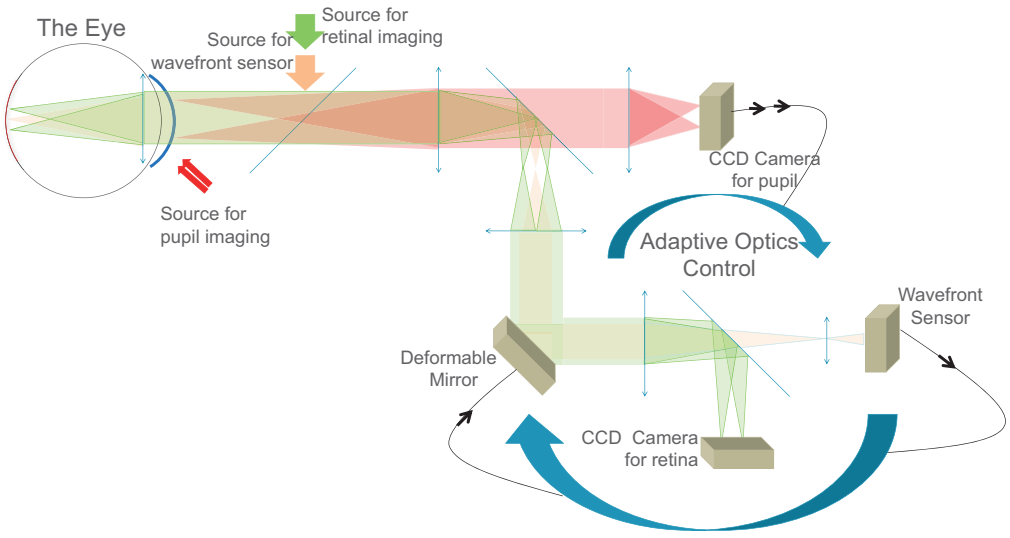

Figure 2.5: Adaptive optics system of the retinal camera, where the deformable mirror can receive wavefront information from both the wavefront sensor and the pupil tracker measurements.

There are a few topics to mention regarding the performance and the error sources of the adaptive optics of the system. Firstly, the magnetic membrane deformable mirrors were found the most suitable for ocular applications in a study made among some of the deformable mirrors that were available on the market [124]. The membrane of the mirao 52e is virtually not clamped from the edges (clamping diameter is 30 mm; two times the used area), this is an advantage because when the edges are not free to move the aberrations at the edges cannot be formed successfully. With a clamped membrane only 60% of the total area can be used; a few modes have to be sacrificed to decrease noise as ocular aberrations increase towards the edges [125, 126].

The deformable mirror's ability to represent each aberration independently depends on the flexibility of the surface and the actuator geometry. The set of Zernike polynomials that represent the aberrations can never be perfectly reproduced because the actuators of the deformable mirror and therefore the minimum set of independent functions that can be exactly reproduced by the flexible surface is finite [81]. Because of this when simulating a certain Zernike polynomial, some other Zernike polynomials also appear, which is called mode coupling or cross talk; a well known problem typically occurring with deformable continuous membranes

in the generation of surfaces. Another unwanted affect is the oscillations after the application of a step command which is due to the continuous surface and the magnets attached to the thin membrane. The oscillation time can be reduced from 15 ms to 5 ms by applying appropriate voltage curves [127, 68]. In the retinal camera prototype that is used in the course of this research a deformable mirror driver that sends step voltages was used; as a result the response time of the deformable mirror was 15 ms.

The Haso 32-eye wavefront sensor has a wide dynamic range to cover large ocular aberrations with the help of its short lenslet focal distance. A criticism regarding the adaptive optics system of the retinal camera could be regarding the resolution of the wavefront sensor. One may argue that the 32×40 lenslet wavefront sensor is sampling too much for a 52 actuator deformable mirror. A large number of lenslets means the part of the wavefront that is sampled by one lenslet resembles a tilt more, improving the estimation [55]. It must be taken into account that the total light power that is sent to the eye has to be higher with a large number of lenslets. Speckle which is a result of coherent light was another factor that affected wavefront sensor measurements. Using an SLD, a light source with wider bandwidth than a laser and relatively longer exposure times (30 ms minimum) so that the eye movements average out the speckle were solutions applied in this system.

Wavefront sensor measurements are subject to the error related to the unwanted reflections of the light sources from the lenses on the optical path and cornea. Appropriate filters were used to stop other wavelengths reaching the wavefront sensor and the SLD was used off axis. The off axis use of the SLD widens and attenuates the reflection from the cornea and the central lenslets are free from reflection which is important for the accuracy of the software. On the other hand although it is assumed that the retina is a perfect diffuser and the aberration of the incoming light source is cancelled, the off axis SLD produces some unwanted astigmatism and coma on the first path before reaching the retina. Also if the

pupil of the subject suddenly gets smaller, or moves away the SLD beam can be out of the range of the pupil boundary easily because it is already close to the edge. The optical bench ocular adaptive optics set-ups use wide, off axis spherical mirrors to prevent those deflections but this is not possible for a device which has to be compact [128, 129]. Another advantage of using spherical mirrors instead of lenses is that they do not produce chromatic aberrations. In our case achromatic doublets are used, although this is not a very big problem since we do not use polychromatic light like optical coherence tomography systems.

Once the slopes data of the angular ray deviations are acquired, they are used directly to calculate the voltages for the deformable mirror; reconstruction of the residual wavefront is not a part of the adaptive optics algorithm. Reconstruction of the measured wavefront can be effectuated outside the adaptive optics loop from the same slopes data if desired. In this thesis we will reconstruct the measured wavefronts and calculate the RMS of them to evaluate the success of the aberration correction. We will use both zonal and modal reconstruction, first of which is a discrete method based on iterations and may have fitting errors and second of which can provide RMS of individual Zernike modes but confined to a circular pupil and results in the loss of data in the case of non-circular pupils [130].

In the adaptive optics system of the retinal camera tilt terms are not corrected for by the deformable mirror. Defocus term is corrected but also can be modified either using the deformable mirror or the Badal to be used as a way to look at the different layers of the retina.

Chapter 3

The Pupil Tracking System

The pupil tracking system was developed outside the adaptive optics retinal camera in a separate set-up. The adaptive optics retinal camera made by Imagine Eyes had an eye camera to help the user align the subject's eye with respect to the system, and it was this camera that was used to acquire live eye images to track the pupil when it was adapted to the retinal camera. The pupil tracking system that is described here was made of the same type of camera for image acquisition and the same optics for pupil conjugation.

3.1 Hardware

The pupil tracking set-up was comprised of a CCD camera, an objective and a doublet for image formation, an array of ten near infrared LEDs with a mean wavelength of 950 nm to illuminate the eye and a standard ophthalmic chinrest to stabilize the subject's head, see Figure 3.1. A frame grabber is also a part of the hardware and is used to retrieve and digitize analog signals[1] from the CCD to input to the pupil tracking software for further processing. Table A.1 in Appendix A gives detailed information on the components.

The adaptive optics retinal camera had several light sources most of the time

[1]time varying signal of any type of variable. Digitization of analog data means it's conversion into binary code, which uses binary digits - bits which are either 0 or 1. The sequences of 0s and 1s that constitute information are called bytes.

on the same optical path ending up at different detectors. To prevent interference, all of the imaging components were synchronized in time and different wavelengths of light sources, appropriate filters and several beam splitters were used. The LED array stands on a LED holder which is normal to the optical axis, see Figure 3.1. Because of the 5% relative sensitivity of the CCD at 950 nm and the existence of filters and a beam splitter on the pathway, the light that reaches the CCD is as low as 1% of the light that reflects off the pupil.

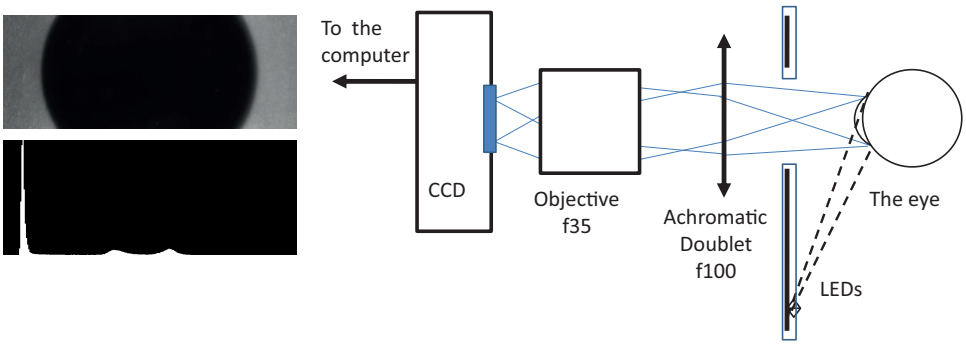

Figure 3.1: (right) The pupil tracking set-up schematics and (left) acquired image of the model eye in the case of an ideal illumination and its histogram of grey levels.

The distance of the LEDs to the optical axis and the eye was not arbitrary; the LED array was situated below far enough to avoid primary reflections from the cornea; bright spots on the dark pupil prevents the algorithm working efficiently, Figures 3.1 and 3.2. The pupil tracking algorithm ideally requires a uniformly and well illuminated eye image of which the pupil is the darkest part, see Figure 3.1. Figure 3.2 shows the image of the model eye and its histogram when it was illuminated with high power. The iris of the eye is white because the LEDs were too bright and primary reflections of are visible due to the position of the LED array.

Firstly being two arrays, one below and one above the optical axis, after realising that the light from the array above did not arrive at the eye due to the facial features only one array of LEDs below the optical axis was kept. The LEDs were carefully positioned in the LED holder socket strips using a hot melt glue gun in an inclined manner to point to slightly back of the object plane to form a

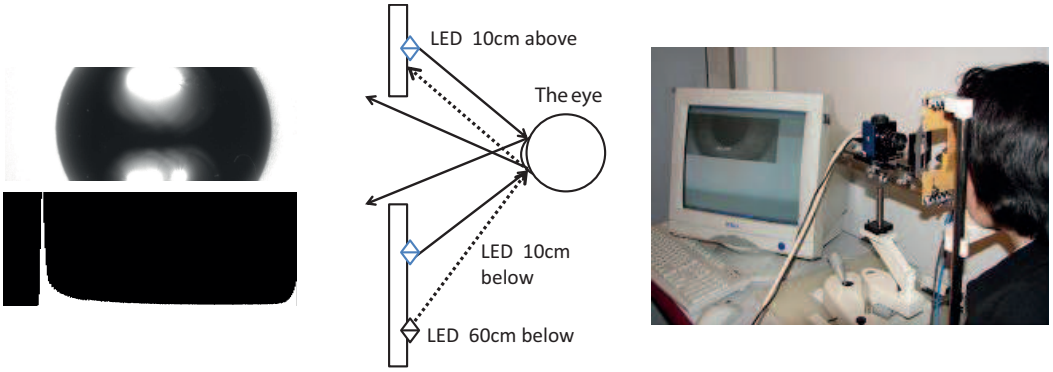

Figure 3.2: (right) The photograph of the pupil tracking set-up and (middle) schematics showing the formation of specular reflections by the LED array when they were placed 10 mm below the optical axis. (left) The image of the model eye and its histogram of grey levels where specular reflections of the two LED arrays can be seen as they were positioned 10 mm above and below the optical axis.

homogenous illumination across the desired area on the face of the eye. Finally, the set-up was tested for ocular safety and was found under the limits, for more information see Appendix B.

3.2 Software

3.2.1 The algorithm

The software was written in C++ language by S. Berthier and R. Gillet, two intern students, from an algorithm which was developed at Imagine Eyes in the previous years. My task was to develop the hardware, calibrate, test the software and use the system. The aim of the software was to track the pupil center of the acquired eye images in real time, following the steps described below.

Histogram Calculation

The first thing done by the algorithm is to produce a histogram of the eye image. Under uniform illumination, the eye images have the following characteristics: a pupil which is always the darkest part of the image and the lighter iris which has a wider distribution of grey levels. Histograms of such eye images are always like in Figure 3.3.

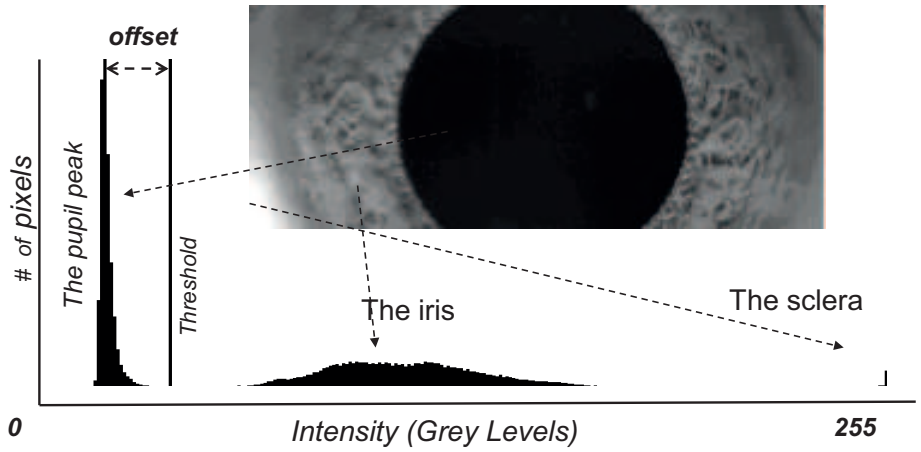

Figure 3.3: Histogram of an eye image produced by the pupil tracking algorithm.

Calculation of a threshold for binarization

Once the histogram is made, the most important information that can be derived from it is the grey level of the pupil peak which is always the highest peak in the histogram, Figure 3.3. When this is known, the next step is to estimate the threshold, the grey level of the border of the pupil, which is used to classify the pixels of the image into two; those who belong to the pupil and those that belong to the iris. For a better functioning of the algorithm the threshold is defined as, Threshold = Pupil peak + Offset.

The adaptive optics retinal camera was designed to be used by health professionals and therefore it had to be as automated as possible. Because of this, the pupil tracking algorithm had to have a pre-defined offset value which was applicable to most of the population. A survey showed that indeed under the same illumination, histograms of pupil images have very similar pupil peak and offset levels, see Figure 3.6 in Section 3.2.2.

Dynamic windows

Calculation of the threshold is followed by a search within the image for those points of transition from pupil to iris and vice versa. To save time, the area of

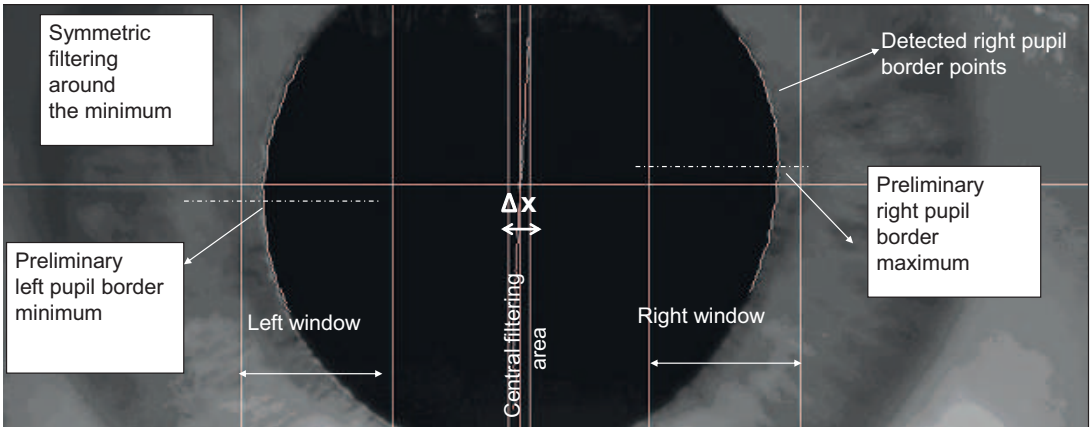

Figure 3.4: Drawing illustrates the steps of detection; dynamic windows, central and symmetric filtering, the white contour showing the detected pupil border points after central and symmetric filtering.

the image that is processed is limited into two windows, one for the left border of the pupil and one for the right, Figure 3.4. The window width was calculated for maximum number of detected border points with minimum processing time for pupils with diameters from 6 to 9 mm; the processing time of the algorithm is ~ 2 ms per frame. The algorithm can follow the pupil within a frame of ± 3 mm, both on x and y axis without being prevented by the eye lids; a covered upper or lower pupil border does not affect the measurements.

Binarization and detection of borders

Within the two windows, if the intensity value of a pixel is above the threshold, it is converted to white, and if it is below the threshold, it is converted to black demonstrating the right and left pupil borders. After detection of pupil borders, the border points that are not conjugate on both left and right borders on a horizontal line are eliminated in order to avoid image artefacts, Figure 3.4.

Central Filter

The aim of this filter is to eliminate the detected points that do not represent the pupil border. First, the centers of x - coordinates, x_{center} of each pupil border pair are calculated. Second, the median of these centers, x_{median} is found which is a

primitive estimation of the pupil center on x axis, Figure 3.4. The center of the pupil border pairs are presumed to be within a central filtering area with a width of Δx, and only the pairs with centers within this area are kept,

$$x_{center} \in \left[x_{median} - \frac{\Delta x}{2}, x_{median} + \frac{\Delta x}{2} \right]. \tag{3.1}$$

There will also be a pre-defined width of Δx, *i.e.* central filtering width which is the subject of Section 3.2.2.

Preliminary detection of pupil border minimum and maximum

Among the detected border points the ones at the far left and the far right are accepted as the x coordinates of the right and left peaks of the pupil borders for maintenance of dynamic windows, Figure 3.5. The position of the left and right window is set to be at a specific distance from these preliminary detected pupil border peaks. In this way the windows follow the pupil as it moves dynamically.

Symmetric filter

This filter equalizes the number of detected pupil border points below and above the preliminarily detected pupil border peaks because a parabolic fit that is performed on points symmetrically distributed better estimates the pupil border, Figure 3.4, 3.5.

Parabolic fit

This part of the algorithm estimates a $f_{right}(x, y)$ and $f_{left}(x, y)$ parabola equation for the right and left pupil border based on the detected pupil border points, Figure 3.5. x coordinates of the minimum or the maximum of a parabola is found by solving the derivative equation, $\frac{d(f)}{dx} = 0$. Calculation of the coordinates of the right and left pupil border peaks, (x_{right}, y_{right}) and (x_{left}, y_{left}), are followed by

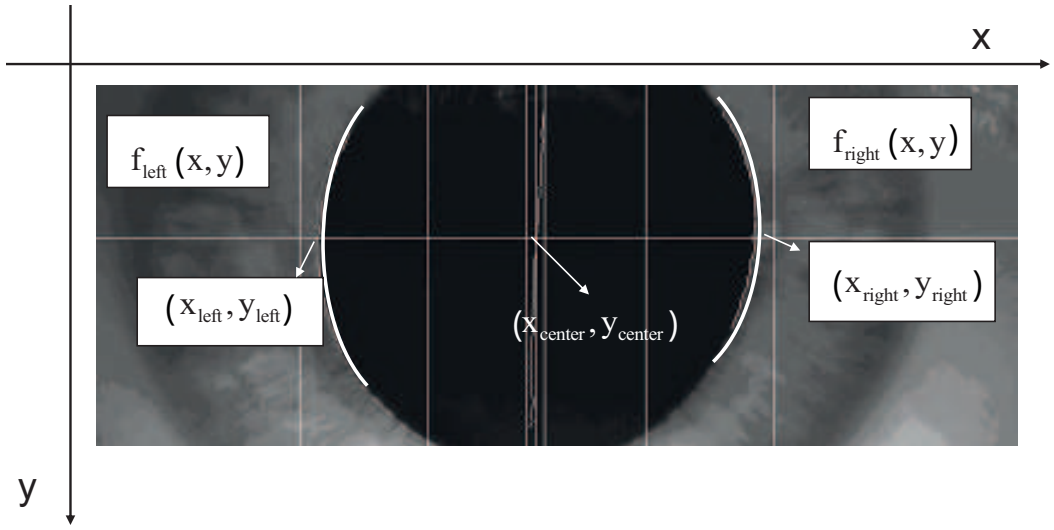

Figure 3.5: Parabolic fits $f_{right}(x, y)$ and $f_{left}(x, y)$ to the detected points.

the calculation of the center and the diameter of the pupil by,

$$(x_{center}, y_{center}, D) = \left(\frac{x_{right} + x_{left}}{2}, \frac{y_{right} + y_{left}}{2}, x_{right} - x_{left} \right). \tag{3.2}$$

3.2.2 Estimation of the offset and the central filtering width

The most efficient offset and median values may be different for each subject also it may differ instantly depending on the illumination, pupil size, or the position of the eye lids for example. It is possible to do calculations to estimate the best values in real time for each image that is acquired but this would be time consuming. Our strategy was to estimate the error related to those values and if possible pre-define the values for the general population to facilitate the use of the device in a clinical environment automatically.

The offset

The threshold value which is used to differentiate the pupil from the rest of the image is the sum of the grey level of the pupil peak and an offset value, Section 3.2.1. A survey was made among 7 female and 14 male healthy European and African origin aged 31 ± 8 in average, under a defined illumination level in which

eye images and their histograms were recorded, see Figure 3.6.

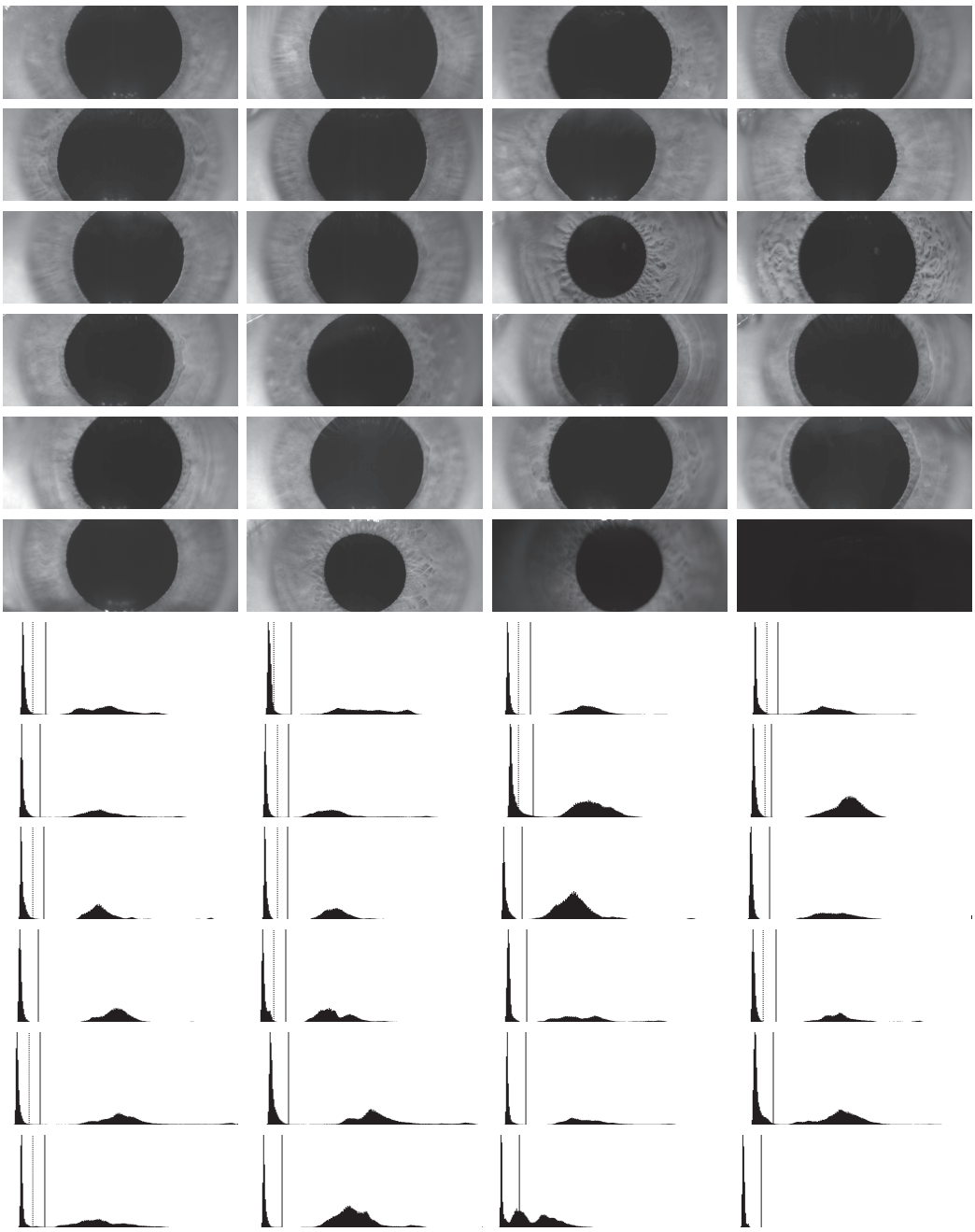

Figure 3.6: Eye images captured at the same illumination for 22 subjects. First three rows belong to colored eyes except the last two images on the right on the third row which belong to two dark colored eyes of African origin. The rest of the images belong to brown eyed Europeans. The last two images at the sixth row on the right were taken when the illumination was obscured by facial features or was not bright enough. The rest of the images are the histograms produced by the pupil tracking software from the eye images respectively. The last two histograms show how the histogram changes if the illumination was obscured or not bright enough.

Examining the histogram of an eye image, the best offset value or the best point of threshold which is the point where the pupil ends and the iris starts can be seen subjectively, Table 3.6. It is definitely using this optimum offset value that the pupil tracking algorithm can calculate the position of the pupil center most accurately. As the pupil tracking algorithm can detect pupil center on both recorded and live images, among ten of the recorded images, positions of the pupil center were calculated using different offset values. The error of the pupil center calculation was estimated by their difference from the pupil position calculated using the optimum offset value which was specific to each eye image. Figure 3.7 shows that pupil center position may vary ± 4 μm for offset values starting from 10 to 70. The standard deviation of the error distribution was lowest at the offset value of 25 which was then accepted and used as the pre-defined offset value of the algorithm.

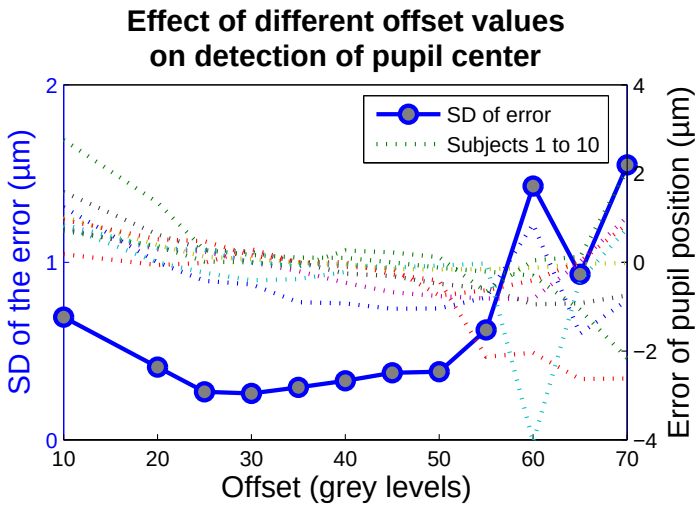

Figure 3.7: Ten images from the survey were used to estimate the offset value which fits to all eye types.

The central filtering width

In the previous section the central filtering was described. It eliminates the detected pupil border points which do not actually belong to the pupil borders. To estimate a pre-defined central filtering width (in pixels) for the algorithm again

one of the recorded eye images was used. The pupil center position was calculated using the software for central filtering widths starting from 3 to 18 pixels and for offset values from 10 to 70 grey levels. Figure 3.8 shows the calculated pupil center position as the radial distance from the bottom left corner of the eye image. The central filtering width had no significant effect on pupil position calculation where a central filtering width lower than eight pixels is slightly erroneous. A central filtering width of 10 pixels was accepted as the predefined value.

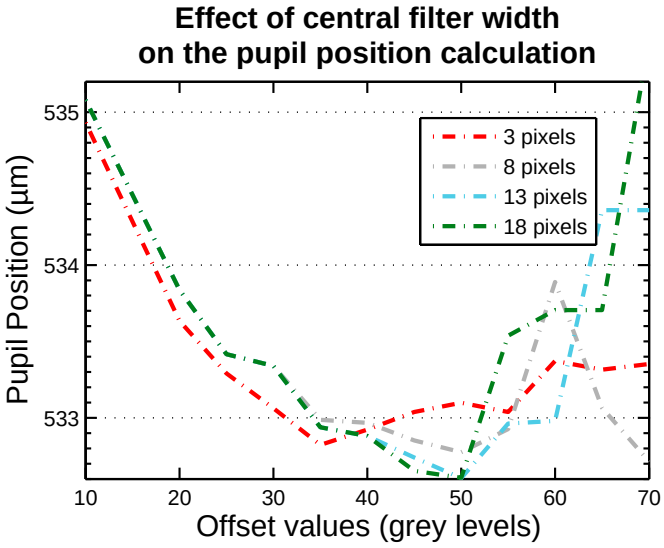

Figure 3.8: Central filtering with less than eight pixels width gave slightly different results while the central filtering width bigger than and equal to eight pixels had no significant difference.

3.3 Performance

3.3.1 Accuracy and Precision

The accuracy of a measuring system is defined as its ability to provide a value close to the true value of the measured. Accuracies of commercial eye tracking systems are expressed as the mean measurement error in degrees; the smaller the error the higher the accuracy. As the pupil tracker does not measure rotation of the eye in degrees but measures the position of the pupil center (with respect to the bottom left corner of the acquired images) in microns, the accuracy of

the system is expressed in terms of the mean measurement error from a known position in microns. Precision or repeatability of the pupil tracker will be expressed as the standard deviation of the measurements from the average value of the measurement.

Motion controller stages and a model eye[2] that produces an image histogram that closely resembles the image histogram of a real eye were used for the tests. The model eye was attached to a stage which was itself attached to a second stage forming x and y axes on a plane normal to the optical axis of the pupil tracking system.

The 2×5 mm^2 active area of the CCD corresponds to 6×14 mm^2 on the object plane due to a magnification factor of 0.34. If an eye with a 7 mm pupil moves away from the center more than ± 3 mm on the x and y axes it will be out of the range of pupil tracker's capability of taking measurements because the pupil tracking algorithm requires left and right pupil borders to be visible in the eye image. To estimate the mean error in the pupil tracking measurements we measured the pupil position of the model eye every ~ 12 ms during ~ 13 s at 25 different positions within two different central square areas of 1 mm^2 and 2 mm^2. The mean and the standard deviation of these data, $\left(\bar{x}, \bar{y}, \bar{D}\right) \pm (\Delta x, \Delta y, \Delta D)$ at each point were calculated. Table 3.1 shows the mean error and standard deviation in detection of the radial pupil position, *i.e.*, $\sqrt{x^2 + y^2}$, and the pupil diameter for the central squares of 1 mm^2 and 2 mm^2.

		Mean Error (μm)	Standard Deviation (μm)
Pupil position	($\pm$1 mm range)	6	2
	($\pm$2 mm range)	11	8
Pupil diameter	($\pm$1 mm range)	18	1
	($\pm$2 mm range)	28	1

Table 3.1: Mean errors and maximum standard deviation of radial pupil position values of 25 sets of data points within central squares of 1 mm^2 and 2 mm^2

On the x axis the pupil tracker is more accurate and precise and the detection

[2]see Appendix C, Figures C.1 and C.2

continues until one of the pupil borders is out of the image frame. Although not shown here separately, most of the error in the measurements and the lack of precision was due to the detection of the y axis because it required a parabolic fit to the data. x axis coordinates had the standard deviation of 1 μm in general, so did the pupil diameter measurements. Pupil diameter measurements had <1 μm error in the central 500 μm region but as the eye goes away the error increases.

The algorithm was more accurate within the central $\pm$1 mm region mainly because when the pupil moves upwards and downwards the detected number of pixels on the pupil borders decrease significantly causing error. In average the error related to the measurement was as low as 6 ± 2 μm but we have to keep in mind that the resolution of the pupil tracker is one pixel, i.e. $4.65 \times \frac{100}{35} = 13.2$ μm for a single measurement on the object plane, 4.65 μm being the width of one pixel on the CCD and $\frac{35}{100}$ being the magnification factor of the system.

Effect of Defocus

Although defocus is a temporary phenomenon which is quickly noticed and corrected by the operator or by the subject, it is worth estimating the error related to it. The histogram is the most crucial part of the algorithm: the quality of pupil center detection highly depends on the sharpness of separation between pupil and the iris. If the model eye is defocused along the optical axis with respect to the pupil tracker, the histogram of grey levels of the image has a thicker baseline when compared to the focused image. To estimate the error in detection, the pupil center position was measured every $\sim$ 12 ms during $\sim$ 13 s while the model eye was at 20 different positions along the optical axis within a range of $\pm$5 mm axially. The error related to the defocus of the pupil image up to $\pm$5 mm was less than 15 ± 4 μm.

Precision of real eye measurements

Even though the model eye produced a good approximation of a real eye image, in contrast, the human eye is restless by nature. Fixational eye movements at speeds of up to 100 $\frac{deg}{s}$, a pupil which dilates and contracts continuously to adapt the illumination and the minute inevitable movements of the subject's head, all make it harder to measure pupil position. The error or precision of the *in vivo* measurements of the pupil center cannot be known directly as there are no means of knowing the actual value of the pupil position with respect to the eye camera.

However, mydriatic eye drops which dilate pupil and paralyze accommodation temporarily can be used to estimate not the accuracy but the ***precision*** of the measurement indirectly. In such a case pupil diameter D becomes relatively stable and standard deviation of the pupil diameter measurements, ΔD is related to the standard deviation of the measurement of the x coordinates of the pupil center Δx_{center} (Eq. 3.2) by this way:

$$x_{center} = \frac{x_{right} + x_{left}}{2}, \tag{3.3}$$

$$\bar{x}_{center} \pm \Delta x_{center} = \frac{\bar{x}_{right} + \bar{x}_{left}}{2} \pm \frac{\sqrt{\Delta x_{right}^2 + \Delta x_{left}^2}}{2}, \tag{3.4}$$

$$D = x_{right} - x_{left}, \tag{3.5}$$

$$\bar{D} \pm \Delta D = \bar{x}_{right} - \bar{x}_{left} \pm \sqrt{\Delta x_{right}^2 + \Delta x_{left}^2}, \tag{3.6}$$

$$\Delta x_{center} = \frac{\Delta D}{2}, \tag{3.7}$$

x_{right} and x_{left} being the x coordinates of the right and left pupil borders.

Tropicamide (1%)[3] drops were applied in the left eyes of two volunteers. The pupil center position *in vivo* was measured every $\sim$ 12 ms during $\sim$ 13 s three times just after application and then in 15 minutes intervals while the subjects fixated their eyes to a target. Figures 3.9 and 3.10 show that the effect of droplets was evident after 15 minutes as the pupils were dilated by $\sim$ 2 mm and the standard

[3]Tropicamide is a neurotransmitter blocking agent that produces short acting dilation of the pupil and accommodation paralysis.

deviation of the pupil diameter measurements decreased abruptly and stabilized.

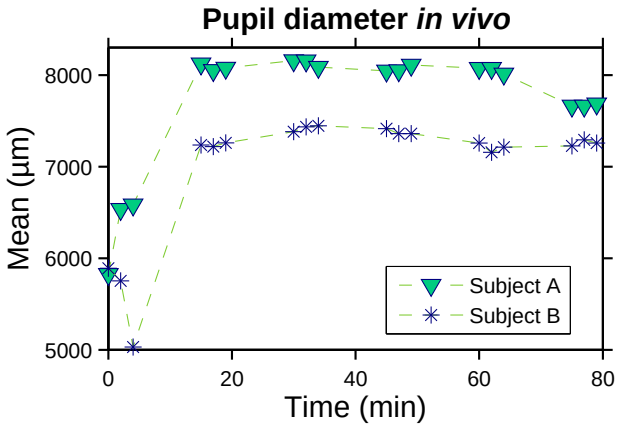

Figure 3.9: Mean of the pupil diameter measurements of two subjects taken at regular intervals after Tropicamide (1%) droplets were applied.

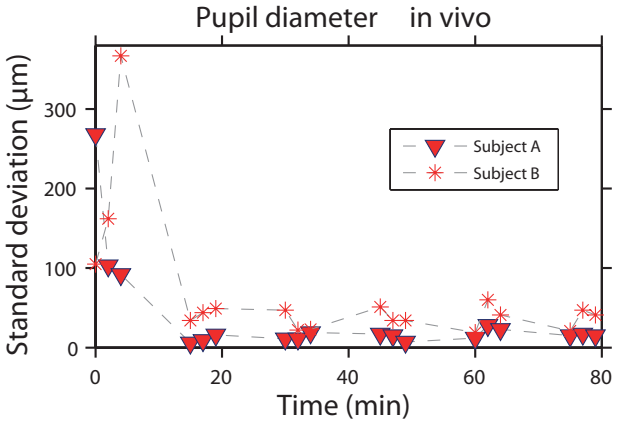

Figure 3.10: The standard deviation of the pupil diameter measurements of two subjects taken at regular intervals after Tropicamide (1%) droplets were applied.

Table 3.2 summarizes the mean and the standard deviations of 30×13 s series of measurements in total for two subjects which were taken after the pupil diameters were stable. The precision of pupil diameter measurement was the mean of standard deviations for the two subjects; $\Delta D = \frac{\sqrt{14^2+40^2}}{2} \sim 21$ μm, which leads to the precision of pupil center measurement $\Delta x_{center} = \frac{21}{2} \sim 11$ μm, assuming that the magnitude of the pupil diameter was frozen and the standard deviations were solely due to the pupil tracking system.

	Pupil Diameter Before Tropicamide	Pupil Diameter After Tropicamide
Subject A	6313 ± 153 (μm)	8002 ± 14 (μm)
Subject B	5900 ± 153 (μm)	7300 ± 40 (μm)

Table 3.2: Mean pupil diameter and standard deviations of two subjects before and after Tropicamide (1%) application.

3.3.2 The time response

Rapid eye movements deteriorate retinal images in two ways. First, the aberrations of the eye cannot be compensated for, mainly due to slow wavefront sensing in the adaptive optics system and second, during the exposure, the image exposed is spanning a vast area across the retina depending on the speed of the eye movement resulting in a blurred image. The retinal imaging camera has a 9 ms image exposure time which results in at least five blurred images out of 40 recorded in an imaging session. Those blurred images are ignored and the remaining high contrast images are chosen for digital image processing. Having this relatively slow imaging camera, there seems no advantage of being able to track rapid eye movements.

However it is useful to know the pupil tracking measurement error related to rapid eye movements as a function of speed, to evaluate the correction of eye's aberrations using adaptive optics and pupil tracking. For this purpose we needed a platform in which the model eye could move rapidly in a controllable way. The model eye was attached to a motor with the help of a mechanical piece[4] which can be attached to a motor arm, using which it was possible to place the model eye at various distances from the rotation axis of the motor, see Figure 3.11.

The motor was an electric motor with linear voltage-to-speed relationship whose true frequency of rotation could be estimated by two methods, either using the motor driver and an oscilloscope or by Fast Fourier Transform (FFT) of the recorded pupil tracking data, both of which gave results that were in good correlation, see Figure 3.12.

It was not possible to measure the radius of rotation - distance of the attached

[4]see Appendix A, Figure A.1

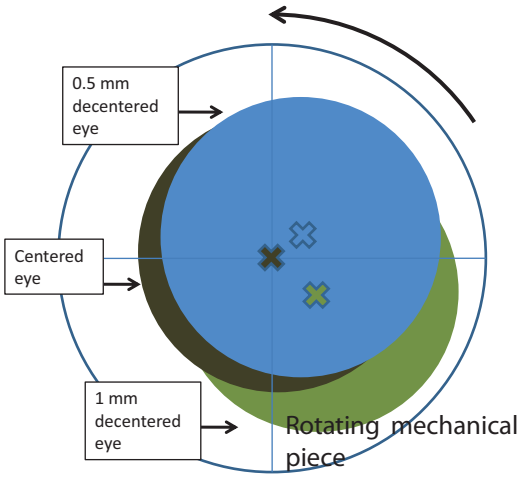

Figure 3.11: Attached to the mechanical piece the model eye can rotate with different radius of rotations around the axis of the motor arm.

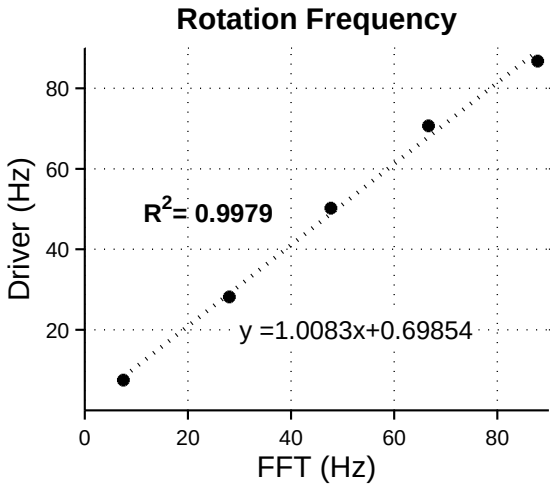

Figure 3.12: Correlation of the rotation frequencies measured from the motor driver and derived from the FFT of the pupil tracking data.

model eye to the motor axis precisely when the motor was static. Although the attachment points for different radius of rotations of the mechanical piece were known theoretically, the attachment of the model eye was not robust enough to be accurate at the micron level. The only way to know the radius of rotation was by using the pupil tracking measurement data recorded during rotation. Radius of rotation was equal to $\frac{(r_{max}-r_{min})}{2}$ where r_{max} and r_{min} were the maximum and minimum radial magnitude of the pupil center measured with respect to the bottom left corner of the eye image in microns. At different frequency and radius of rotations, the position of the pupil were recorded every $\sim$ 12 ms during $\sim$ 13 s

with a camera exposure time of 10 ms. Table 3.3 displays the estimated radius of rotations.

	8 Hz	28 Hz	48 Hz	67 Hz	88 Hz
Model eye at ∼150 μm	156 μm	140 μm	105 μm	66 μm	22 μm
Model eye at ∼200 μm	224 μm	203 μm	156 μm	108 μm	37 μm
Model eye at ∼300 μm	298 μm	265 μm	205 μm	127 μm	36 μm

Table 3.3: The radius of rotations of the model eye were deduced from pupil tracking measurements by $\frac{(r_{max}-r_{min})}{2}$, where r_{max} and r_{min} are the maximum and minimum magnitude of radial position of the pupil center with respect to the bottom left corner of the eye image.

Figure 3.13 shows the errors in estimation of radius of rotations based on pupil tracking data. The lowest frequency of rotation that could be achieved by the

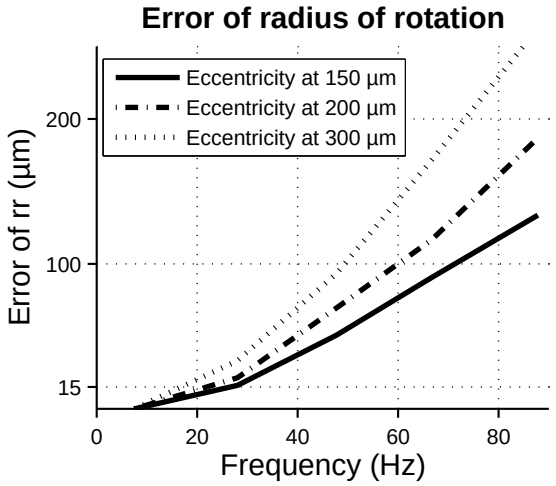

Figure 3.13: Error in radius of rotation (rr) estimations for frequencies of 8-89 Hz and radius of rotations of $\sim$ 150, 200 and 300 μm.

motor was $\sim$ 8 Hz and the actual radius of rotation of the model eye was accepted as the one calculated at this frequency. For the same frequency of rotation the error of measurement for a model eye rotating with a bigger radius of rotation was larger. In the same way the model eyes at the same radius of rotations with higher frequencies of rotation introduced more error and deteriorated the perceived radius of rotation by the pupil tracker, see Figure 3.14.

The error of measurement was related to the radius and frequency of rotation quadratically, see Figure 3.13. It is reasonable to assume that the error of measurement was proportional to the square of the speed $v = 2\pi rf$ of the model eye,

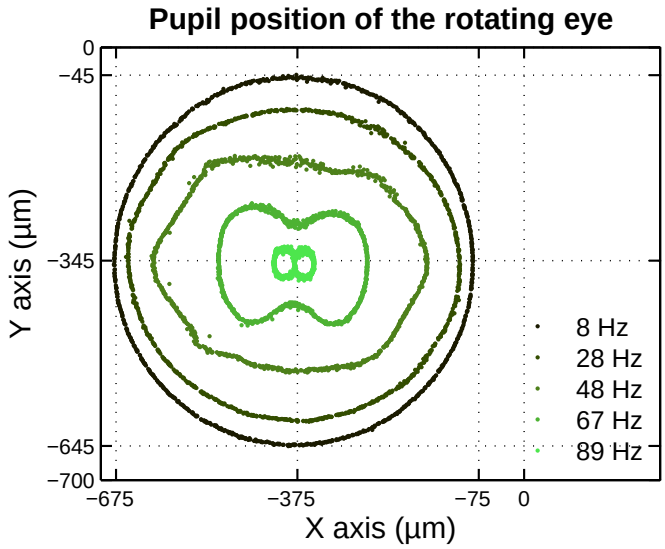

Figure 3.14: The pupil tracking data on x-y plane for increasing frequency of rotations while the model eye was rotating at ~ 300 μm and the camera exposure time was 10 ms.

r and f being the radius and frequency of rotation respectively. Converting all the data taken at various radius and frequency values into the speed of the model eye, $Error \propto v$ was plotted and a second degree polynomial curve was fit with a correlation coefficient of 0.99, see Figure 3.15.

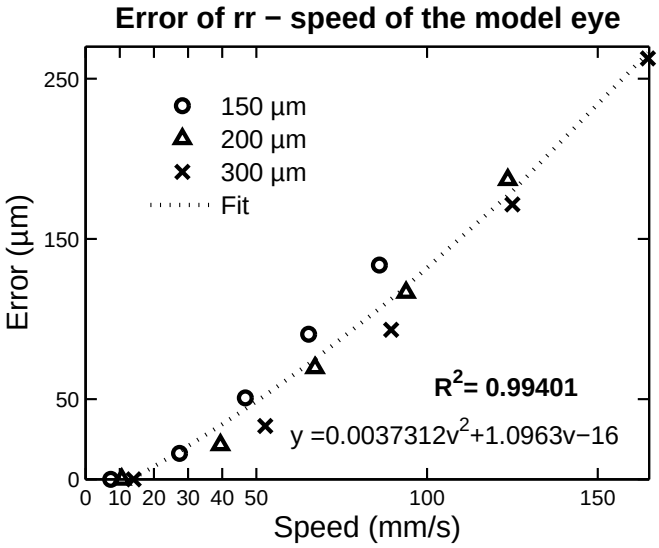

Figure 3.15: Error of radius of rotation (rr) estimation in relation to the tangential speed of the model eye.

When the eye moved by less than 25 $\frac{mm}{s}$ the error of the measurement was less than 15 μm which is close to the error of static measurements, see Figure 3.15.

Now we will convert this units into the $\frac{deg}{s}$ based on the Figure 3.16.

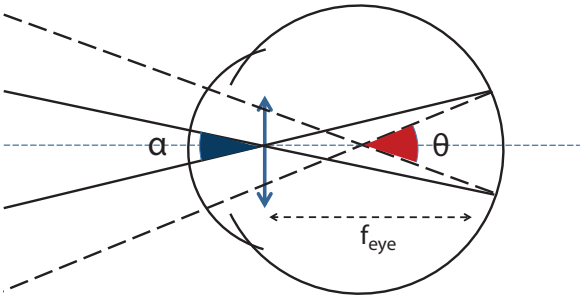

Figure 3.16: θ is the angle of rotation of the eye which takes place around its center, α is the field of view of the rotation, f_{eye} is the focal distance of the refraction of the eye.

The rotation of the eye takes place around its center, because of this a pupil displacement of Δx measured by the pupil tracker corresponds to the same displacement on the retina. Δx can be expressed in terms of angle of view α by taking into account the f_{eye}, the focal length of the eye,

$$tan(\alpha) = \frac{\Delta x}{f_{eye}} \tag{3.8}$$

$$\alpha = tan^{-1}(\frac{\Delta x}{f_{eye}}) \tag{3.9}$$

This follows that a pupil movement at 25 $\frac{mm}{s}$ corresponds to 55 $\frac{deg}{s}$ on the retina, when f_{eye} was taken as 17 mm. The micro saccades were reported to have 10 $\frac{deg}{s}$ mean speed and maximum speeds as high as 100 $\frac{deg}{s}$ whereas, the maximum speed accepted for a drift is 0.5 $\frac{deg}{s}$ on the retina[84]. In conclusion it can be deduced that the pupil tracker can follow drifts and micro saccades up to 50 $\frac{deg}{s}$ speed with its default accuracy and precision as long as they are within central $\pm 5^{\circ}$ range.

As the camera exposure time gets longer there is more blur in the image due to movement, the pupil border becomes less sharp and error is inevitable. The image exposure time also effects the input light level; a short exposure time requires more power on the surface of the eye. Ocular safety concerns and the configuration of the

retinal camera do not allow us to use the eye camera at an exposure time less than 10 ms *in vivo* because this would require significantly higher light input. On the other hand it is possible to perform experiments with an image exposure time of 2 ms using the model eye. Figure 3.17 shows that the amount of pupil tracking error in measuring a moving eye is directly related to the amount of time required for image exposure of the camera and that the pupil tracker could work with almost no error up to 60 Hz with a radius of rotation of 150 μm which corresponds to a model eye which moves by almost 60 $\frac{mm}{s} = tan^{-1}(\frac{60}{17}) = 75\ \frac{deg}{s}$.

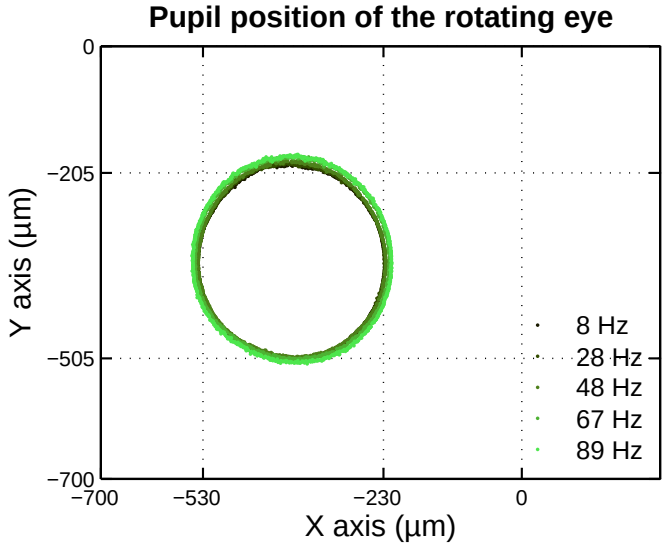

Figure 3.17: The pupil tracking data on x-y plane for increasing frequency of rotations while the model eye was rotating at $\sim$ 150 μm and the camera acquisition time was 2 ms.

Assuming the pupil tracker was a linear system, its gain for rotational movement would be calculated by, $Gain = 10log(Power_{out}/Power_{in})$ where a 3dB decrease would correspond to the cut-off frequency of rotation at which the output power of the system was half of the input power, see Figure 3.18.

The input power of the system was directly related to the square of the radius of rotation as the rotational kinetic energy of the model eye was $E_K = 1/2I\omega^2$ where $I = \sum_{i=1}^{N} m_i r_i^2$ was the moment of inertia, m_i, r_i and ω were the point mass, radial distance of the point mass to the rotation axis and the angular velocity of the model eye respectively. Output power of the system was square of the amplitude of the FFT of the measurements which had the two peaks with equal amplitude

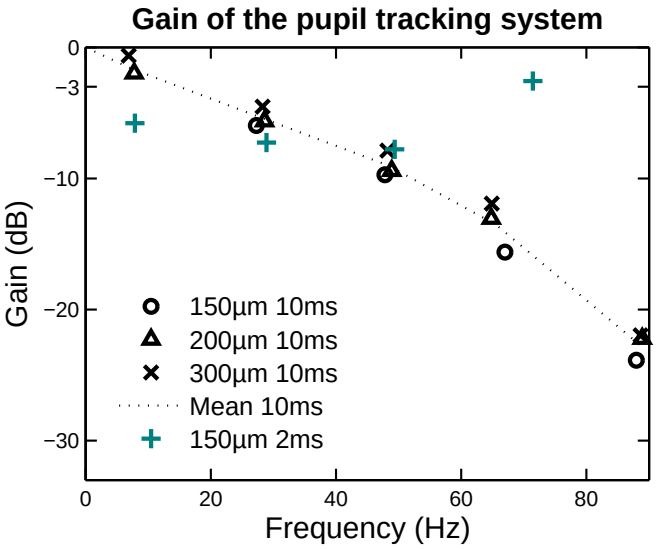

Figure 3.18: $Gain = 10log(Power_{out}/Power_{in})$ of the pupil tracker with the acquisition time of 10 ms, the model eye at radius of rotation of 150, 200 and 300 μm and with acquisition time of 2 ms, the model eye at radius of rotation of 150 μm.

on the frequency axis one being the mirror image. The amplitude of the FFT was distributed to those two peaks so that total amplitude was their sum.

Figure 3.18 shows that there was a 3dB decrease of gain even before a frequency of rotation of 20 Hz which did not comply with the results found early in this section. With the same frequency of rotation a model eye which had a radius of rotation of 300 μm was faster than a model eye which was at 150 μm therefore the pupil tracker was expected to have more error and a steeper curve for the model eye which was farther but it was the opposite. The gain curve for the 2 ms image acquisition time started below 3dB and had a tendency upwards for higher frequencies which can be seen in the Figure 3.14 as the radius of rotation increases by frequency of rotation. As a result it can be derived that our assumption was wrong and pupil tracker was a not a linear system.

3.4 Discussion

In conclusion we developed a pupil tracking system which is accurate and precise in tracking fixational eye movements that are within $\pm 5^\circ$ field of view. The blur

related to the long 10 ms exposure time of the camera was the major factor that defined the traceability of a moving pupil by this system.

The pupil tracker can follow majority of the eye movements and *in vivo* measurements had similar precision with the measurements done with the model eye.

Chapter 4

Adaptive Optics Control Algorithm Based on Pupil Tracking

In this chapter first, a brief introduction to the classical adaptive optics control algorithm based on wavefront sensing, second, a description of the adaptive optics control algorithm based on pupil tracking, then the results of simulations, preliminary experiments done and the problems encountered will be given.

4.1 Adaptive optics algorithm based on wavefront sensing

The adaptive optics system of the adaptive optics retinal camera consists of an electromagnetic deformable mirror with 52 actuators and a Shack-Hartmann wavefront sensor with 32×40 lenslets, for specifications of the components see Appendix A, Table A.2. The lenslet matrix has a rectangular shape only because it is easier to find a rectangular CCD array than a square one, the pupil of wavefront sensing is not elliptical; it is circular.

Typical outcomes of a Shack-Hartmann wavefront sensor measurement with

32×40 lenslets are two separate data matrices containing $s_{x_{ij}}$ and $s_{y_{ij}}$, the projections of Δs_{ij} on x and y axes where $i = (1, 2, \ldots, 32)$ and $j = (1, 2, \ldots, 40)$ are the indices of the lenslet array, see Figure 4.1.

$$s_x = [\,]_{32\times 40}\,, \;\; s_y = [\,]_{32\times 40} \tag{4.1}$$

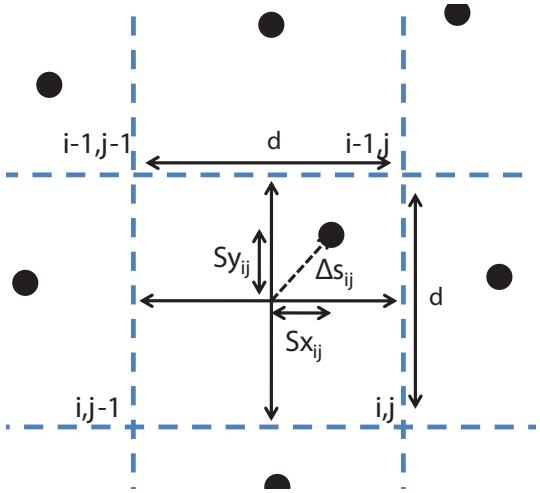

Figure 4.1: Distribution of the Shack-Hartmann spots on the CCD as they are generated by the two dimensional lenslet array where d is the diameter of the lenslets, i and j denote the lenslet indices.

The slope vector $\mathbf{s}$ of a wavefront measurement is built from s_x and s_y by,

$$\mathbf{s} = [s_{x_1}, s_{x_2}, \ldots, s_{x_K}, s_{y_1}, s_{y_2}, \ldots, s_{y_K}]^T_{1\times 2K}\,, \tag{4.2}$$

where K is the number of valid lenslets, $K \leq 32 \times 40 = 1280$. The interaction matrix $\mathbf{IM}$ of a wavefront sensor and deformable mirror pair is the assembly of all slopes vectors that are measured and built after pushing and pulling of all the actuators of the deformable mirror one by one,

$$\mathbf{IM} \;\; = \;\; [\mathbf{s_1}, \ldots, \mathbf{s_m}, \ldots, \mathbf{s_M}]_{2K\times M}$$

$$= \begin{bmatrix} s_{x_{11}} & \cdots & s_{x_{1m}} & \cdots & s_{x_{1M}} \\ \vdots & \ddots & \vdots & \ddots & \vdots \\ s_{x_{k1}} & \cdots & s_{x_{km}} & \cdots & s_{x_{kM}} \\ \vdots & \ddots & \vdots & \ddots & \vdots \\ s_{x_{K1}} & \cdots & s_{x_{Km}} & \cdots & s_{x_{KM}} \\ s_{y_{11}} & \cdots & s_{y_{1m}} & \cdots & s_{y_{1M}} \\ \vdots & \ddots & \vdots & \ddots & \vdots \\ s_{y_{k1}} & \cdots & s_{y_{km}} & \cdots & s_{y_{kM}} \\ \vdots & \ddots & \vdots & \ddots & \vdots \\ s_{y_{K1}} & \cdots & s_{y_{Km}} & \cdots & s_{y_{KM}} \end{bmatrix}_{2K \times M} , \tag{4.3}$$

where $M = 52$ is the number of actuators. The command vector $\mathbf{v}$ holds the voltages to be applied to the actuators of the deformable mirror,

$$\mathbf{v} = \left[v_1, v_2, \ldots, v_M\right]_{1 \times M} . \tag{4.4}$$

If the interaction matrix of the wavefront sensor and deformable mirror configuration is known, the slope vector $\mathbf{s}$ of the wavefront produced by the deformable mirror in response to the applied voltages $\mathbf{v}$ can be estimated by,

$$\mathbf{s} = \mathbf{IM} \times \mathbf{v}. \tag{4.5}$$

During adaptive optics correction, the control algorithm based on wavefront sensing calculates the $\mathbf{v}$ to be applied to the deformable mirror from the slope vector of the measured wavefront $\mathbf{s}$ each time,

$$\mathbf{v} = \mathbf{IM}^{\dagger} \times \mathbf{s}, \tag{4.6}$$

using $\mathbf{IM}^{\dagger}$ which is the pseudo inverse of the interaction matrix calculated by singular value decomposition[1] because $\mathbf{IM}$ is not an invertible square matrix.

[1] an $m \times n$ matrix M is factorized of the form $M = U\Sigma V^*$ after which $M^{\dagger} = V\Sigma^{\dagger}U^*$.

4.2 Adaptive optics algorithm based on pupil tracking

The adaptive optics control algorithm based on pupil tracking works by approximating a unit shift on x and y axes for both s_x and s_y data of a reference wavefront measurement $\mathbf{WF_{Ref}}$. For s_x, the unit shift on the x axis $\Delta_x s_x$ and the unit shift on the y axis $\Delta_y s_x$ are produced by shifting s_x one row (of lenslets) to the left and subtracting this from the initial s_x and by shifting s_x one column (of lenslets) downwards and subtracting this from the initial s_x respectively,

$$\begin{aligned} \Delta_x s_{x_{ij}} &= s_{x_{i,j+1}} - s_{x_{ij}} \qquad \text{for} \quad i = 1, 2, \ldots, 32 \\ \Delta_y s_{x_{ij}} &= s_{x_{i+1,j}} - s_{x_{ij}} \qquad\qquad j = 1, 2, \ldots, 40. \end{aligned} \tag{4.7}$$

The procedure is repeated for s_y to produce $\Delta_x s_y$ and $\Delta_y s_y$,

$$\begin{aligned} \Delta_x s_{y_{ij}} &= s_{y_{i,j+1}} - s_{y_{ij}} \qquad \text{for} \quad i = 1, 2, \ldots, 32 \\ \Delta_y s_{y_{ij}} &= s_{y_{i+1,j}} - s_{y_{ij}} \qquad\qquad j = 1, 2, \ldots, 40. \end{aligned} \tag{4.8}$$

Having acquired $\Delta_x s_x$, $\Delta_y s_x$, $\Delta_x s_y$, $\Delta_y s_y$, we can now construct the slope vector for one unit shift on x axis $\Delta_x \mathbf{s}$, and the slope vector for one unit shift on y axis $\Delta_y \mathbf{s}$,

$$\begin{aligned} \Delta_x \mathbf{s} &= \left[\Delta_x s_{x_1}, \ldots, \Delta_x s_{x_{k'}}, \ldots, \Delta_x s_{x_{K'}}, \Delta_x s_{y_1}, \ldots, \Delta_x s_{y_{k'}}, \ldots, \Delta_x s_{y_{K'}}\right]^T_{1 \times 2K_{IM}} \\ \Delta_y \mathbf{s} &= \left[\Delta_y s_{x_1}, \ldots, \Delta_y s_{x_{k'}}, \ldots, \Delta_y s_{x_{K'}}, \Delta_y s_{y_1}, \ldots, \Delta_y s_{y_{k'}}, \ldots, \Delta_y s_{y_{K'}}\right]^T_{1 \times 2K_{IM}}, \end{aligned} \tag{4.9}$$

where $K' \leq K$ and K_{IM} depends on the effective pupil of the IM.

To demonstrate the method, a pure coma (y axis) aberration was formed using the deformable mirror and the data matrices s_x and s_y of the aberration measured by a 32×40 lenslet wavefront sensor were used, see Figure 4.2.

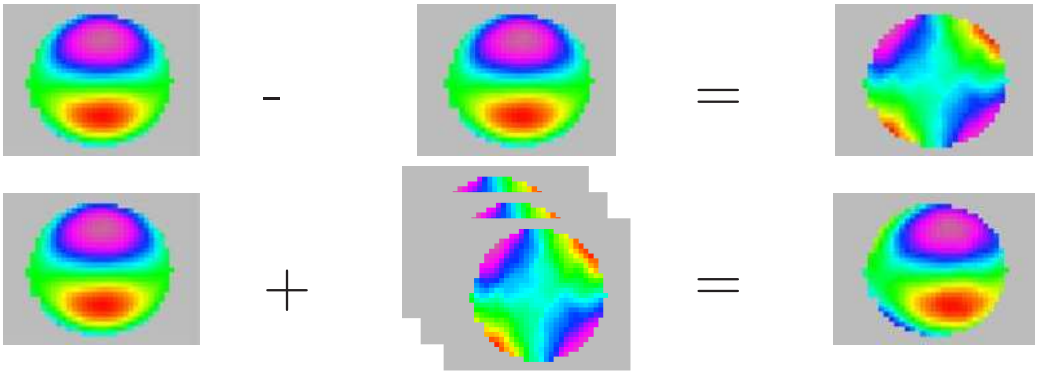

Figure 4.2: The coma (y axis) aberration data on 32×40 lenslet array was shifted one lenslet to the right and was subtracted from the original yielding one unit shift on x axis (top). Three lenslet shifted coma was produced by adding three unit shifts to the original data, as wavefronts were built by zonal reconstruction from the slopes data (bottom).

First, both s_x and s_y matrices were shifted to the right one column then these matrices were subtracted from the originals, the results were the slopes data representing one columns (of lenslets) shift on x axis, $\Delta_x s_x$ and $\Delta_x s_y$. Next $\Delta_x s_x$ and $\Delta_x s_y$ were multiplied by three and added to the original untouched slopes data matrices, s_x and s_y respectively. Three lenslets shift which corresponds to almost 1 mm of shift of the pupil on the object plane was only chosen to make the displacement visible to the reader. It has to be noted that our aim is compensating for the displacements of the pupil smaller than the diameter of one lenslet. The results were the slopes data for the three lenslet shifted coma aberration. The wavefronts at each step were reconstructed by zonal reconstruction method using the slopes data of both axes, Figure 4.2.

If $f(x, y)$ was the polynomial representing a wavefront aberration, the slope data of the aberration s_x and s_y would be approximately its partial derivatives on x and y axis, $\frac{\partial f}{\partial x}$ and $\frac{\partial f}{\partial y}$ respectively. Calculating the one column (of lenslets) shift on x axis, $\Delta_x s_x$ and $\Delta_x s_y$ in the adaptive optics control algorithm based on pupil tracking is again approximating a further derivative, to acquire $\frac{\partial^2 f}{\partial x^2}$ and $\frac{\partial^2 f}{\partial y \partial x}$ respectively. In a similar way the one row (of lenslets) shift on y axis, $\Delta_y s_x$ and $\Delta_y s_y$ would be calculated by $\frac{\partial^2 f}{\partial x \partial y}$ and $\frac{\partial^2 f}{\partial y^2}$ respectively.

Figure 4.3 shows the plots of Zernike polynomials representing the coma aber-

ration (y axis) $f(x,y) = 3y^3 + 3x^2y - 2y$ and its derivative on x axis $\frac{\partial f}{\partial x} = 6xy$ in cartesian coordinates, made using Matlab 7.5. The surface on the bottom right is three unit shifted coma which is equal to $f(x,y) - 3 \times \frac{\partial f}{\partial x} = 3y^3 + 3x^2y - 18xy - 2y$.

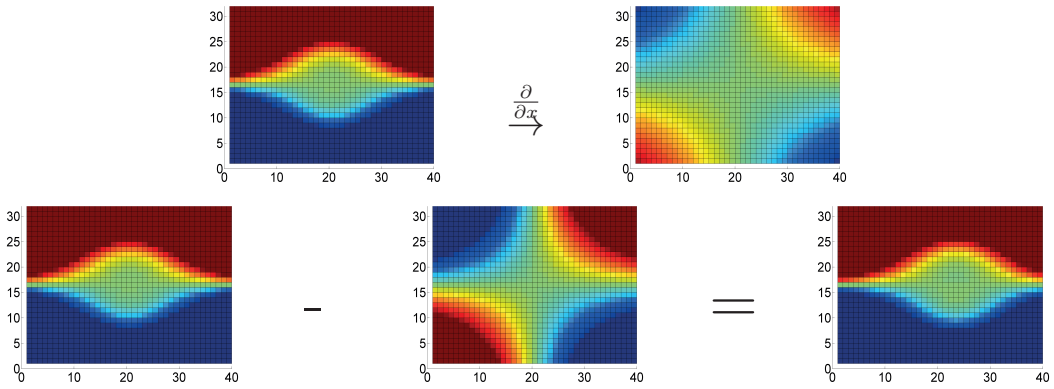

Figure 4.3: Plots of polynomials representing coma (y axis) $f(x,y)$ and its derivative on x axis $\frac{\partial f}{\partial x}$(top), subtraction of $3 \times \frac{\partial f}{\partial x}$ from $f(x,y)$ yields $f(x-3,y)$ (bottom).

Although Figure 4.2 demonstrates the method using wavefront reconstructions, in the execution of adaptive optics algorithm, wavefronts are not reconstructed; only the slopes data which is the derivative of the wavefront aberration is used. The command vector $\mathbf{v}$ is calculated from the $\mathbf{IM}^\dagger$ and the slope vector $\mathbf{s}$ of the last measured wavefront, and then it is applied to the deformable mirror.

In the adaptive optics control algorithm based on pupil tracking the command vectors for the unit shifts for x and y axes are calculated only once at the beginning of a correction by,

$$\begin{aligned} \Delta_x \mathbf{v} &= \mathbf{IM}^\dagger \times \Delta_x \mathbf{s} \\ \Delta_y \mathbf{v} &= \mathbf{IM}^\dagger \times \Delta_y \mathbf{s}, \end{aligned} \tag{4.10}$$

based on the $\mathbf{WF_{Ref}}$, the reference wavefront measurement.

If the pupil displaces $(\Delta x, \Delta y)$ microns on the object plane as measured by the pupil tracker, the wavefront would displace $(\Delta x', \Delta y')$ microns on the wavefront sensor plane and the displacement of the wavefront in terms of lenslets (a, b) is

calculated by,

$$\begin{bmatrix} a \\ b \end{bmatrix} = \frac{1}{l} \begin{bmatrix} \Delta x' \\ \Delta y' \end{bmatrix} \tag{4.11}$$

where l is the pitch *i.e.*, the distance between two lenslet centers. The $\begin{bmatrix} \Delta y' \\ \Delta x' \end{bmatrix}$ depends on the optical set-up and is found by,

$$\begin{bmatrix} \Delta x' \\ \Delta y' \end{bmatrix} = M \times R(\theta) \begin{bmatrix} \Delta x \\ \Delta y \end{bmatrix} \tag{4.12}$$

where M is the magnification and $R(\theta)$ is the rotation of the wavefront as it reaches the wavefront sensor.

Finally, the command vector to correct for a shift of the wavefront of amount (a, b) on the wavefront sensor plane and the final command vector to be applied is calculated by,

$$\begin{aligned} \Delta \mathbf{v}\,(a,b) &= a \times \Delta_x \mathbf{v} + b \times \Delta_y \mathbf{v} \\ \mathbf{v}_1\,(a,b) &= \mathbf{v_0} + \Delta \mathbf{v}\,(a,b)\,, \end{aligned} \tag{4.13}$$

where $\mathbf{v}_0$ is the previous command vector applied to the deformable mirror.

4.3 Simulations done using human eye aberration measurements

A computer program was developed in Labview to simulate the error related to the adaptive optics control algorithm based on pupil tracking using the wavefront aberration data of ten subjects that were recorded with an aberrometer (irx3, Imagine Eyes), for the algorithm of the program see Appendix D, Figure D.1.

First, two different estimates of 2 to 5 rows or columns shifted measurement data were generated using the control algorithm or directly from the data. Their difference was the slopes data of the error of the control algorithm to generate that

shift, *i.e.*, ${}^{n}_{x}s_{x_{ij}}$ and ${}^{n}_{x}s_{y_{ij}}$,

$$\begin{aligned} {}^{n}_{x}s_{x_{ij}} &= s_{x_{i+n,j}} - \left(s_{x_{ij}} + n \times \Delta_x s_{x_{ij}}\right) \\ {}^{n}_{x}s_{y_{ij}} &= s_{y_{i+n,j}} - \left(s_{y_{ij}} + n \times \Delta_x s_{y_{ij}}\right) \end{aligned} \tag{4.14}$$

where $n = \{2, 3, 4, 5\}$, $i = \{1, 2, \ldots, 32\}$ and $j = \{1, 2, \ldots, 40\}$, see Table 4.1.

(a)

N	N	N	N	N	N	N
N	N	N	1	N	N	N
N	N	1	1	1	N	N
N	1	1	1	1	1	N
N	N	1	1	1	N	N
N	N	N	1	N	N	N
N	N	N	N	N	N	N

(b)

N	N	N	N	N	N	N
N	N	N	N	1	N	N
N	N	N	1	1	1	N
N	N	1	1	1	1	1
N	N	N	1	1	1	N
N	N	N	N	1	N	N
N	N	N	N	N	N	N

(c)

N	N	N	N	N	N	N
N	N	N	N	N	N	N
N	N	N	0	0	N	N
N	N	0	0	0	0	N
N	N	N	0	0	N	N
N	N	N	N	N	N	N
N	N	N	N	N	N	N

Table 4.1: The slopes data showing the effective pupil of the measurement by 1 and N denotes ***not a number***. The initial slopes data (a), the one column (of lenslets) shifted slopes data (b), and their difference which represents one unit shift on x axis (c).

For instance to calculate ${}^{2}_{x}s_{x_{ij}}$ and ${}^{2}_{x}s_{y_{ij}}$, the slopes data of the residual error of the control algorithm for a shift of two columns (of lenslets) on x axis, the original slopes matrix was summed by twice the derivative of the slopes and the resulting matrix was subtracted from the two lenslet shifted original matrix. The same procedure was repeated to calculate ${}^{n}_{y}s_{x_{ij}}$ and ${}^{n}_{y}s_{y_{ij}}$, the slopes data of the error of the control algorithm for a shift of n rows (of lenslets) on y axis,

$$\begin{aligned} {}^{n}_{y}s_{x_{ij}} &= s_{x_{i,j+n}} - \left(s_{x_{ij}} + n \times \Delta_y s_{x_{ij}}\right) \\ {}^{n}_{y}s_{y_{ij}} &= s_{y_{i,j+n}} - \left(s_{y_{ij}} + n \times \Delta_y s_{y_{ij}}\right) \end{aligned} \tag{4.15}$$

where $n = \{2, 3, 4, 5\}$, $i = \{1, 2, \ldots, 32\}$ and $j = \{1, 2, \ldots, 40\}$.

Using ${}^{n}_{x}s_{x_{ij}}$ and ${}^{n}_{x}s_{y_{ij}}$, the ${}^{n}_{x}\mathbf{WF}$, *i.e.*, the residual error wavefront for n columns shift on x axis, and using ${}^{n}_{y}s_{x_{ij}}$ and ${}^{n}_{y}s_{y_{ij}}$, the ${}^{n}_{y}\mathbf{WF}$, *i.e.*, the residual error wavefront for n rows shift on y axis were reconstructed by zonal reconstruction and their RMS were calculated, Figure 4.4.

In Figure 4.4, *a* and *b*, the displacements from 2 to 5 lenslets on the wavefront

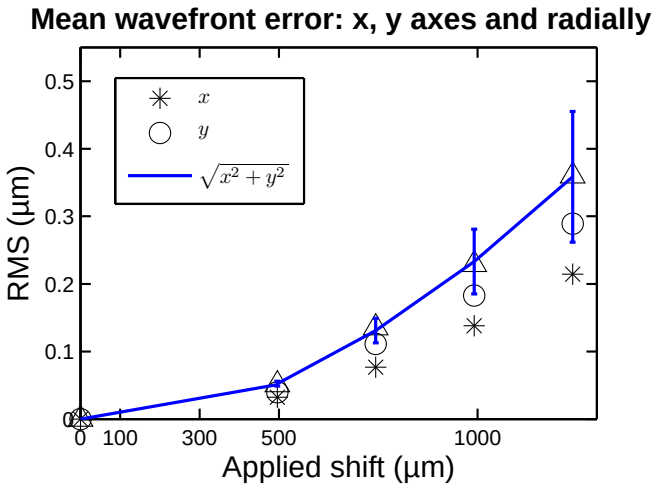

Figure 4.4: Mean of the RMS of the residual wavefront error of the control algorithm in generating shifted wavefronts on x and y axis, calculated from real eye wavefront measurements of 10 subjects.

sensor plane for x and y axes respectively, were converted to displacements in microns on the object plane by,

$$\begin{bmatrix} \Delta x \\ \Delta y \end{bmatrix} = n \times \frac{l}{M} \begin{bmatrix} a \\ b \end{bmatrix} \tag{4.16}$$

where $l = 114$ μm is the distance between two lenslet centers and $M = 0.46$ is the magnification of the optical system. According to the simulations which were done for 10 aberration measurements, for the pupil displacements of up to 500 microns, the mean wavefront error related to the method was less than 50 nm.

A better evaluation of the results could be done with the knowledge of range of fixational eye movements. A study was made among healthy subjects and it was found that a healthy fixating eye displaces $\sim 40 \pm 10$ μm in 50 ms, the error related to the method was low enough to work with.

4.3.1 Statistics of fixational eye movements

Pupil center position of 10 subjects was measured every $\sim$ 12 ms during $\sim$ 13 s several times. In total $\sim 72 \times 13$ s of recordings of measurements were used to estimate the average pupil movement (total movement summed up during the time

indicated) and displacement (difference between initial and final positions) in $\sim$ 12, 50 and 100 milliseconds. 50 and 100 ms are the time durations in which four and eight pupil tracking measurements can take place respectively, Figure 4.5.

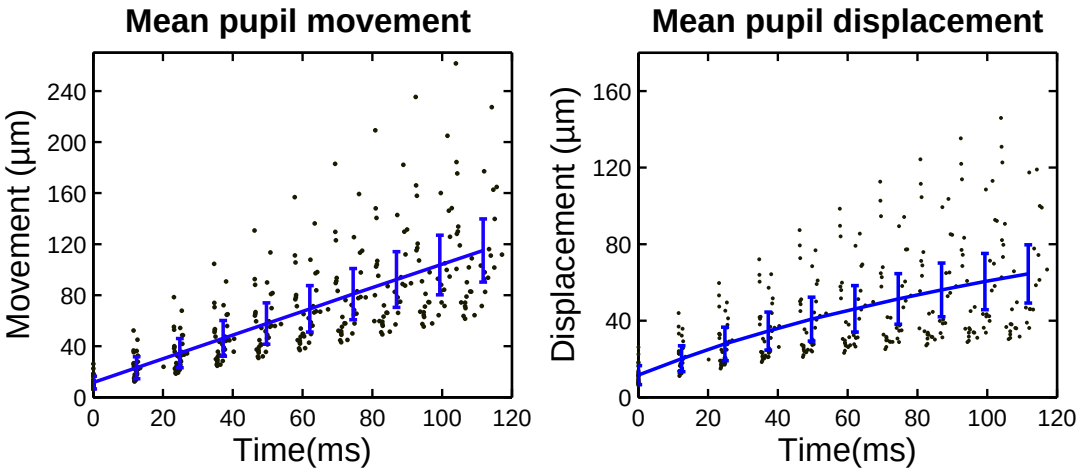

Figure 4.5: Mean pupil displacements (difference between initial and final positions) and movements (total movement summed up during the time indicated) of 10 healthy fixating subjects.

The pupil displacement was always smaller than the total pupil movement and the former had a linear relationship with time while the latter had an upper limit and was nonlinear, see Figure 4.5. The eye was keeping its position at and around the central vision, as confirmed by the recordings of the fixational eye movements. For instance in 50 ms the pupil moved $\sim 60 \pm 10$ μm while its displacement from its first position was $\sim 40 \pm 10$ μm. Again the pupil moved $\sim 100 \pm 20$ μm in 100 ms but its displacement from its first position was $\sim 60 \pm 10$, see also Figure 4.6.

4.4 Initial experiments with a model eye

First experiments were performed using the model eye, the adaptive optics retinal camera, its control software Casao, and the computer program developed in Labview to execute the adaptive optics control algorithm based on pupil tracking. The program's parts related to the instrumentation control was developed using the software development kit provided by the Casao software so that it would be compatible with it, for the algorithm of the program see Appendix D, Figure D.2.

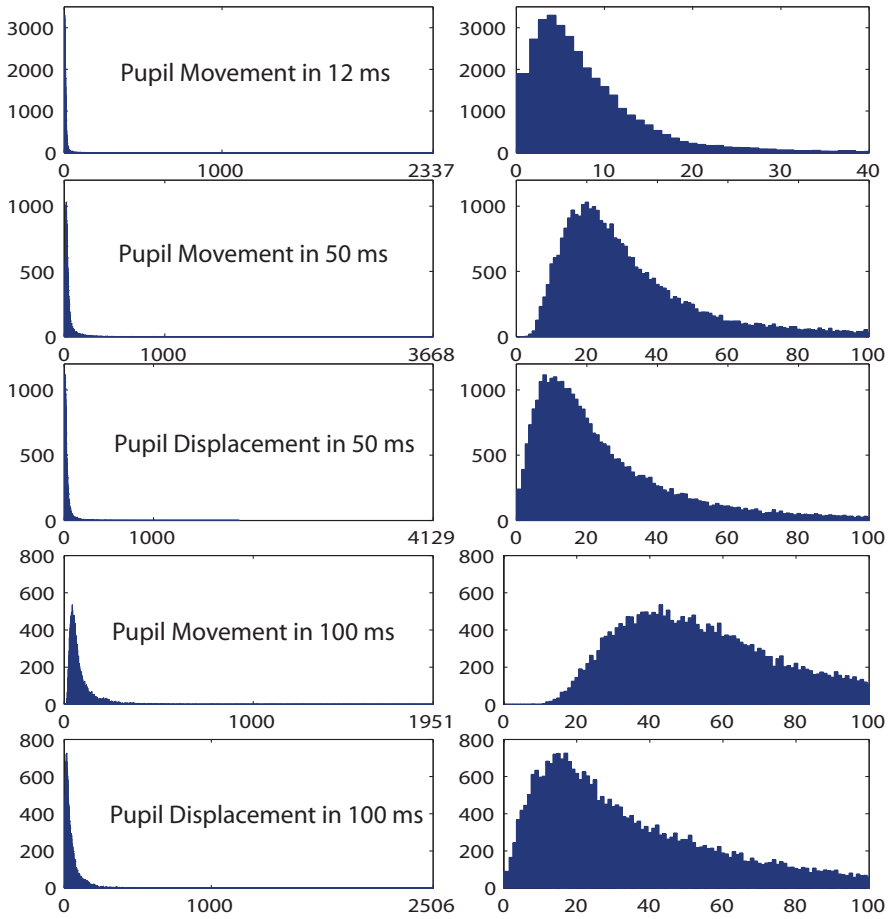

Figure 4.6: Histograms of the pupil displacements (difference between initial and final positions) and movements (total movement summed up during the time indicated) of 10 healthy fixating subjects in ***microns***. The right column shows a closer look at the histograms of the left column. For instance maximum pupil displacement in 50 ms was 4129 μm (left) while the majority of the displacement took place in $\sim 40\mu$m range.

To be able to perform the experiments, firstly, it was necessary to calibrate the system and the computer program.

4.4.1 Calibration

There were four important factors in the set-up to be calibrated; the interaction matrix of the adaptive optics system, the magnification and the rotation factors of the adaptive optics retinal camera's optics and the reference wavefront measurement.

The interaction matrix

For each aberration measurement the wavefront sensor provides the slope data, s_x and s_y in which only the effective pupil area is filled with slope information, Table 4.2 - b and c. The effective pupil area depends on first, the pupil of the subject and then the entrance pupil of the system except the case of the interaction matrix registration. The interaction matrix registration is done using an internal light source which circulates only between the wavefront sensor and the deformable mirror and is not limited by the entrance pupil of the system, therefore the pupil of the interaction matrix is always equal or larger than the pupil of the measurement of an outside object, see Table 4.2 - a and b.

(a)

0	0	0	0	0	0	0
0	0	0	1	0	0	0
0	0	1	1	1	0	0
0	1	1	1	1	1	0
0	0	1	1	1	0	0
0	0	0	1	0	0	0
0	0	0	0	0	0	0

(b)

0	0	0	0	0	0	0
0	0	0	0	0	0	0
0	0	0	1	0	0	0
0	0	1	1	1	0	0
0	0	0	1	0	0	0
0	0	0	0	0	0	0
0	0	0	0	0	0	0

(c)

N	N	N	N	N	N	N
N	N	N	N	N	N	N
N	N	N	0.7	N	N	N
N	N	0.9	1.5	2	N	N
N	N	N	1.2	N	N	N
N	N	N	N	N	N	N
N	N	N	N	N	N	N

(d)

N	N	N	N	N	N	N
N	N	N	0	N	N	N
N	N	0	0.7	0	N	N
N	0	0.9	1.5	2	0	N
N	N	0	1.2	0	N	N
N	N	N	0	N	N	N
N	N	N	N	N	N	N

(e)

N	N	N	N	N	N	N
N	N	N	2.1	N	N	N
N	N	3	0.7	-1.3	N	N
N	0.1	0.9	1.5	2	2.3	N
N	N	0.9	1.2	0.6	N	N
N	N	N	1.1	N	N	N
N	N	N	N	N	N	N

(f)

N	N	N	N	N	N	N
N	N	N	0	N	N	N
N	N	0	-2.3	-2	N	N
N	0	0.8	0.6	0.5	-0.3	N
N	N	0	0.3	-0.6	N	N
N	N	N	0	N	N	N
N	N	N	N	N	N	N

Table 4.2: Representations for data provided by a 7×7 lenslet array wavefront sensor, N denotes ***not a number***. The pupil of measurements for the interaction matrix (a) is always equal or larger than the pupil of the aberration of an object (b). The slope data *i.e.*, s_x or s_y exists only on this effective pupil area, (b) and (c). The slope vector is formed using s_x and s_y after the missing points are filled with zeros based on the pupil of the **IM**, (a) and (d). Starting with slopes data of (e) the pupil of the slopes vector of the derivative is smaller because of the truncation due to the subtraction of the one column shifted data (f).

For example let's suppose we have a $7 \times 7 = 49$ lenslet wavefront sensor and a 4 actuator deformable mirror, Table 4.2. Using the internal light source we

pushed and pulled each actuator of the deformable mirror, recorded the slopes data, s_x and s_y with an effective pupil of 13 data points each, formed a slopes vector $\mathbf{s} = [s_{x_1}, s_{x_2}, \ldots, s_{x_{13}}, s_{y_1}, s_{y_2}, \ldots, s_{y_{13}}]^T$ with the size 26×1 for each actuator and finally constructed the interaction matrix $\mathbf{IM} = [\mathbf{s_1}, \mathbf{s_2}, \mathbf{s_3}, \mathbf{s_4}]$ with the size 26×4, see Table 4.2 - a. This interaction matrix sets the language between the wavefront sensor and the deformable mirror and shall be used in the adaptive optics system correction. Let's suppose we want to correct an aberration which had a smaller pupil than the interaction matrix had, Table 4.2 - b and c. First we measure the aberration and form the slopes vector for the measurement $\mathbf{s_{mes}} = [s_{x_1}, s_{x_2}, \ldots, s_{x_5}, s_{y_1}, s_{y_2}, \ldots, s_{y_5}]^T$ with size 10×1. To calculate the command vector sized 4×1, using $\mathbf{v} = \mathbf{IM}^\dagger \times \mathbf{s}$ we have to be able to multiply the 4×26 sized $\mathbf{IM}$ with 10×1 sized $\mathbf{s_{mes}}$ which is not possible.

The solution to overcome this problem in an adaptive optics control algorithm is to use the effective pupil of the interaction matrix to build an 26×1 sized $\mathbf{s_{mes}}$ after filling the gaps with zeros, *i.e.* $\mathbf{s_{mes}} = [0,\ 0,\ s_{x_1},\ 0,\ 0,\ s_{x_2},\ s_{x_3},\ s_{x_4},\ 0,\ 0,\ s_{x_5}, \ldots$ $0,\ 0,\ 0,\ 0,\ s_{y_1},\ 0,\ 0, s_{y_2}, s_{y_3},\ s_{y_4},\ 0,\ 0,\ s_{y_5},\ 0,\ 0]^T$, see Table 4.2 - d. This would over-estimate the actual aberration and the resulting correction would span a larger area but since the pupil of the aberration is restricted to the central part, the edges would not affect the correction.

On the other hand the correction would be erroneous for our case because of the shifts in the data matrices this over-estimation is done within the pupil area that we are trying to correct for. For instance, Table 4.2 - f shows the case where there are five data points that were over-estimated and added to the derivative of the slopes data. This problem can only be overcome by doing the opposite of the usual adaptive optics algorithm; by reducing the size of the interaction matrix to correspond to the pupil of the measured slopes vector. This solution could not be applied in the ordinary adaptive optics loop because it would take a lot of time to modify an interaction matrix sized 1024×52 at each loop, but for our case this will not affect the loop speed because this modification will take place only at the

beginning of the correction once, then the same calculated derivative command vectors will be used continuously.

Coordinate transformation

The wavefront entering the adaptive optics retinal camera is modified in two ways; it is reduced in size and rotated due to the several mirrors on the optical pathway that are placed to maintain the size of the device as compact as possible in spite of its complexity. In the adaptive optics control algorithm any modification of the wavefront between the wavefront sensor and the deformable mirror is taken into account with the interaction matrix, as the interaction matrix is the mapping of this pathway. Although it is not important for the control algorithm based on wavefront sensing, to correct the aberrations based on pupil tracking it is obligatory to know exactly the correspondence of a certain amount of displacement on the pupil plane (as measured by pupil tracking) to the displacement on the wavefront sensor plane. With the knowledge of magnification M, and the rotation θ in the optics for the wavefront sensor, the displacement of the wavefront $(\Delta x', \Delta y')$, can be estimated from the displacement of the pupil $(\Delta x, \Delta y)$ by,

$$\begin{bmatrix} \Delta x' \\ \Delta y' \end{bmatrix} = M \begin{bmatrix} cos\theta \ sin\theta \\ -sin\theta \ cos\theta \end{bmatrix} \begin{bmatrix} \Delta x \\ \Delta y \end{bmatrix} \tag{4.17}$$

The line profile of the aberration of the model eye was used to find the degree of rotation of the wavefront, Figure 4.7.

The model eye was attached to a micrometer translation stage which was also attached to a rotating stage, having 10 microns and 1° resolution respectively, as shown in Figure 4.9. Observing the parabola like line profile of the wavefront surface on x axis via Haso software, the model eye was displaced along the translation stage while the stage was rotated between 110 to 130°. At $\sim 119 \pm 1°$ it was possible to move the model eye vertically without a significant deviation of the minimum of the line profile of the wavefront. Taking into account the 1° offset

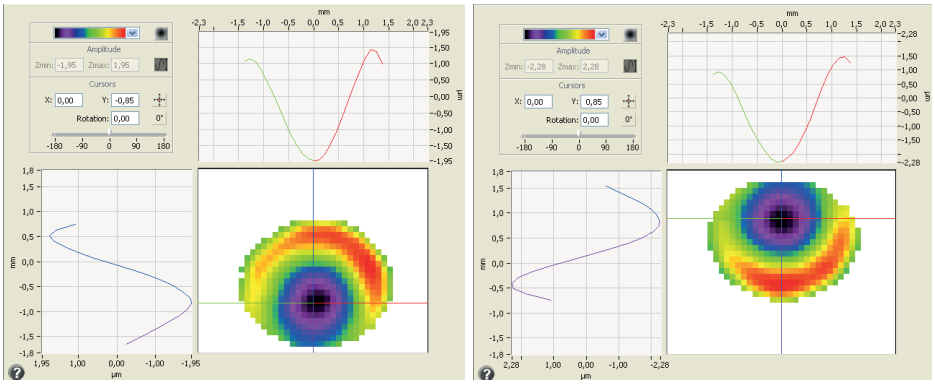

Figure 4.7: The line profiles of the spherical aberration on x and y axes, after the stage was rotated and the model eye was moved along the axis of the stage upwards (right) and downwards (left).

rotation of the stage, the rotation of the system was estimated as 120°.

When the translation stage was rotated at 119 ± 1° (plus 1° offset of the base of the set up), the movement of the model eye on the translation stage corresponded to the movement of the wavefront vertically on the wavefront sensor plane, the shape of the line profile did not change, see Figure 4.8.

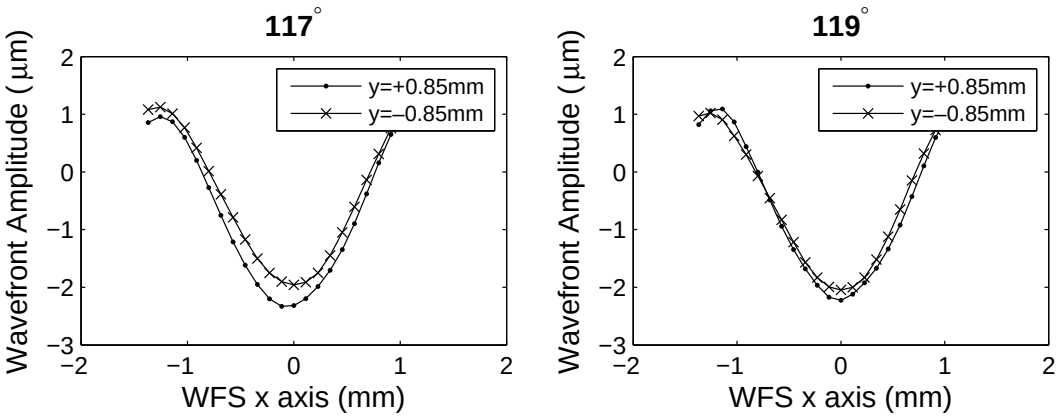

Figure 4.8: The resemblance of the line profiles of the spherical aberration at the two extremities of the stage at the rotations of 117° (left) and 119° (right).

Magnification

In theory, the wavefront that reaches the wavefront sensor was reduced in size by the magnification factor of 0.45. On the other hand because of the imperfections in the optical elements and the assembly errors, this magnification factor was slightly different than 0.45. The focal spots were observed on the wavefront sensor

to estimate the reduction factor in size.

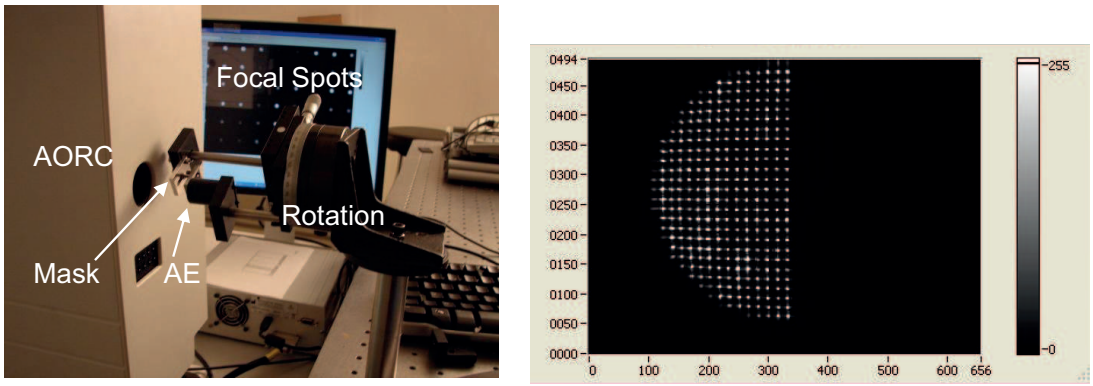

Figure 4.9: The model eye with a sliding mask before it is placed in front of the adaptive optics retinal camera (AORC) (left) and focal spots as seen by the wavefront sensor (right).

Figure 4.9 shows the set-up prepared, where the 119° rotated translation stage held the model eye and a mask in front of it (left) and the wavefront sensor camera image where x and y axes are in pixels and each pixel of the camera corresponded to 7.4 microns (right). The model eye was stable while the mask was moving over it and it was possible to observe the disappearance of the aberration focal spots column by column at a closer look to the image where the pixels were resolvable. In average 250 ± 10 μm of shift on the object plane resulted in disappearance of one row of lenslets which corresponded to a magnification power of 0.46 ± 0.04 by $M = \frac{l}{\Delta x}$ where $l = 114$ μm is the distance between each lenslet center and $\Delta x = 250$ μm is the displacement of the pupil.

The reference wavefront

$\mathbf{WF_{Ref}}$ is the reference wavefront measurement that represents the aberrations of the eye. The more the $\mathbf{WF_{Ref}}$ is close to the true aberrations of the eye the better the control algorithm based on pupil tracking can compensate for the changes of the aberrations based on pupil displacements. For this reason a $\mathbf{WF_{Ref}}$ measurement is taken before the start of the corrections while the eye is well centered with respect to the system.

$\mathbf{WF'_{Ref}}$ is a measure of the aberrations of the eye plus the aberrations of the

system therefore the true aberrations of the eye as measured by the wavefront sensor should be,

$$\mathbf{WF_{Ref}} = \mathbf{WF'_{Ref}} - \mathbf{WF_{Sys}} \tag{4.18}$$

where $\mathbf{WF_{Sys}}$ is the aberrations of the system. A way to estimate the true aberrations of the eye was to measure the aberrations of the system and then subtract this from the $\mathbf{WF'_{Ref}}$, see Figure 4.10.

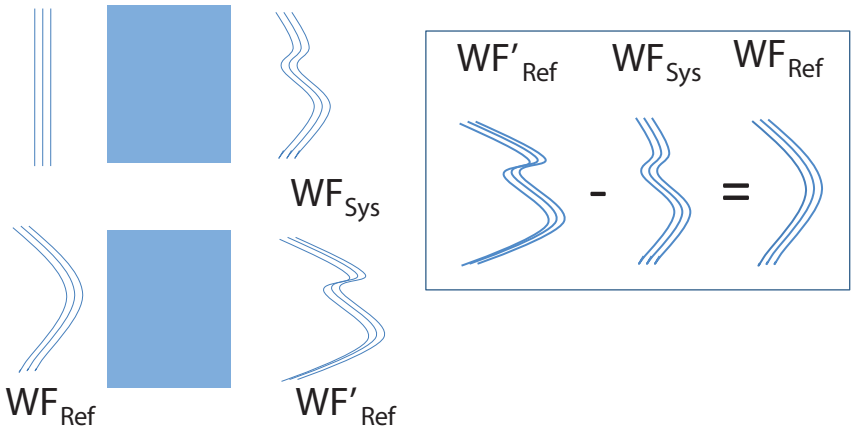

Figure 4.10: The plane wavefront passing through the system was aberrated as it reached the wavefront sensor (left top). $\mathbf{WF_{Ref}}$ had the $\mathbf{WF_{Sys}}$ superimposed on when it reached the wavefront sensor (left bottom). To retrieve $\mathbf{WF_{Ref}}$, it was necessary to subtract $\mathbf{WF_{Sys}}$ from $\mathbf{WF'_{Ref}}$.

$\mathbf{WF_{Sys}}$ could be measured using a model eye[2] that had no aberrations, because the initially plane wavefront was aberrated as it proceeded in the optical system and represented the aberrations of the optical path starting from the entrance pupil to the wavefront sensor when measured.

The aberrations of the system (as measured using the model eye with no aberrations) excluding the tilt and defocus terms was ~ 0.36 μm RMS being mostly astigmatism some of it originating from the instabilities of the surface of the deformable mirror when no voltages were applied on the surface. Memory of previous measurements, small changes in the reflective surface because of internal or external factors such as heating of the electronics caused a slightly different $\mathbf{WF_{Sys}}$. We decided to try a different method which could be more reliable, see Figure

[2]see Appendix C, Figures C.3 and C.4

4.11.

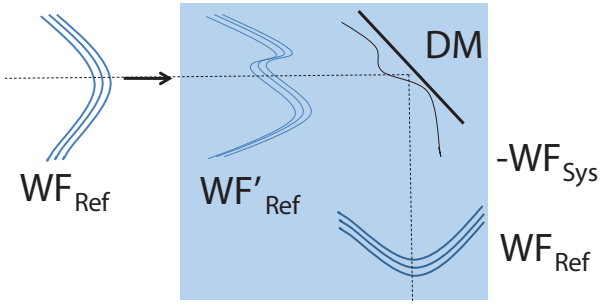

Figure 4.11: The deformable mirror (DM) corrects for the $\mathbf{WF_{Sys}}$ so that the reference wavefront of the eye, the $\mathbf{WF_{Ref}}$ reaching the wavefront sensor is free from the aberrations of the system.

This case we corrected for the aberrations of the system with the deformable mirror and saved the command vector $\mathbf{v_{Sys}}$. Each time the control algorithm based on pupil tracking was used to correct for the aberrations of the eye, before the correction the $\mathbf{WF_{Ref}}$ was measured after the deformable mirror was uploaded by the $\mathbf{v_{Sys}}$ to correct for $\mathbf{WF_{Sys}}$.

4.4.2 Method and results

The model eye was attached to a micrometer system and was placed in front of the adaptive optics retinal camera. The experiments started first by producing an interaction matrix, then the procedure was as follows:

- upload $\mathbf{v_{Sys}}$[3],
- measure and save the $\mathbf{WF_{Ref}}$[4] using Casao[5],
- correct the aberrations with control algorithm based on wavefront sensing, using Casao,
- export the deformable mirror command vector $\mathbf{v_0}$, the interaction matrix and the aberration data s_x and s_y,

[3]the deformable mirror command vector to subtract the aberrations of the system from the reference aberration measurement

[4]The reference measurement of the wavefront aberrations of the eye whose derivative is used in the control algorithm based on pupil tracking (WF_{Ref})

[5]the commercial software by Imagine Eyes that controls the adaptive optics instruments in the retinal camera

- using the data exported and the control algorithm based on pupil tracking calculate $\Delta_x \mathbf{v}$ and $\Delta_y \mathbf{v}$,
- displace the model eye by an amount of $(\Delta x, \Delta y)$,
- the adaptive optics correction was lost: calculate (a, b) the displacement on the wavefront sensor plane and $\Delta \mathbf{v}\,(a, b) = a \times \Delta_x \mathbf{v} + b \times \Delta_y \mathbf{v}$,
- calculate the next command vector $\mathbf{v}_1\,(a, b) = \mathbf{v_0} + \Delta \mathbf{v}\,(a, b)$,
- apply $\mathbf{v}_1\,(a, b)$ to the deformable mirror to restore the correction,
- repeat the last four steps for different amounts of displacements $(\Delta x, \Delta y)$.

Figure 4.12 displays the RMS of the wavefronts recorded at each step.

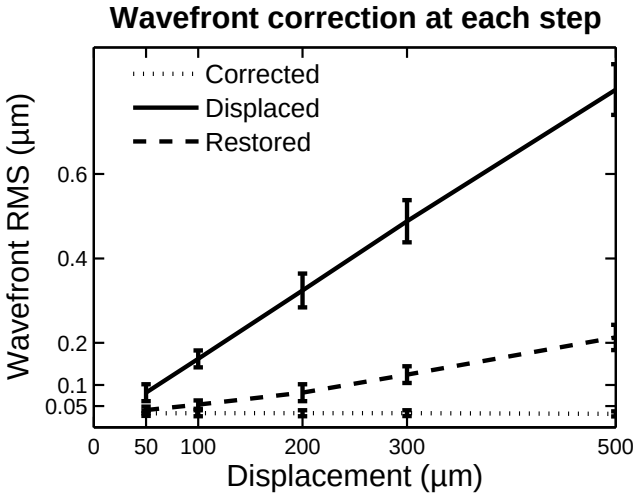

Figure 4.12: The RMS of the wavefronts at each step; first, the aberration of the model eye was corrected with the adaptive optics algorithm based on wavefront sensing (dotted line), second, model eye was shifted and the correction was lost (solid line), finally the deformable mirror was run using the commands calculated by the control algorithm based on pupil tracking (dashed line).

Figure 4.13 displays the summary of simulations done with real eye measurements with the model eye and the experiments done with the model eye. Experimental results with the model eye which had an aberration RMS of 1.1 ± 0.5 microns might not have been relevant to compare with *in vivo* simulation results which had a much smaller RMS value, so the simulations were repeated for the

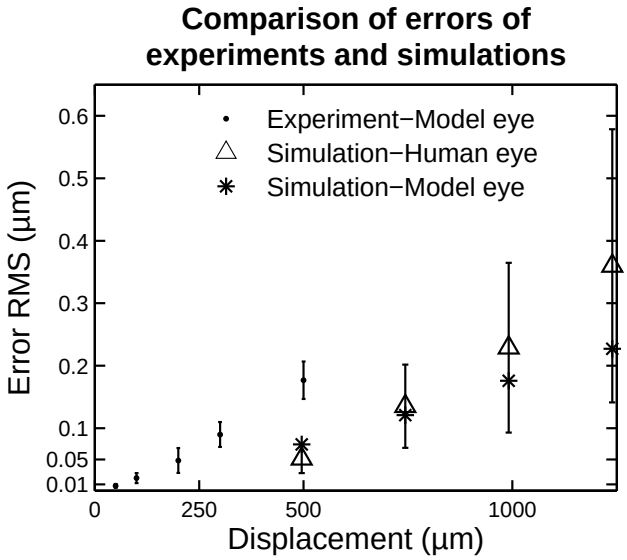

Figure 4.13: Residual wavefront RMS of the experiments done using the model eye and the simulations done using human eye and model eye aberration measurements.

model eye. In spite of this, a significant difference could be seen between simulations and experimental results which can be explained by the effective pupil of the measurement. In the simulations, as the wavefront slopes data shifts to the right, the emptied data points on the left edge of the pupil are left empty. In the experiments as the model eye was shifted to right, the far left side of the pupil was filled with new data which the control algorithm based on pupil tracking did not recognize because of the fact that the model eye had a larger pupil than the system.

The mean RMS error in the experiments was 0.008 μm for a 50 μm displacement which was sufficient considering that the lowest RMS values that can be achieved by the adaptive optics system of the retinal camera was $\sim$ 0.015 μm to correct the aberrations between the wavefront sensor and the deformable mirror using the internal light source, $\sim$ 0.036 μm for the correction of the wavefront aberrations of the model eye and 0.050-0.15 μm in vivo. A correction as good as at least $\sim$ 0.15 μm RMS is a must for a good retinal image although it does not guarantee good images as there are other factors that affect retinal image quality.

4.5 Discussion

The control algorithm was tested by simulations and by experiments using computer programs that were not completely automatic, that did not acquire the pupil position from the pupil tracker and that sought the help of Casao. The results showed that the control algorithm based on pupil tracking provided a good estimate of a shifted wavefront and the calibrations of the system was successful.

To correct for the aberrations real time we developed a fully automated computer program that acquired the information from the pupil tracker and compensated for the aberrations using both the control algorithm based on pupil tracking and wavefront sensing which is the subject of the next chapter.

Chapter 5

Experiments real time

A computer program that can control the adaptive optics components of the retinal imaging system and correct for the ocular aberrations using the two control algorithms based on wavefront sensing and pupil tracking was developed. A brief description of software development process is given in the next section followed by the experimental results.

5.1 Software development

The deformable mirror and the wavefront sensor of the retinal camera were a part of a package commercialized by Imagine Eyes that included an adaptive optics control software, Casao. The Casao control software was build up using small modules of programs written in C++ and Labview which were also supplied by the manufacturer in a software development kit for a custom control of the mirao 52-e deformable mirror and the HASO 32-eye wavefront sensor. The adaptive optics control algorithm based on pupil tracking was written partially using this software development kit.

All the cameras and the light sources within the retinal imaging system were synchronised in time, controlled by the PulseBlaster TTL pulse generator using which the cameras and the light sources could be sent the desired trigger (rising or falling) at the desired time and duration. A typical synchronisation of the

components of retinal camera in an imaging session is illustrated in Figure 5.1.

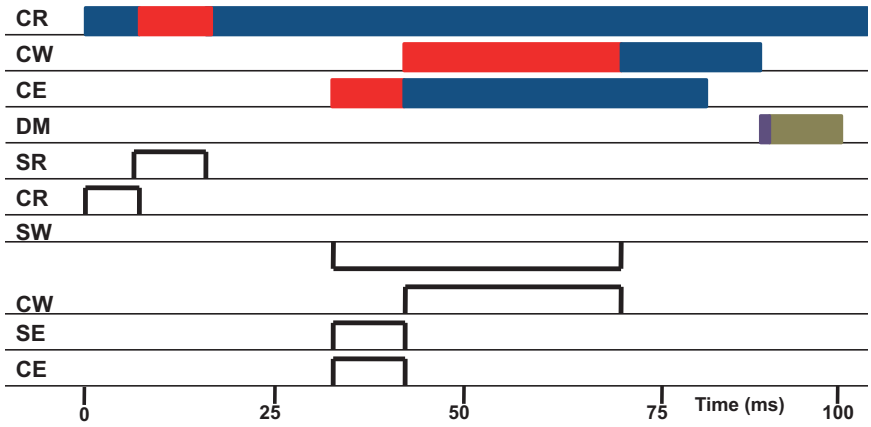

Figure 5.1: Chronogram of the elements of the adaptive optics retinal camera (top - colored) and the trigger times (bottom). The red portion stands for the exposure time of the each camera and dark blue portion stands for the time required for the acquisition being, 9 and 96 ms for the camera for retinal imaging (CR), 30 and 17 ms for the camera for wavefront sensing (CW), 10 and 40 ms for the camera for aligning the eye and pupil tracking (CE), respectively (top - colored). The adaptive optics control algorithm (purple) takes a few milliseconds to calculate and sends the commands to the deformable mirror (DM) which is not triggered and takes maximum 15 ms to execute the commands and stabilize. SE, SR and SW stand for light sources for eye, retinal imaging and wavefront sensing respectively.

The trigger for the retinal imaging camera started before the trigger for the retinal imaging source because there was a default delay in the onset of the exposure of the retinal imaging camera. The trigger for the wavefront sensing light source was inverse because this super luminescent diode was triggered by a falling signal, unlike the others.

The eye camera of the retinal imaging system worked in triggered mode while the eye camera of the previously described pupil tracking system was working in continuous mode and had a different frame grabber. Adapting the pupil tracking to the retinal imaging system meant the piece of C++ code that acquired the image to serve the pupil tracking algorithm had to be re-written. It was basically a library of functions using which it was possible to open, get the image each time a trigger arrived, run the pupil tracking algorithm or close the eye camera. The position of the pupil would be calculated at each trigger; as long as the trigger was applied at the right time; after the end of acquisition and the processing of

the previous image by the camera, otherwise the user would see a blank frame.

After the new library was written by the software engineers at Imagine Eyes, the pupil tracking algorithm and the library functions were used to make the pupil tracking functional again to work in triggered mode in the retinal camera. However, the upgraded pupil tracking system did not have 85 Hz frame rate; for a reason still unknown the camera now could work at a maximum of 20 Hz frame rate. This meant that the eye had 50 ms instead of 12 ms to move after the pupil tracker camera started the image exposure (that takes 10 ms) and would decrease the accuracy of the pupil tracker measurements. To be able to do two consecutive pupil tracking measurements that took 50 ms each, which was necessary for one adaptive optics loop with both wavefront sensing and pupil tracking to execute, the loop had to take 120 ms minimum instead of a 100 ms of loop duration normally. For this reason, unless otherwise stated all the experiments was performed with a loop rate of ~ 8.35 Hz.

The final software that controlled the adaptive optics with pupil tracking was written using both C++ and Labview where appropriate. For instance the pupil tracking algorithm was written in C++, its functions were converted into a library with .dll extension and a module was written in Labview that calls these functions via the .dll file. By this way it was possible to exploit the ease of the Labview user interface and the robustness of the C++ language.

After the programming and the calibrations, it was possible to form different types of loops using these five following components:

- the deformable mirror
- the wavefront sensor
- the control algorithm based on wavefront sensor measurements
- the pupil tracking system
- the control algorithm based on pupil tracking measurements

Using these tools five types of loops (i.e., in a general sense means repeating measurements of the same kind) were designed and experiments with a model eye and experiments *in vivo* were performed.

The first loop took continuous wavefront sensor and pupil tracking measurements without the control algorithms or the deformable mirror. Figure 5.2 illustrates the synchronisation of the cameras of the wavefront sensor and the pupil tracker in this loop which was named 'WFPT' for future reference.

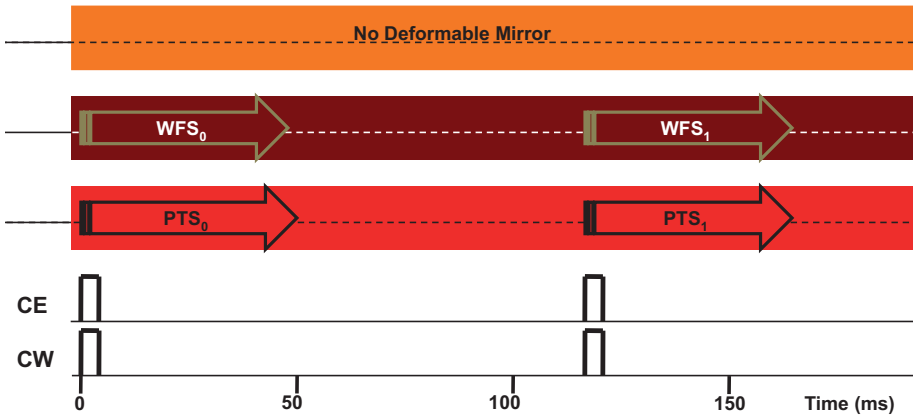

Figure 5.2: The WFPT loop: the eye camera for pupil tracking (CE) and the camera for wavefront sensing (CW) were triggered at the same time. Each loop takes 120 ms and WFS_0 and PTS_0 stands for the first wavefront sensor and the pupil tracking measurements respectively.

The second loop which was named 'AOPT' was illustrated in Figure 5.3.

The second loop took continuous wavefront sensor and pupil tracking measurements while doing adaptive optics correction using the deformable mirror and the adaptive optics control algorithm based on wavefront sensor measurements.

The third loop, first corrected the aberrations of the eye using the AOPT[1] loop and then keeping the deformable mirror at the latest correction shape, measured the wavefront aberrations and pupil positions of the eye. Figure 5.4 illustrates the timing and functioning of the elements in this loop which was called 'WFPTa' for future reference.

The Figure 5.5 illustrates the layout of the fourth loop named 'AOPTL1' . This

[1]Loop which incorporates the wavefront sensor, the deformable mirror, the pupil tracker and the control algorithm based on wavefront sensing (AOPT)

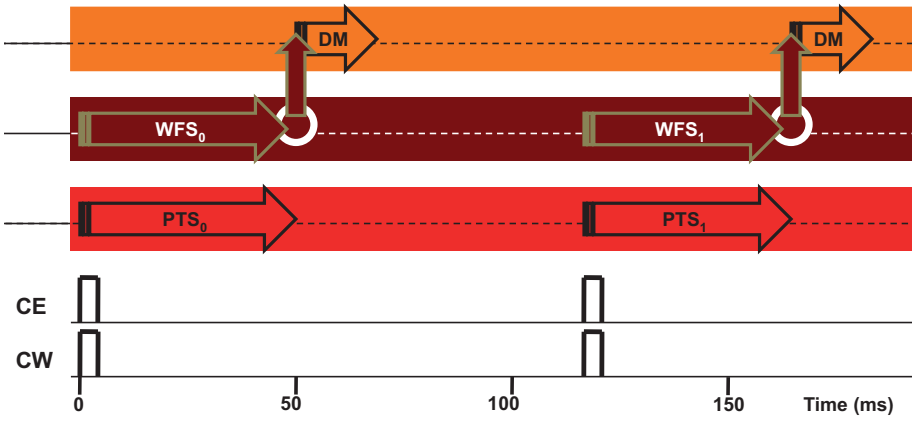

Figure 5.3: The AOPT loop: the eye camera for pupil tracking (CE) and the camera for wavefront sensing (CW) were triggered at the same time while the deformable mirror (DM) was given the commands from the adaptive optics control (shown as the white ring) based on wavefront sensor data. WFS_0 and PTS_0 stands for the first wavefront sensor and pupil tracking measurements respectively.

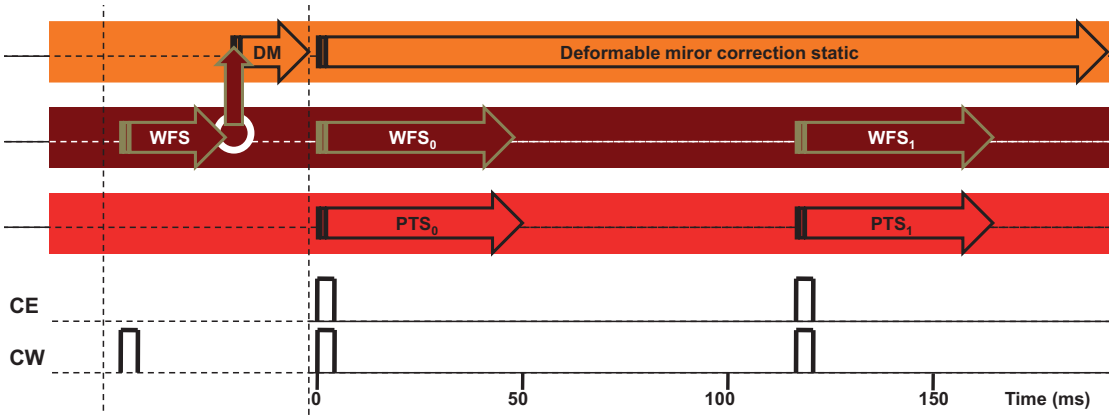

Figure 5.4: The WFPTa loop: the eye camera for pupil tracking (CE) and camera for wavefront sensing (CW) were triggered at the same time while the deformable mirror (DM) was kept constant at the latest correction shape. WFS_0 and PTS_0 stands for the first wavefront sensor and the pupil tracking measurements respectively.

loop constituted the wavefront sensor, the deformable mirror, the pupil tracker and the adaptive optics control algorithm based on pupil tracking measurements; it used the control algorithm based on wavefront sensor measurements only at the beginning of the loop.

First, $\mathbf{WF_{Ref}}$, the reference wavefront of the eye and its pupil position was measured and $\Delta\mathbf{v_x}$ and $\Delta\mathbf{v_y}$ the command vectors for the unit shifts were calculated to be used in the course of the correction by the adaptive optics control algorithm based on pupil tracking. After the aberrations of the eye were corrected

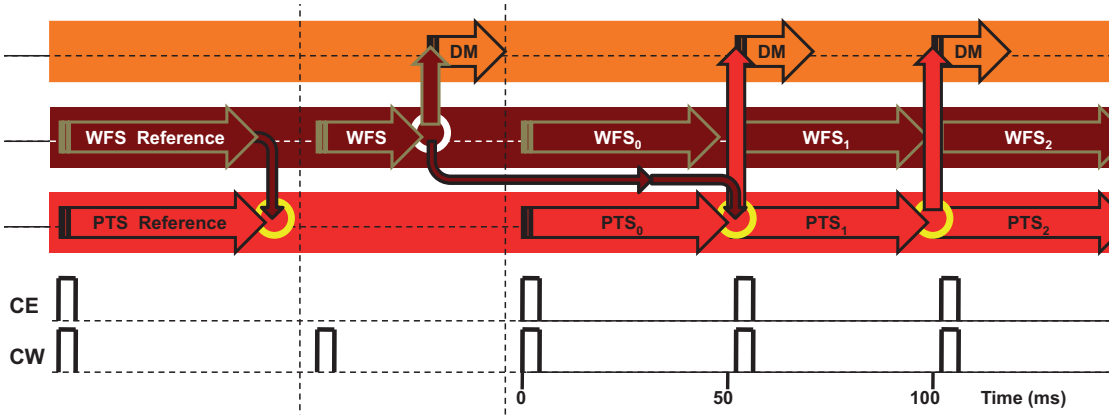

Figure 5.5: The AOPTL1 loop: the eye camera (CE) and the camera for wavefront sensor (CW) were shown triggered at 20 Hz although during the experiments unless stated otherwise the rate of the loop was $\sim$ 8.35 Hz. The correction done using the control algorithm based on wavefront sensing (the white ring) was updated by the commands calculated by the control algorithm based on pupil tracking (the yellow ring).

using the control algorithm based on wavefront sensor measurements, in the loop, the correction was updated for the displacements of the pupil where the pupil tracker was called once in a loop.

Finally, the fifth loop was a more complicated adaptive optics loop which constituted all the five elements; the wavefront sensor, the deformable mirror, the first control algorithm to calculate the commands based on wavefront sensor measurements, the pupil tracker and the second control algorithm to calculate the commands based on the pupil tracker measurements. Figure 5.6 illustrates the functioning and timing of the adaptive optics components in this loop which was named 'AOPTL2'.

Before the correction started, $\mathbf{WF_{Ref}}$, the reference wavefront was measured and $\Delta\mathbf{v_x}$ and $\Delta\mathbf{v_y}$, the command vectors for the unit shifts were calculated to be used in the course of the correction by the adaptive optics control algorithm for pupil tracking. The wavefront sensor and the pupil tracker started exposure at the same time. The wavefront sensor measurement was followed by the adaptive optics control algorithm for wavefront sensing which calculated the commands and fed the deformable mirror. As soon as the deformable mirror started execution, the pupil tracker started the second measurement. At the end of the pupil tracker measure-

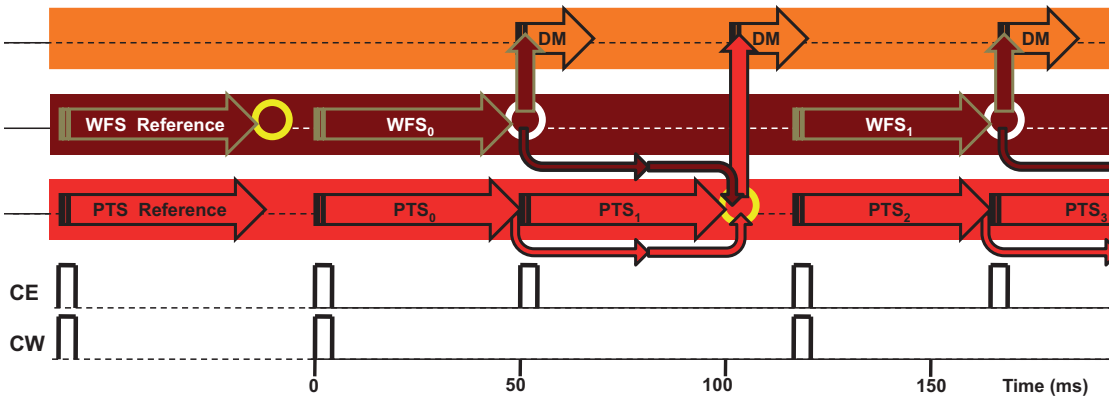

Figure 5.6: The AOPTL2 loop: the wavefront aberrations were corrected using the both adaptive optics control algorithms based on wavefront sensing and pupil tracking, shown as white and yellow rings respectively. The deformable mirror (DM) was called two times in one loop for the two command vectors coming from the two control algorithms successively.

ment the adaptive optics control for pupil tracking calculated the next command vector using the measured shift of the pupil, $\Delta\mathbf{v_x}$ and $\Delta\mathbf{v_y}$, and the command that was just applied to the deformable mirror in the loop. The deformable mirror was called a second time for the command calculated by the control algorithm based on pupil tracking and by this way the correction was compensated for the pupil shift that took place during the wavefront sensor measurement.

The wavefront sensor measurements required at least 50 ms because of the long exposure time needed due to the low power of the light source. During the time of both exposure and acquisition the pupil moves, and so does the wavefront. The pupil tracker recorded the initial and final positions of the pupil center and the control algorithm based on pupil tracking calculated the commands to be applied so that the deformable mirror could generate the shifted wavefront. Correction of this loop would probably be better with a faster pupil tracker but since unfortunately it took 50 ms for the pupil tracker to take a measurement in this configuration, this loop was not expected to yield a significant enhancement.

5.2 Experiments with the model eye

The model eye[2] with spherical aberration was positioned in front of the retinal imaging system on a stage and the stage was pushed and pulled mechanically by hand resulting in a quasi-periodic motion in micrometer scale. In all the plots the total RMS of the measured wavefronts and the coefficients of Zernike polynomials up to fifth order were estimated ***excluding tilt and defocus terms.*** The position of the measured pupil center is shown with respect to the position of the first data of the pupil tracking recording, on the x and y axis of the plane of the eye's pupil separately. First, The WFPT[3] loop was performed, see Figure 5.7. The mean RMS of the wavefront measurements after the still measurements (the measurements taken while the model eye was not moving - as seen towards the end of the Figure 5.7 - top) were excluded was 0.67 ± 0.02 μm. The pupil moved 32 ± 17 μm on average in between each pupil tracking measurement and the total pupil movement took place normally within 250×40 μm^2 ($2\sigma_x \times 2\sigma_y$). The effective number of lenslets used was 437 ± 1 lenslets on average over 1280 total lenslets. The wavefront of the model eye which had a 7 mm pupil, continuously fitted a pupil of 6 mm diameter which was the exact size of the pupil of the system, indicating wavefront measurement quality was good compared to measurements done with the data filling a smaller pupil due to misalignment.

The correlation of the RMS of the wavefront measurements with the pupil position on the x axis was 0.82, indicating a significant relationship between the decentration of the pupil and the aberration induced, see Figure 5.7. Indeed, the model eye had an important spherical aberration that was represented by the fourth order component of Zernike polynomials. Coma aberration which is induced in the optical systems by the misalignment of the pupil with the presence of a spherical aberration is represented here within the third order Zernike polynomials. It can be seen that because of the coma aberration that appeared when

[2]see Appendix C, Figures C.1 and C.2

[3]Loop which incorporates the wavefront sensor and the pupil tracker only (WFPT)

the spherical aberration was off-axis, the third order Zernikes were responsible for the majority of the aberration increases induced by the displacement of the model eye. The recording of the measurements can be viewed in the demo.exe application under the name 'Model Eye WFPT'.

Second, the AOPT[4] loop was performed where the deformable mirror was active and receiving the commands from the adaptive optics control algorithm based on wavefront sensor measurements, as shown in Figure 5.8. The mean RMS of the measured wavefronts after the still measurements (the measurements taken while the model eye was not moving) were excluded was 0.08 ± 0.04 μm, the model eye moved 30 ± 22 μm on average in between each pupil tracking measurements and spanned normally an area of 170×40 μm^2 ($2\sigma_x \times 2\sigma_y$). The wavefront measurements took place over a pupil which had 438 ± 1 active lenslets on average.

The correlation of the wavefront RMS with the pupil position was low but was 0.69 with the pupil displacement at each loop on x axis, see Figure 5.8. Because the aberrations were continuously corrected by the deformable mirror, the relative position of the pupil had no effect on the aberrations, instead this time the pupil shift at each loop was the factor that introduced the aberrations to the corrected wavefront. It was again the coma aberration that was introduced by the shift of the model eye. The recording of the measurements can be viewed in the demo.exe application under the name 'Model Eye AOPT'.

[4]Loop which incorporates the wavefront sensor, the deformable mirror, the pupil tracker and the control algorithm based on wavefront sensing (AOPT)

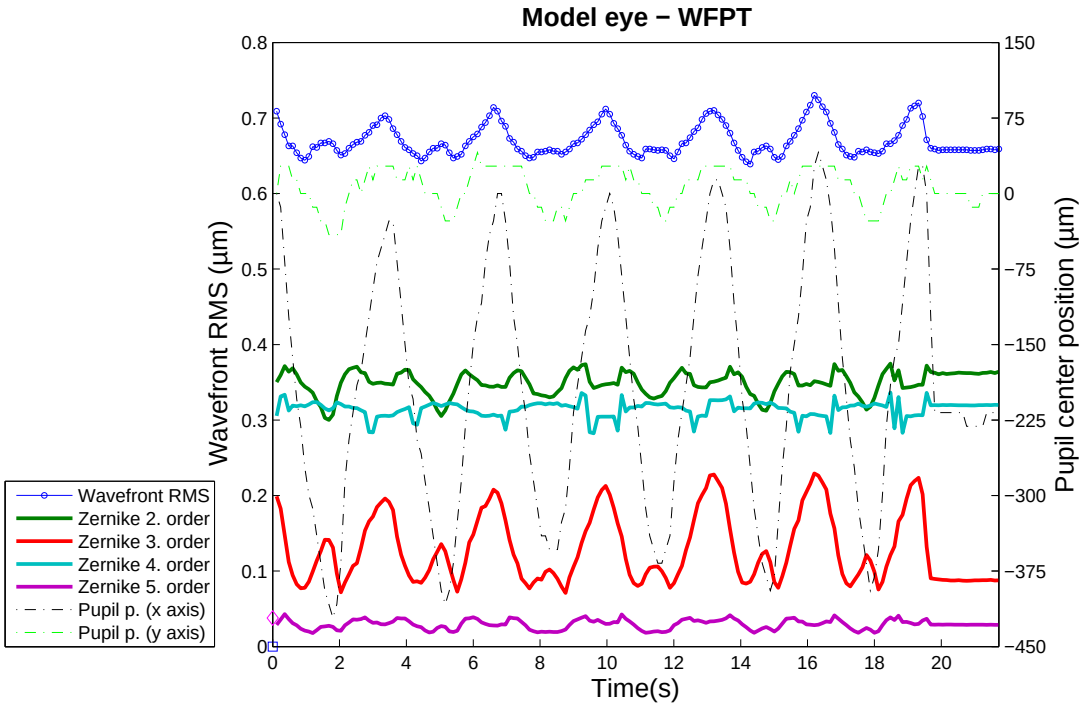

(top) Loop which incorporates the wavefront sensor and the pupil tracker only (WFPT). The total RMS of the wavefront measurements, coefficients of Zernike polynomials up to the fifth order and pupil position with respect to initial position of the pupil on x and y axis separately at each loop (tilt or defocus terms are not included in the total RMS or in the Zernike coefficients).

WFPT - Mean (μm)

RMS	PS	NA	PD	NL
0.67 ± 0.02	32 ± 17	250×40 μm^2	7072±0	437 ± 1 $(lenslets)$

(middle) Mean wavefront RMS (RMS), mean pupil shift in between two pupil tracking measurements (PS), dimensions of the area in which the eye normally was (NA) ($2\sigma_x \times 2\sigma_y$), mean pupil diameter (PD), and mean number of lenslets that were used during the measurement (NL).

WFPT - Correlation of the WF RMS with

PP (x axis)	PP (y axis)	PP (ρ)	PS (x axis)	PS (y axis)	PS (ρ)
0.82	-0.62	-0.79	-0.12	-0.18	-0.14

(bottom) Correlation of the measured wavefront RMS with the measured pupil position (PP) and with the pupil shift in between each pupil tracking measurement (PS) on x axis and y axis. ρ stands for the radial position.

Figure 5.7: The model eye: the WFPT loop.

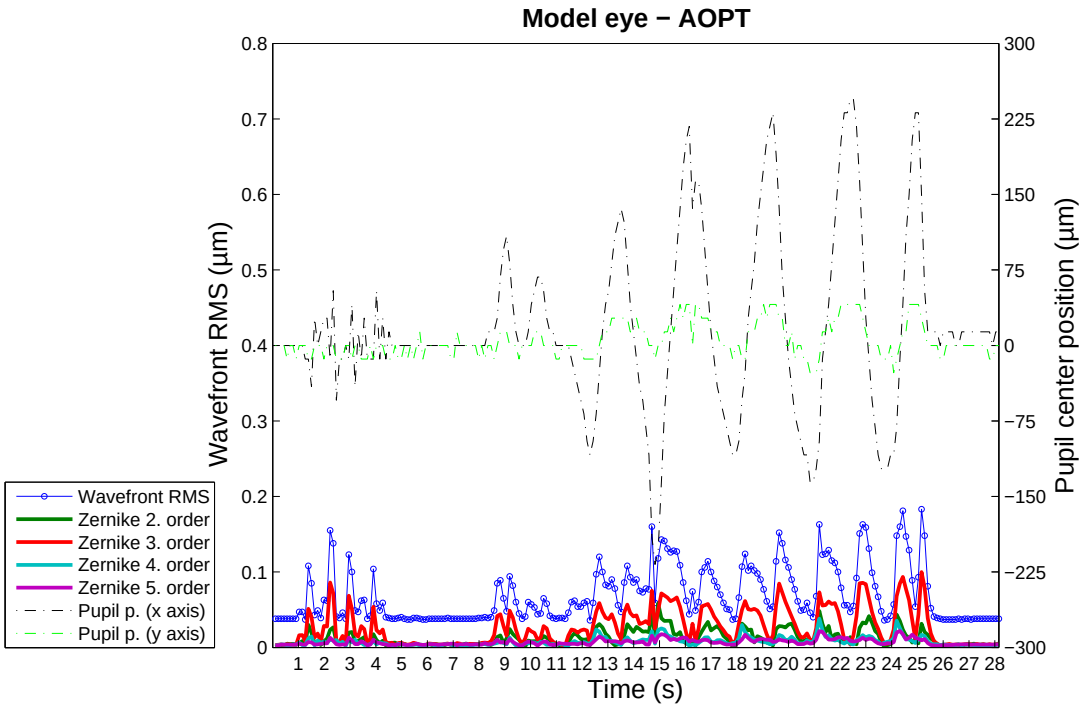

(top) Loop which incorporates the wavefront sensor, the deformable mirror, the pupil tracker and the control algorithm based on wavefront sensing (AOPT). The total RMS of the wavefront measurements, coefficients of Zernike polynomials up to the fifth order and pupil position with respect to initial position of the pupil on x and y axis separately at each loop (tilt or defocus terms are not included in the total RMS or in the Zernike coefficients).

AOPT - Mean (μm)

RMS	PS	NA	PD	NL
0.08 ± 0.04	30 ± 22	170×40 μm^2	7072±0	438 ± 1 (*lenslets*)

(middle) Mean wavefront RMS (RMS), mean pupil shift in between two pupil tracking measurements (PS), dimensions of the area in which the eye normally was (NA) ($2\sigma_x \times 2\sigma_y$), mean pupil diameter (PD), and mean number of lenslets that were used during the measurement (NL).

AOPT - Correlation of the WF RMS with

PP (x axis)	PP (y axis)	PP (ρ)	PS (x axis)	PS (y axis)	PS (ρ)
0.14	-0.37	0.28	0.69	0.17	0.12

(bottom) Correlation of the measured wavefront RMS with the measured pupil position (PP) and with the pupil shift in between each pupil tracking measurement (PS) on x axis and y axis. ρ stands for the radial position.

Figure 5.8: The model eye: the AOPT loop.

Third, the WFPTa[5] loop was performed, see Figure 5.9. The mean wavefront RMS after the still measurements were excluded was 0.14 ± 0.08 μm; the pupil displaced 23 ± 16 μm in average at each loop and the total movement took place normally in an area of 180×40 μm^2 ($2\sigma_x \times 2\sigma_y$).

Again the dominant aberration that caused the increase in wavefront RMS was coma represented by Zernike third order in Figure 5.9. The RMS of the wavefront aberrations were lowest whenever the model eye returned back to its initial position where the static correction shape of the deformable mirror was valid. The wavefront RMS was highly related to the radial pupil position with a correlation coefficient of 0.92. The correlation of the pupil position with the wavefront RMS suggested that the change of aberrations could be simulated.

First, the derivatives of the s_x^{ref} and s_y^{ref}, the slopes data of the $\mathbf{WF_{Ref}}$[6] of the eye were calculated according to the control algorithm based on pupil tracking as described in the previous chapter. The $\Delta_x s_x$ and $\Delta_y s_x$, the derivatives of s_x^{ref} on x and y axis,

$$\begin{aligned} \Delta_x s_{x_{ij}} &= s^{ref}_{x_{i,j+1}} - s^{ref}_{x_{ij}} \quad \text{for} \;\; i = 1, 2, \ldots, 32 \\ \Delta_y s_{x_{ij}} &= s^{ref}_{x_{i+1,j}} - s^{ref}_{x_{ij}} \qquad\quad j = 1, 2, \ldots, 40. \end{aligned} \tag{5.1}$$

And the $\Delta_x s_y$ and $\Delta_y s_y$, the derivatives of s_y^{ref} on x and y axis,

$$\begin{aligned} \Delta_x s_{y_{ij}} &= s^{ref}_{y_{i,j+1}} - s^{ref}_{y_{ij}} \quad \text{for} \;\; i = 1, 2, \ldots, 32 \\ \Delta_y s_{y_{ij}} &= s^{ref}_{y_{i+1,j}} - s^{ref}_{y_{ij}} \qquad\quad j = 1, 2, \ldots, 40. \end{aligned} \tag{5.2}$$

Second, the displacements of the model eye on the pupil plane $(\Delta x, \Delta y)$ were converted to the displacements of the wavefronts on the wavefront sensor plane in

[5]Loop which incorporates the wavefront sensor, the pupil tracker and the deformable mirror that corrects the aberrations statically (WFPTa)

[6]The reference measurement of the wavefront aberrations of the eye whose derivative is used in the control algorithm based on pupil tracking (WF_{Ref})

terms of lenslets, (a, b) by,

$$\begin{bmatrix} a \\ b \end{bmatrix} = \frac{M}{l} \begin{bmatrix} cos\theta \ sin\theta \\ -sin\theta \ cos\theta \end{bmatrix} \begin{bmatrix} \Delta x \\ \Delta y \end{bmatrix} \tag{5.3}$$

where M and θ are the magnification and the rotation coefficients of the optical system respectively and l is the distance between the two lenslet centers.

Next, to simulate the aberrations of the displaced model eye, the derivatives on x and y axis were multiplied by a and b respectively and added to the slopes data of the first wavefront measurement of the experiment $\mathbf{WF_0}$, namely $s_x^{mes^0}$ and $s_y^{mes^0}$,

$$s_x^{sim^i} = s_x^{mes^0} + (a_i \times \Delta_x s_x + b_i \times \Delta_y s_x) \tag{5.4}$$

$$s_y^{sim^i} = s_y^{mes^0} + (a_i \times \Delta_x s_y + b_i \times \Delta_y s_y). \tag{5.5}$$

where (a_i, b_i) represents the i^{th} measured displacement of the eye, $s_x^{sim^i}$ and $s_y^{sim^i}$ are the slopes data of the i^{th} simulated wavefront $\mathbf{WF^i_{Sim}}$. Using $s_x^{sim^i}$ and $s_y^{sim^i}$, the i^{th} simulated wavefront, $\mathbf{WF^i_{Sim}}$ was reconstructed by zonal reconstruction. The RMS values of the measured wavefront, $\mathbf{WF^i_{Mes}}$, the $\mathbf{WF^i_{Sim}}$ and the residual error wavefront $\mathbf{WF^i_{Err}} = \mathbf{WF^i_{Mes}} - \mathbf{WF^i_{Sim}}$ were shown in Figure 5.10.

Mean RMS of the $\mathbf{WF_{Sim}}$ had lower RMS than the measured wavefronts. The error of the simulation, the $\mathbf{WF_{Err}}$ had 0.07 ± 0.03 μm mean RMS after the still ones were excluded.

During the experiment the model eye was pushed and pulled by hand away from its stable initial position. When the model eye was pushed or pulled away from its initial position this was immediately followed by a comeback because of the robustness of the set up. This restoration (coming back) to the initial position took shorter time than the disturbance (going away) as it can be clearly seen by comparing the number of data on the ascending and descending sides of the peaks in Figure 5.9 - top.

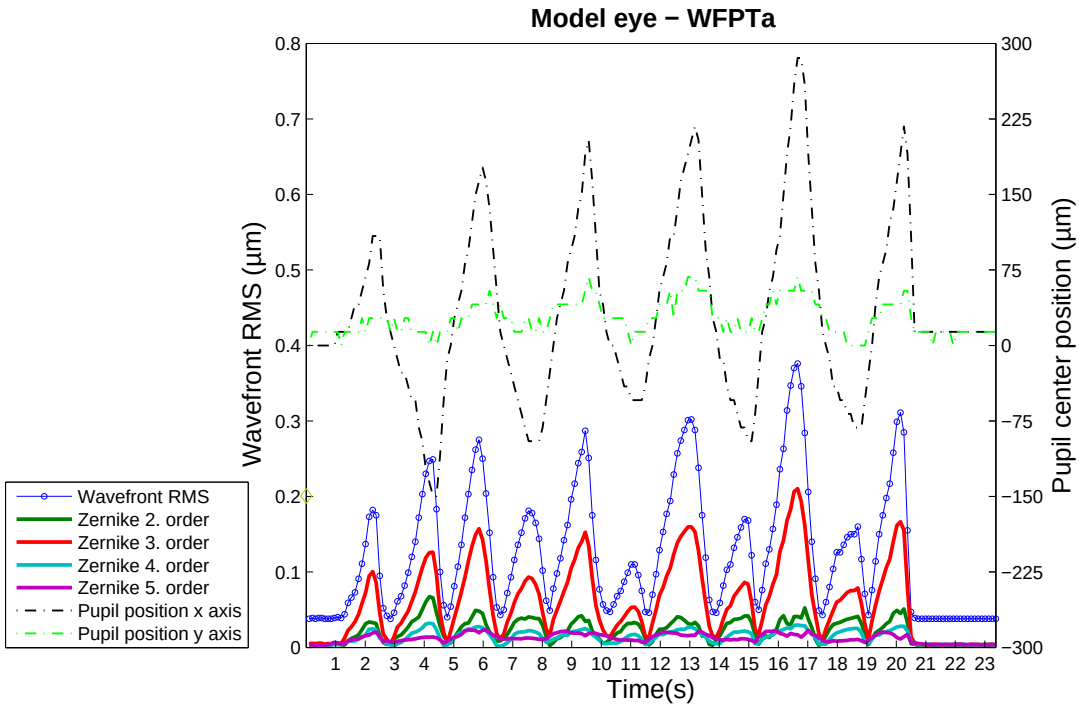

(top) Loop which incorporates the wavefront sensor, the pupil tracker and the deformable mirror that corrects the aberrations statically (WFPTa). The total RMS of the wavefront measurements, coefficients of Zernike polynomials up to the fifth order and pupil position with respect to initial position of the pupil on x and y axis separately at each loop (tilt or defocus terms are not included in the total RMS or in the Zernike coefficients)

WFPTa - Mean (μm)

RMS	PS	NA	PD	NL
0.14 ± 0.08	23 ± 16	180×40 μm^2	7072±0	438 ± 1 (*lenslets*)

(middle) Mean wavefront RMS (RMS), mean pupil shift in between two pupil tracking measurements (PS), dimensions of the area in which the eye normally was (NA) ($2\sigma_x \times 2\sigma_y$), mean pupil diameter (PD), and mean number of lenslets that were used during the measurement (NL).

WFPTa - Correlation of the WF RMS with

PP (x axis)	PP (y axis)	PP (ρ)	PS (x axis)	PS (y axis)	PS (ρ)
0.58	-0.62	0.92	0.16	0.02	0.17

(bottom) Correlation of the measured wavefront RMS with the measured pupil position (PP) and with the pupil shift in between each pupil tracking measurement (PS) on x axis and y axis. ρ stands for the radial position.

Figure 5.9: The model eye: the WFPTa loop.

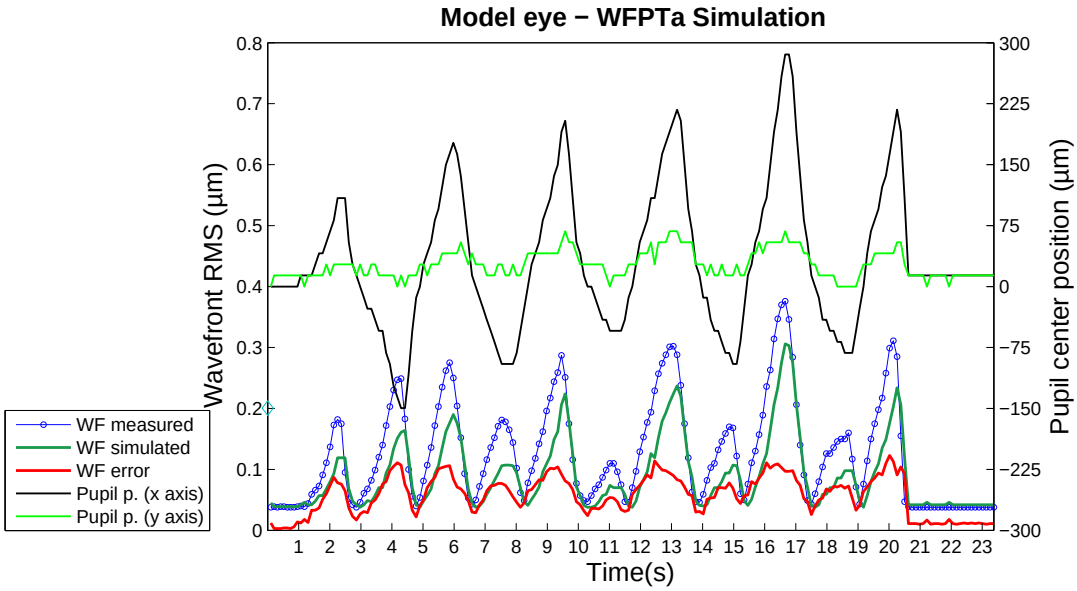

(top) RMS of the simulations of the measured wavefront aberrations changing due to eye movements (green solid line) and the residual error of the simulations (red solid line).

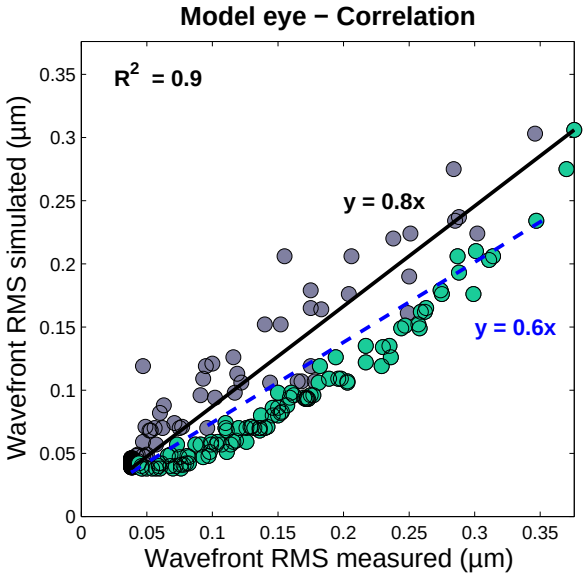

(bottom) Correlation of the RMS of the measured and the simulated wavefronts of the moving eye. The data was categorized into two: the green colored data indicates that the model eye was moving away from the initial position and the purple colored data was taken while the eye was returning back to its initial position.

Figure 5.10: The model eye: simulation of the WFPTa loop measurements.

In Figure 5.10 - bottom, the correlation plot of the measured and the simulated data was not linear; the distribution of the data looked like an ellipse (indicating hysteresis due to a time lag). In the correlation plot, the data was categorized into two according to their trend: the ascending and the descending aberration RMS represented with different colors. Fitting a straight line to this data would be erroneous and would not reveal the real process because the numbers of data of the two types were not equal and an ideal straight line would be at equal distance to the both them.

A time lag can explain this plot: the pupil tracker was always measuring the position of the pupil with a slight error *i.e.*, it was following behind. Because of this when the eye was going away the algorithm was underestimating the shift and when it was coming back it was overestimating. The measurements live can be viewed from the demo.exe with the name 'Model eye WFPTa '.

Next, the AOPTL1[7] loop was run, see Figure 5.11. The wavefront RMS was both related to the radial pupil position and the pupil displacement at each loop, correlation coefficients being 0.78 and 0.32 respectively. This time the major contribution to the aberration changes came from second order Zernike coefficients which represented the astigmatism. This is showing that the control algorithm could compensate for the aberrations which had a linear relationship with the field angle but could not do well for astigmatism for example which had a quadratic relationship with the field angle. The recording of the measurements can be viewed in the demo.exe application under the name 'Model Eye AOPTL1 '.

[7]Loop which incorporates the wavefront sensor, the deformable mirror, the pupil tracker and the control algorithm based on pupil tracking (AOPTL1)

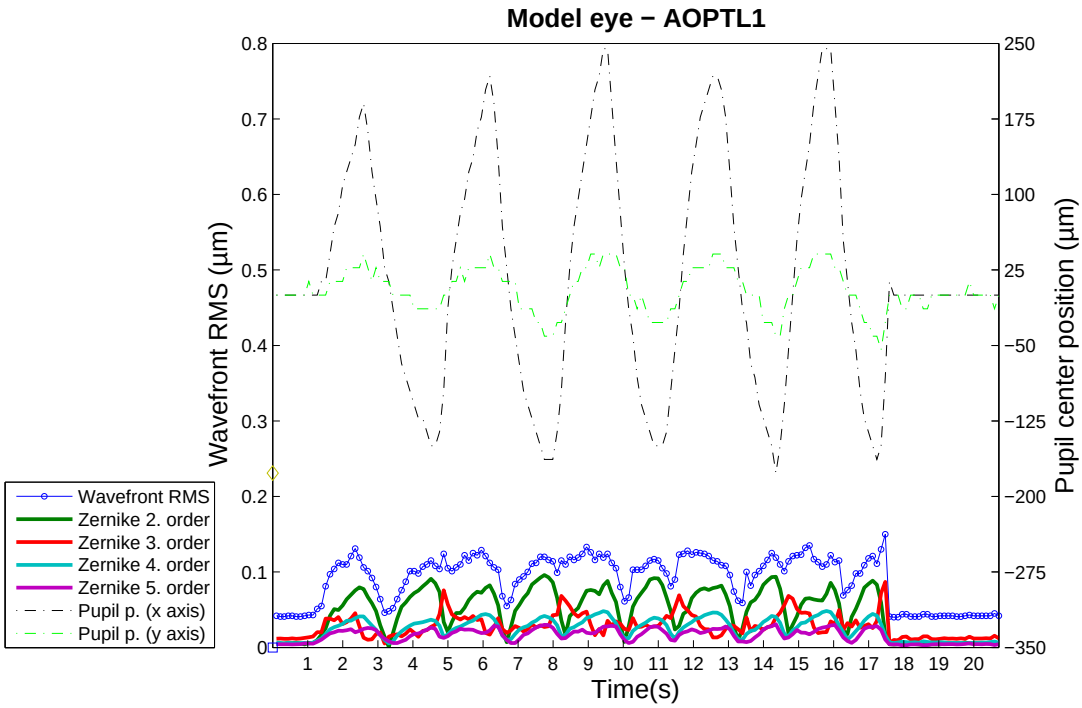

(top)Loop which incorporates the wavefront sensor, the deformable mirror, the pupil tracker and the control algorithm based on pupil tracking (AOPTL1)(tilt or defocus terms are not included in the total RMS or in the Zernike coefficients).

AOPTL1 - Mean (μm)

RMS	PS	NA	PD	NL
0.1 ± 0.02	30 ± 19	230×40 μm^2	7072±0	438 ± 1 $(lenslets)$

(middle) Mean wavefront RMS (RMS), mean pupil shift in between two pupil tracking measurements (PS), dimensions of the area in which the eye normally was (NA) ($2\sigma_x \times 2\sigma_y$), mean pupil diameter (PD), and mean number of lenslets that were used during the measurement (NL).

AOPTL1 - Correlation of the WF RMS with

PP (x axis)	PP (y axis)	PP (ρ)	PS (x axis)	PS (y axis)	PS (ρ)
0.16	-0.12	0.78	0.32	0.09	0.29

(bottom) Correlation of the measured wavefront RMS with the measured pupil position (PP) and with the pupil shift in between each pupil tracking measurement (PS) on x axis and y axis. ρ stands for the radial position.

Figure 5.11: The model eye: the AOPTL1 loop

Finally, the AOPTL2[8] loop was tested with the moving model eye, see Figure 5.12. Similar to the AOPT loop, the correlation of the wavefront RMS with the radial pupil shift at each loop was high, 0.71. Again coma was responsible for the most of the aberration changes induced by the pupil displacement. The recording of the experiment can be viewed in the demo.exe application under the name 'Model Eye AOPTL2 '.

Figure 5.13 displays all the experiments together. The adaptive optics algorithm based on pupil tracking was able to correct for the aberrations of the eye by sending the appropriate commands to the deformable mirror in two cases, first, replacing the wavefront sensor (AOPTL1[9]) and second, working in collaboration with the wavefront sensor (AOPTL2). The control algorithm based on pupil tracking was able to simulate the changes of aberrations due to eye movements in the open loop WFPTa. The error of simulations resembled the residual error RMS of the AOPTL1 loop *i.e.*, the application of the simulations real time.

The wavefront RMS for the AOPT[10] and AOPTL2 loop measurements were 0.08 ± 0.04 and 0.07 ± 0.02 μm respectively. It has to be taken into account that the pupil movements were different for the two loops so it cannot be said that AOPTL2 was better than AOPT. However the AOPTL2 might have had a smaller standard deviation with the help of the pupil tracking, for the plots of pupil tracking measurements on x-y plane see Figure 5.14 .

The mean RMS of the residual error of the simulation of the WFPTa[11] loop and the AOPTL1 loop were 0.07 ± 0.03 μm and 0.1 ± 0.02 μm respectively. The WFPTa loop demonstrated the effect of eye movements to a static correction. Simulations done using the control algorithm based on pupil tracking estimated the induced aberrations well despite their large magnitude.

[8]Loop which incorporates the wavefront sensor, the deformable mirror, the pupil tracker and the control algorithms based on wavefront sensing and pupil tracking (AOPTL2)

[9]Loop which incorporates the wavefront sensor, the deformable mirror, the pupil tracker and the control algorithm based on pupil tracking (AOPTL1)

[10]Loop which incorporates the wavefront sensor, the deformable mirror, the pupil tracker and the control algorithm based on wavefront sensing (AOPT)

[11]Loop which incorporates the wavefront sensor, the pupil tracker and the deformable mirror that corrects the aberrations statically (WFPTa)

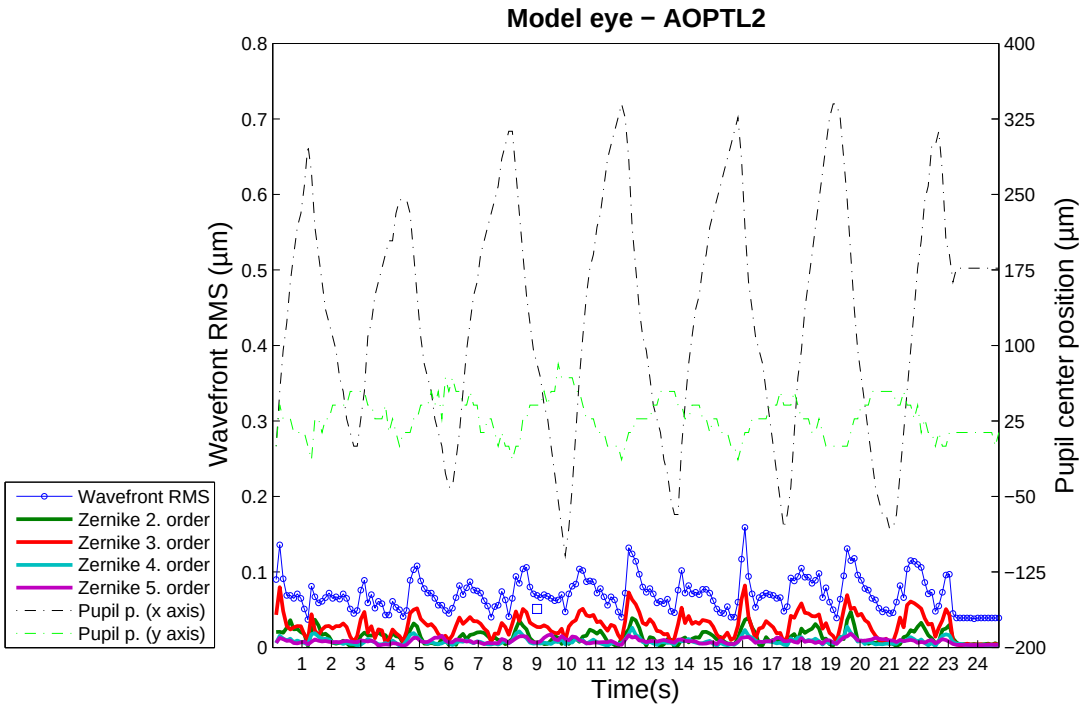

(top) Loop which incorporates the wavefront sensor, the deformable mirror, the pupil tracker and the control algorithms based on wavefront sensing and pupil tracking (AOPTL2)(tilt or defocus terms are not included in the total RMS or in the Zernike coefficients).

AOPTL2 - Mean (μm)

RMS	PS	NA	PD	NL
0.07 ± 0.02	26 ± 15	230×40 μm^2	7072±0	438 ± 1 $(lenslets)$

(middle) Mean wavefront RMS (RMS), mean pupil shift in between two pupil tracking measurements (PS), dimensions of the area in which the eye normally was (NA) ($2\sigma_x \times 2\sigma_y$), mean pupil diameter (PD), and mean number of lenslets that were used during the measurement (NL).

AOPTL2 - Correlation of the WF RMS with

PP (x axis)	PP (y axis)	PP (ρ)	PS (x axis)	PS (y axis)	PS (ρ)
0	-0.03	-0.1	0.73	0.15	0.71

(bottom) Correlation of the measured wavefront RMS with the measured pupil position (PP) and with the pupil shift in between each pupil tracking measurement (PS) on x axis and y axis. ρ stands for the radial position.

Figure 5.12: The model eye: the AOPTL2 loop.

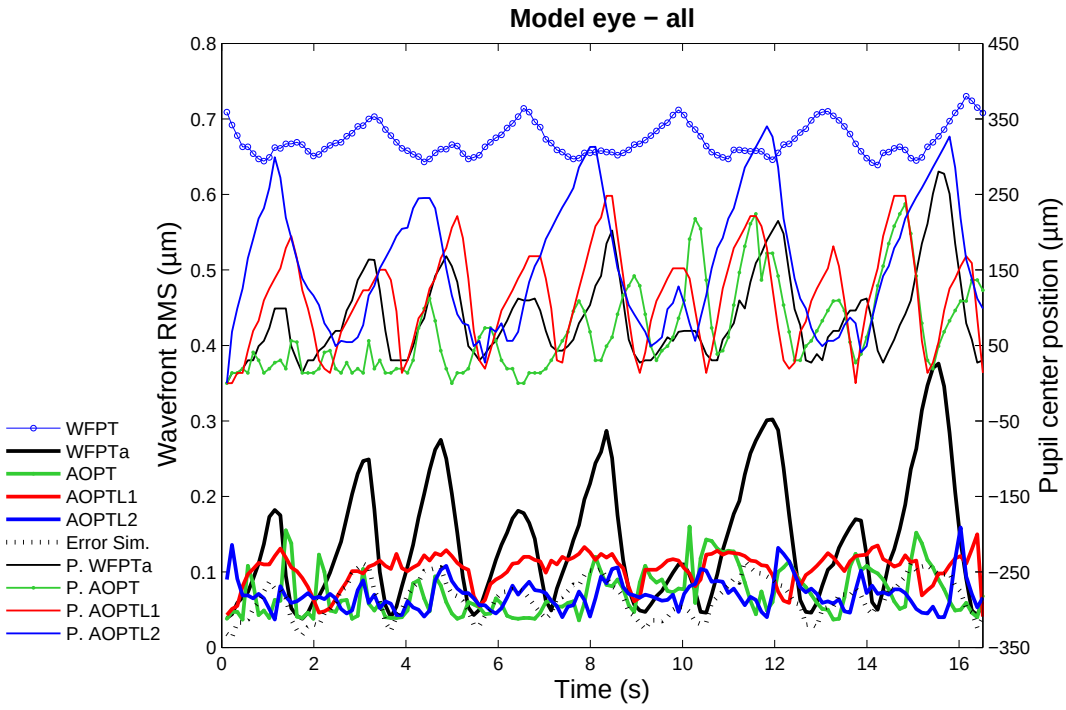

(top) Wavefront RMS of the WFPT, AOPT, WFPTa, AOPTL1 and AOPTL2 experiments along with the residual error of the WFPTa simulations and their respective pupil positions (P) shown in the same color.

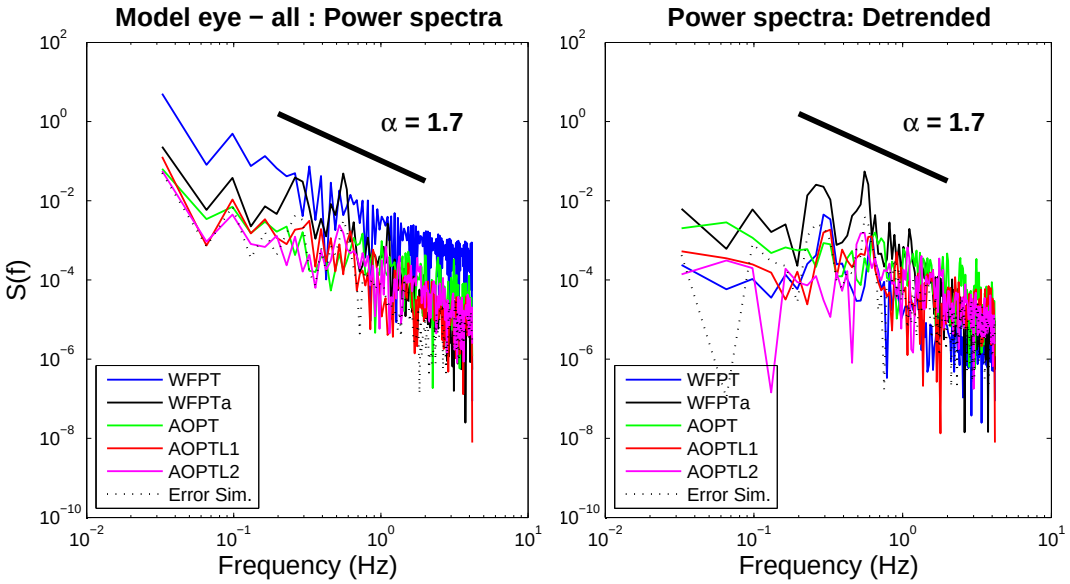

(bottom) Power spectra of the RMS of all the measurements and the residual error wavefront of the simulations after still measurements were excluded (left). The detrended spectra (done after the mean of the each data set were subtracted) shows two distinct peaks at 0.3 and 0.6 Hz.

Figure 5.13: The model eye: summary of the experiments.

Figure 5.13 - bottom displays the power spectra of all the measurements. The maximum frequency that could be shown in this plot was $\frac{8.4}{2} = 4.2$ Hz. Minimum frequency in the data spectrum is $\frac{1}{16.5} = 0.06$ Hz, 16.5 s being the total time of the recording. The spectra covers 0.03-4.2 Hz because of the fact that Fast Fourier Transform requires the number of data to be equal to 2^n, here it was 2^8.

In the spectra on the left, the WFPT and the AOPTL2 measurements had the largest and the smallest magnitudes respectively, which did not represent the magnitude of the fluctuation. The magnitudes and the order of the spectra of the data is affected from the offset of the data so that detrending is a better approach to evaluate the different spectra in terms of fluctuations. The spectra on the right shows the detrended spectra, *i.e.*, the calculations done after the mean values were subtracted from each data. There, the WFPTa and AOPTL2 loops had the largest and smallest amounts of fluctuations respectively. Two distinct peaks at ~ 0.3 and ~ 0.6 Hz can be seen in common in the of WFPTa, WFPT, AOPTL1 loops and the error of simulation.

The logarithmic display of the spectra showed a $1/f^{\alpha}$ like trend indicating a power law relationship between the frequency and the power where $\alpha \cong 1.7$. In the scientific literature any noise (signal) with a power spectral density of the form,

$$S(f) \propto 1/f^{\alpha} \tag{5.6}$$

where $0<\alpha<2$ with α usually close to 1 are loosely called 1/f noise. This type of signal is an intermediate between the white noise with power spectrum of $1/f^0$ and the random walk noise with spectrum of $1/f^2$. The characteristic of this type of noise is that integral of its power spectrum starting from a finite frequency value towards the infinity is diverging as well as integral of its spectra starting from a finite value towards zero [131]. This signifies that its mean over long periods or its instantaneous value are not well defined; a statement of the fact that the data was non-stationary[12]. The spectra are generally noisy and the trends are not well

[12]opposite to stationary *i.e.* a stochastic process whose mean or variance do not change over

defined due to the fact that the power spectra estimation requires large number of stationary data and lack of this is a source of error. It has to be remembered that this quasi-periodic movement was made by hand and not by a machine rendering it complex and non-stationary.

Finally Figure 5.14 shows the recorded pupil positions during each experiment on the x-y plane.

time or position

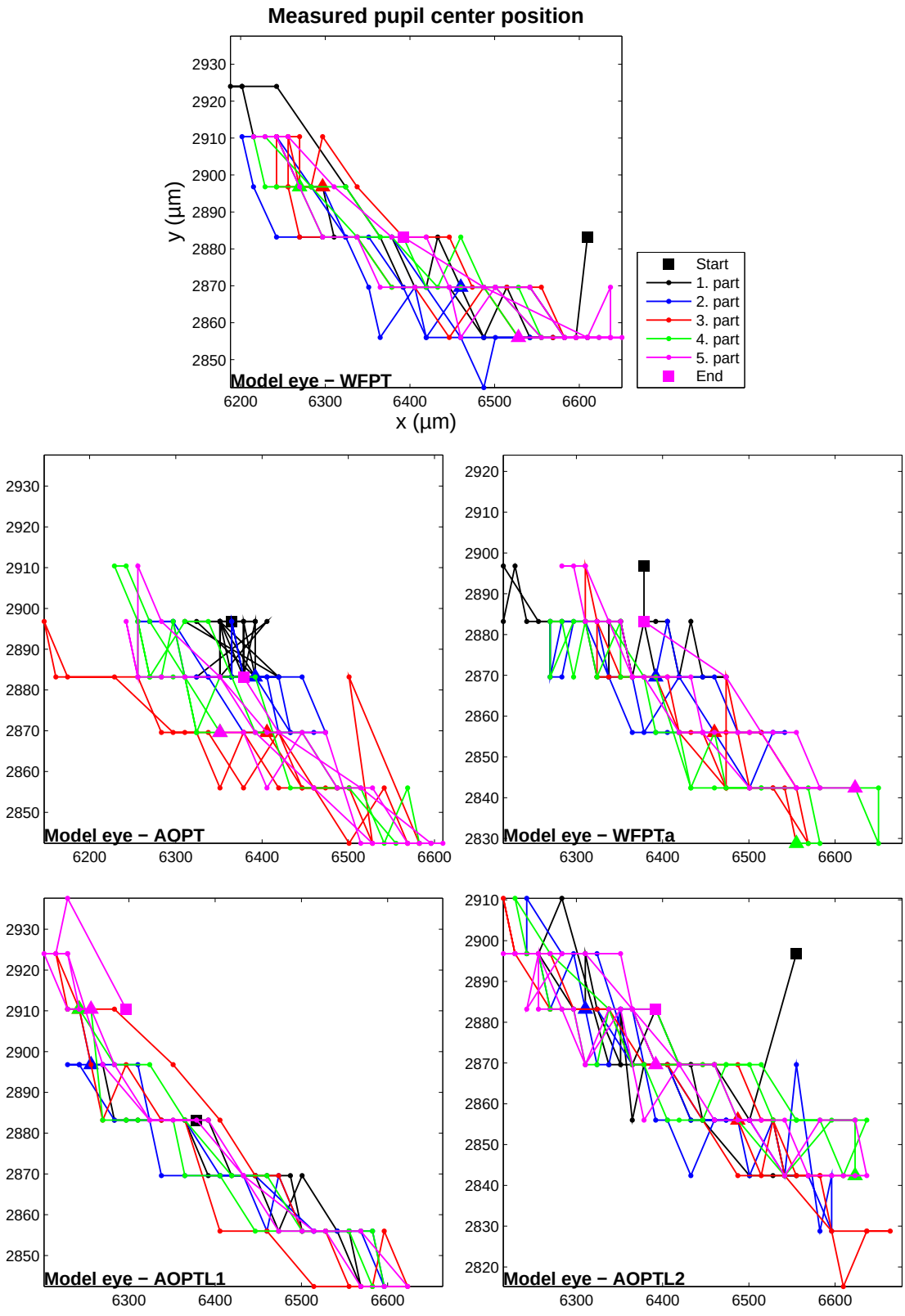

Figure 5.14: Pupil positions recorded during each experiment. All the plots have x and y axes scaled to 462×95 μm. For visual clarity the data was divided into five parts, colored differently and beginning and the end of the data were indicated by square markers.

5.2.1 Static measurements with the model eye

It was important to know the noise levels for all types of loops. For this purpose the same experimental procedure was performed this time for a static model eye. Figure 5.15 displays the mean values and standard deviations of wavefront and pupil tracking measurements.

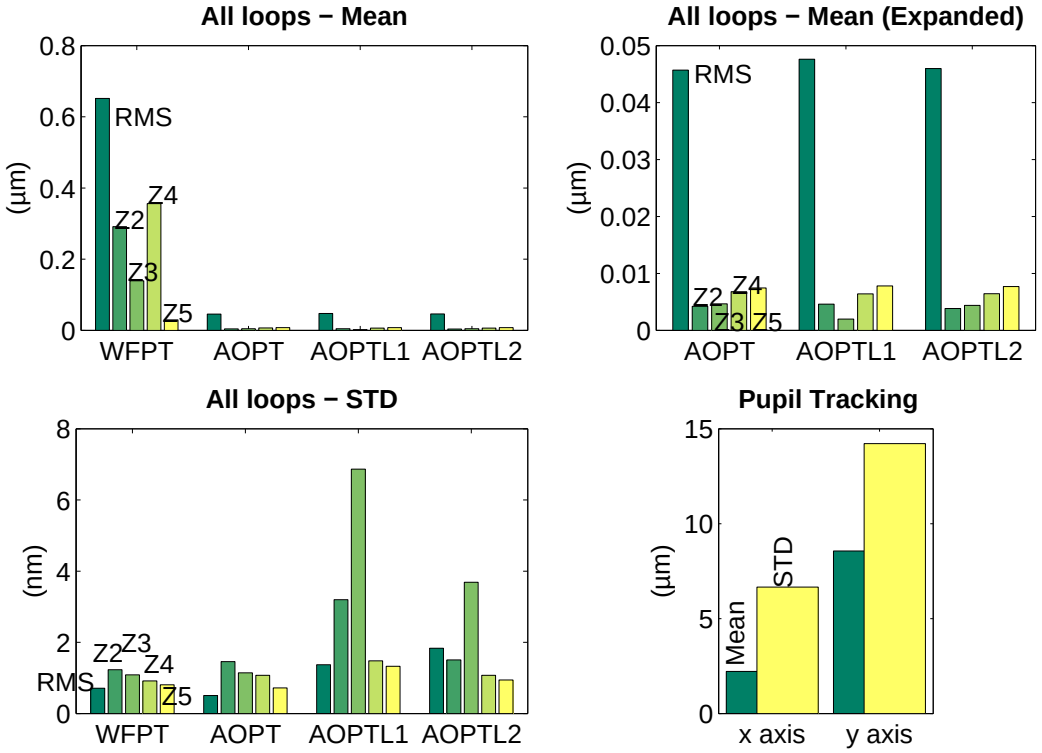

Figure 5.15: Summary of all measurements done by all types of loops for a still model eye: mean of total RMS and the Zernike coefficients of second to fifth order of the measured wavefronts (top left); closer look to see AOPT, AOPTL1 and AOPTL2 measurements (top right); standard deviation of the total RMS and the Zernike coefficients of the measurements (bottom left), and the mean and the standard deviation of the pupil displacement measured in between each pupil tracking measurement during each of the experiments above (bottom right).

The mean RMS of the WFPT[13] loop measurements shows the typical aberrations of the model eye, where astigmatism and coma aberrations were highly dependent on the alignment of the model eye with respect to the system. The

[13]Loop which incorporates the wavefront sensor and the pupil tracker only (WFPT)

mean RMS of the AOPT[14], AOPTL1[15] and AOPTL2[16] corrections had similar aberration profiles but the standard deviations of AOPTL1 and AOPTL2 measurements had a slightly different profile. The standard deviations of the third order Zernikes which represents coma aberrations of the AOPTL1 and AOPTL2 were higher than the AOPT loop, Figure 5.15 (bottom left). This can be understood by looking into the noise levels of the pupil tracking system, Figure 5.15 (bottom right).

One pixel on the pupil tracking camera corresponds to 13.6 μm on the object plane. The pupil tracking algorithm had the resolution of one pixel; the response of the adaptive optics control algorithm based on pupil tracking to an error of one pixel in the pupil tracking measurement was to calculate a new command to be applied for a 13.6 μm shifted wavefront as a result of which the coma aberration appeared. This one pixel error of pupil center measurements must have been equally distributed because the mean of the RMS values for AOPTL1 and AOPTL2 loops were similar to the AOPT loop and demonstrated no extra coma aberration induced due to the error of pupil tracking measurements.

The mean and the standard deviation of the pupil center measurements with respect to the initial pupil position on y axis were higher than the values on x axis. This might be due to the fact the y axis coordinates were calculated using the parabolic fit which had a limited resolution while the x coordinates were calculated directly from the measurement data.

[14]Loop which incorporates the wavefront sensor, the deformable mirror, the pupil tracker and the control algorithm based on wavefront sensing (AOPT)

[15]Loop which incorporates the wavefront sensor, the deformable mirror, the pupil tracker and the control algorithm based on pupil tracking (AOPTL1)

[16]Loop which incorporates the wavefront sensor, the deformable mirror, the pupil tracker and the control algorithms based on wavefront sensing and pupil tracking (AOPTL2)

5.3 Experiments with human eyes

The five different loops were tested with the same procedures for three healthy human subjects. They were positioned in front of the adaptive optics retinal camera where their heads were stabilized with a standard ophthalmic chinrest. They were asked to fixate their eyes to the dim red point image of the SLD light source of the wavefront sensor. They were not applied pupil dilating medicaments or any other solutions. All of the aberration corrections was carried out by the deformable mirror; correcting lenses or the Badal were not used. The recordings of the measurements can be viewed in the demo.exe application under the relevant name.

In all the plots the total RMS of the measured wavefronts and the coefficients of Zernike polynomials up to fifth order were estimated ***excluding tilt and defocus terms.*** The position of the measured pupil center was shown with respect to the position of the first data of the pupil tracking recording, on the x and y axis of the plane of the eye's pupil separately.

The following three sections present the results for the three subjects, and they are then discussed and compared in Section 5.4

5.3.1 Experimental results for Subject 1

First, the WFPT[17] loop was performed with the first subject's eye, Figure 5.16. The mean of the RMS of the wavefront measurements was 2.16 ± 0.11 μm, the wavefront spanned over 405 ± 9 lenslets on the wavefront sensor indicating a smaller and less stable pupil than the pupil of the model eye. The RMS of the aberrations was related to the radial pupil position with 0.65 and was not related to the pupil shift in between each pupil tracking measurements. The most dominant component of the aberrations was the second order Zernike, the astigmatism then the third order, coma.

[17]Loop which incorporates the wavefront sensor and the pupil tracker only (WFPT)

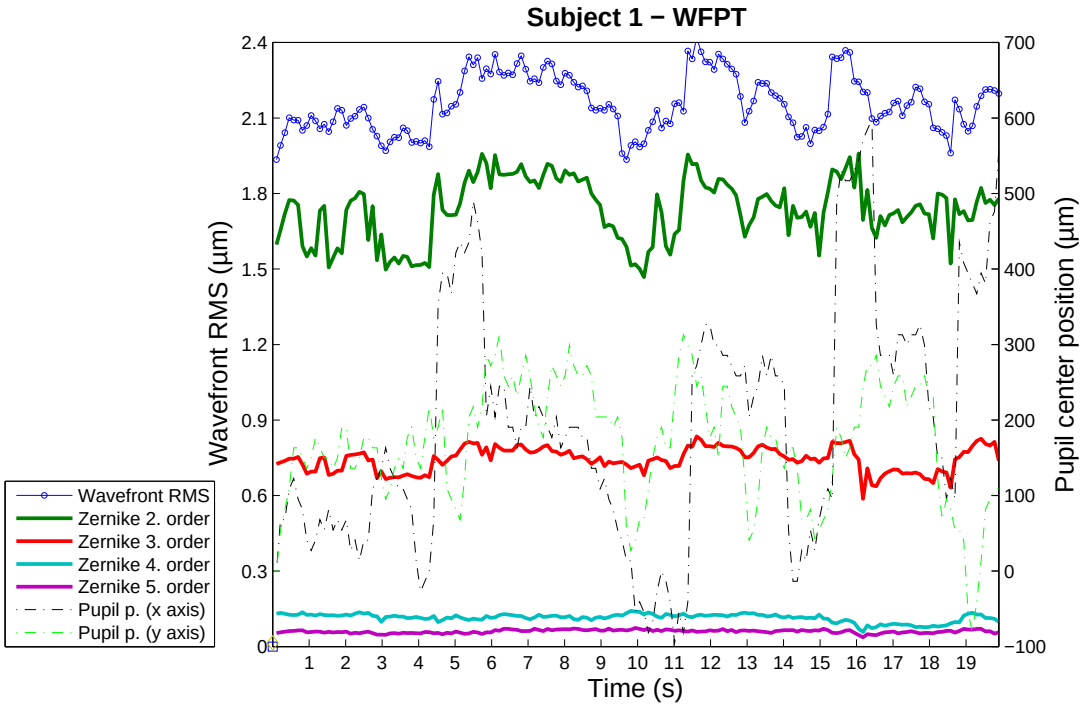

(top) Loop which incorporates the wavefront sensor and the pupil tracker only (WFPT)(tilt or defocus terms are not included in the total RMS or in the Zernike coefficients).

WFPT - Mean (μm)				
RMS	PS	NA	PD	NL
2.16 ± 0.11	51 ± 57	330×160 μm^2	6800 ± 300	405 ± 9 $(lenslets)$

(middle) Mean wavefront RMS (RMS), mean pupil shift in between two pupil tracking measurements (PS), dimensions of the area in which the eye normally was (NA) ($2\sigma_x \times 2\sigma_y$), mean pupil diameter (PD), and mean number of lenslets that were used during the measurement (NL).

WFPT - Correlation of the WF RMS with					
PP (x axis)	PP (y axis)	PP (ρ)	PS (x axis)	PS (y axis)	PS (ρ)
-0.54	-0.52	0.65	0.1	0.03	0.1

(bottom) Correlation of the measured wavefront RMS with the measured pupil position (PP) and with the pupil shift in between each pupil tracking measurement (PS) on x axis and y axis. ρ stands for the radial position.

Figure 5.16: Subject 1: the WFPT loop.

Second, the AOPT[18] loop was performed, see Figure 5.17. Similar to the model eye, the wavefront RMS was correlated with the pupil shift at each loop and was not correlated with the pupil position. Zernike second orders showed several spikes in correlation with the abrupt changes in pupil position while the coefficient of the other orders remained low.

Next, the WFPTa[19] loop was performed, Figure 5.18. The wavefront RMS was correlated with the position of the pupil on the y axis with a coefficient of 0.85. The major contributions to the change of aberrations came from Zernike second order astigmatism while the higher order aberrations were less variant.

Figure 5.19 - top shows the simulations done (as described in the previous section) to estimate the changes of aberrations due to eye movements in the WFPTa loop using the methodology of the control algorithm based on pupil tracking. The mean RMS of the simulations was 0.35 ± 0.10 μm; slightly lower than 0.39 ± 0.09 mean RMS of the measured wavefront. The RMS of the residual error of the simulations were also shown which had an 0.21 ± 0.07 μm average value. The RMS values of the simulated and the measured wavefronts were correlated by a coefficient of 0.9, see Figure 5.19 - bottom.

[18]Loop which incorporates the wavefront sensor, the deformable mirror, the pupil tracker and the control algorithm based on wavefront sensing (AOPT)

[19]Loop which incorporates the wavefront sensor, the pupil tracker and the deformable mirror that corrects the aberrations statically (WFPTa)

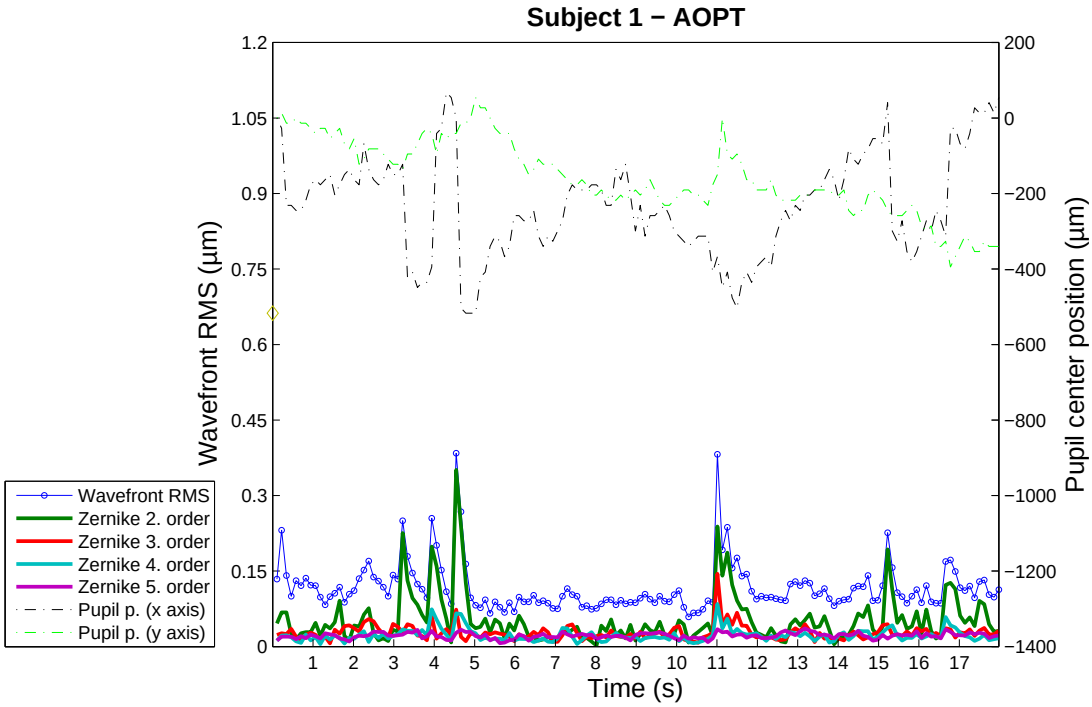

(top) Loop which incorporates the wavefront sensor, the deformable mirror, the pupil tracker and the control algorithm based on wavefront sensing (AOPT)(tilt or defocus terms are not included in the total RMS or in the Zernike coefficients).

AOPT - Mean (μm)

RMS	PS	NA	PD	NL
0.12 ± 0.05	51 ± 67	280×200 μm^2	6800 ± 90	417 ± 5 $(lenslets)$

(middle) Mean wavefront RMS (RMS), mean pupil shift in between two pupil tracking measurements (PS), dimensions of the area in which the eye normally was (NA) ($2\sigma_x \times 2\sigma_y$), mean pupil diameter (PD), and mean number of lenslets that were used during the measurement (NL).

AOPT - Correlation of the WF RMS with

PP (x axis)	PP (y axis)	PP (ρ)	PS (x axis)	PS (y axis)	PS (ρ)
0.06	0.16	-0.1	0.35	0.21	0.37

(bottom) Correlation of the measured wavefront RMS with the measured pupil position (PP) and with the pupil shift in between each pupil tracking measurement (PS) on x axis and y axis. ρ stands for the radial position.

Figure 5.17: Subject 1: the AOPT loop.

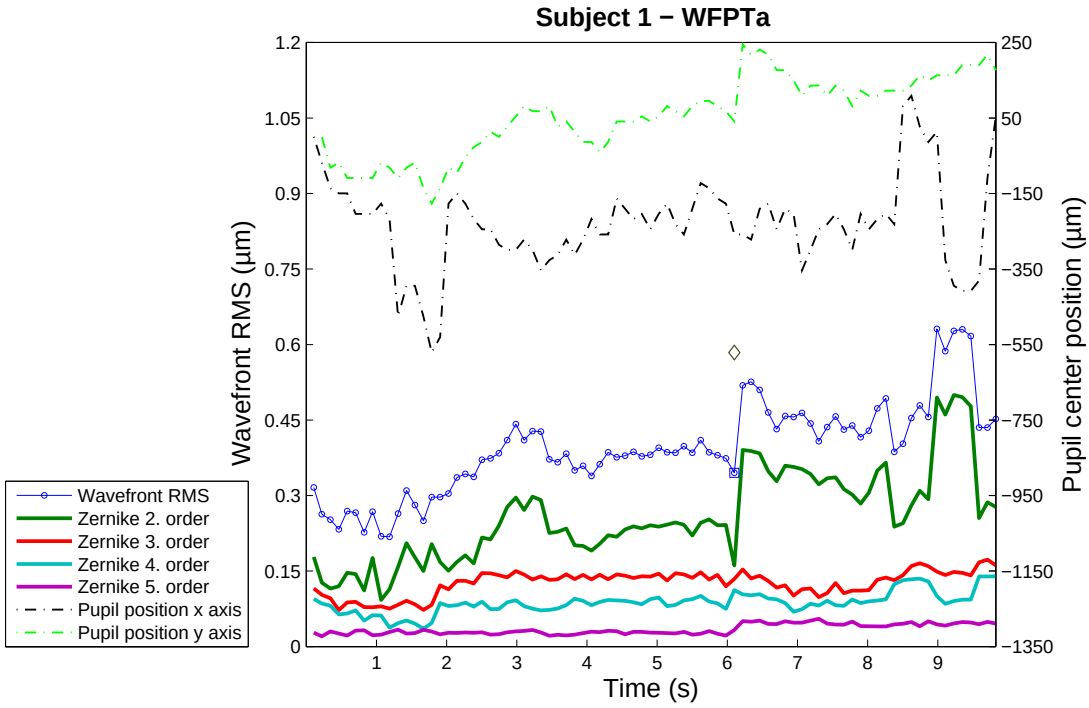

(top) Loop which incorporates the wavefront sensor, the pupil tracker and the deformable mirror that corrects the aberrations statically (WFPTa) (tilt or defocus terms are not included in the total RMS or in the Zernike coefficients).

WFPTa - Mean (μm)

RMS	PS	NA	PD	NL
0.39 ± 0.09	67 ± 72	250×210 μm^2	6300 ± 200	396 ± 12 $(lenslets)$

(middle) Mean wavefront RMS (RMS), mean pupil shift in between two pupil tracking measurements (PS), dimensions of the area in which the eye normally was (NA) ($2\sigma_x \times 2\sigma_y$), mean pupil diameter (PD), and mean number of lenslets that were used during the measurement (NL).

WFPTa - Correlation of the WF RMS with

PP (x axis)	PP (y axis)	PP (ρ)	PS (x axis)	PS (y axis)	PS (ρ)
-0.04	0.85	0.18	0.02	-0.04	0.04

(bottom) Correlation of the measured wavefront RMS with the measured pupil position (PP) and with the pupil shift in between each pupil tracking measurement (PS) on x axis and y axis. ρ stands for the radial position.

Figure 5.18: Subject 1: the WFPTa loop.

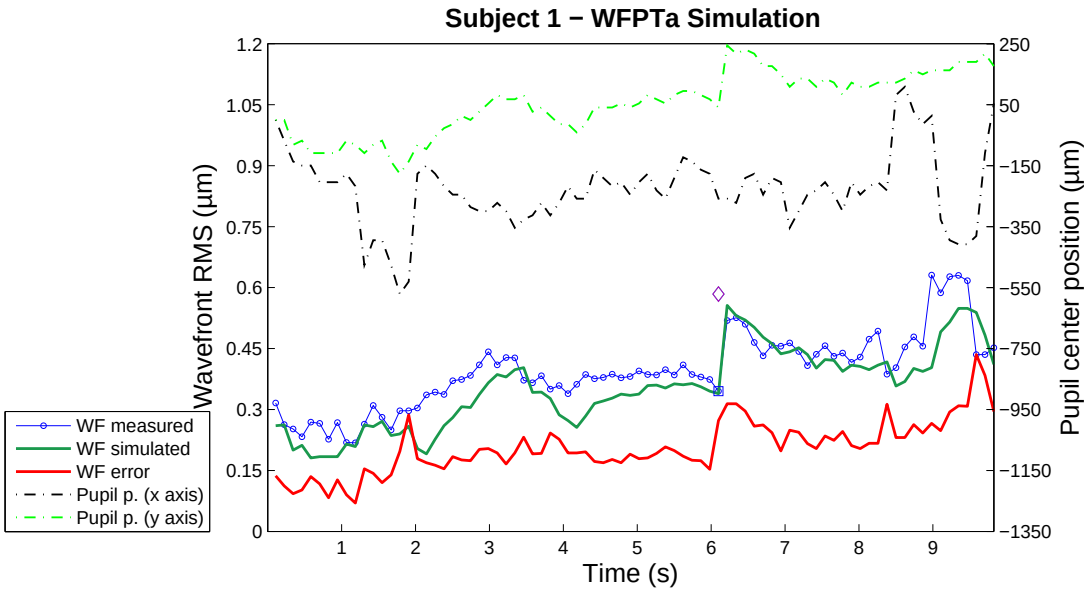

(top) RMS of the simulations of the measured wavefront aberrations changing due to eye movements (green solid line) and the residual error of the simulations (red solid line)

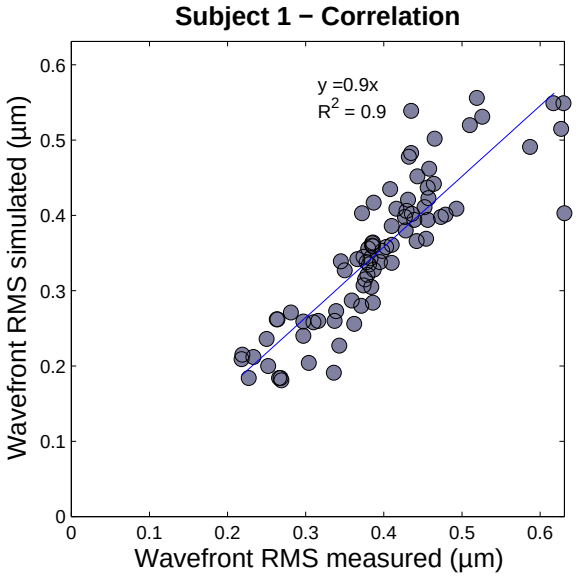

(bottom) Correlation of the RMS of the measured and the simulated wavefronts of the moving eye.

Figure 5.19: Subject 1: simulation of the WFPTa loop measurements.

Finally, the AOPTL1[20] loop was executed, Figure 5.20. The wavefront RMS was correlated with both the radial pupil position and the pupil shift at each loop, the coefficients being, 0.55 and 0.38 respectively.

Figure 5.21 - top shows all types of corrections together. Simulations done to estimate aberrations induced by eye movements had an error very similar to the error of correction for those changes real time using pupil tracking, the AOPTL1 loop, being 0.21 ± 0.07 and 0.21 ± 0.08 μm respectively. AOPTL1 loop yielded better results than the WFPTa[21] loop, the case where the correction was not dynamic and WFPT[22] loop, the case where there were no corrections.

Figure 5.21 - bottom shows the power spectra of the RMS of the all types of experiments and the simulation. The spectra spanned two and a half frequency decades; 0.07 - 4.2 Hz. The smallest frequency in the spectrum was $\frac{1}{9.8} = 0.1$ Hz, 9.8 s being the total time of the recording. The spectra on the left and the detrended spectra on the right both showed that AOPTL1 loop spectrum had the lowest magnitude. All spectra showed a 1/f like trend in the logarithmic plot. In the case of $\alpha = 1$ the power is equally distributed among the frequencies, increasing the independency and robustness of the free running system.

Finally Figure 5.22 shows the recorded pupil positions during each experiment on the x-y plane.

[20]Loop which incorporates the wavefront sensor, the deformable mirror, the pupil tracker and the control algorithm based on pupil tracking (AOPTL1)

[21]Loop which incorporates the wavefront sensor, the pupil tracker and the deformable mirror that corrects the aberrations statically (WFPTa)

[22]Loop which incorporates the wavefront sensor and the pupil tracker only (WFPT)

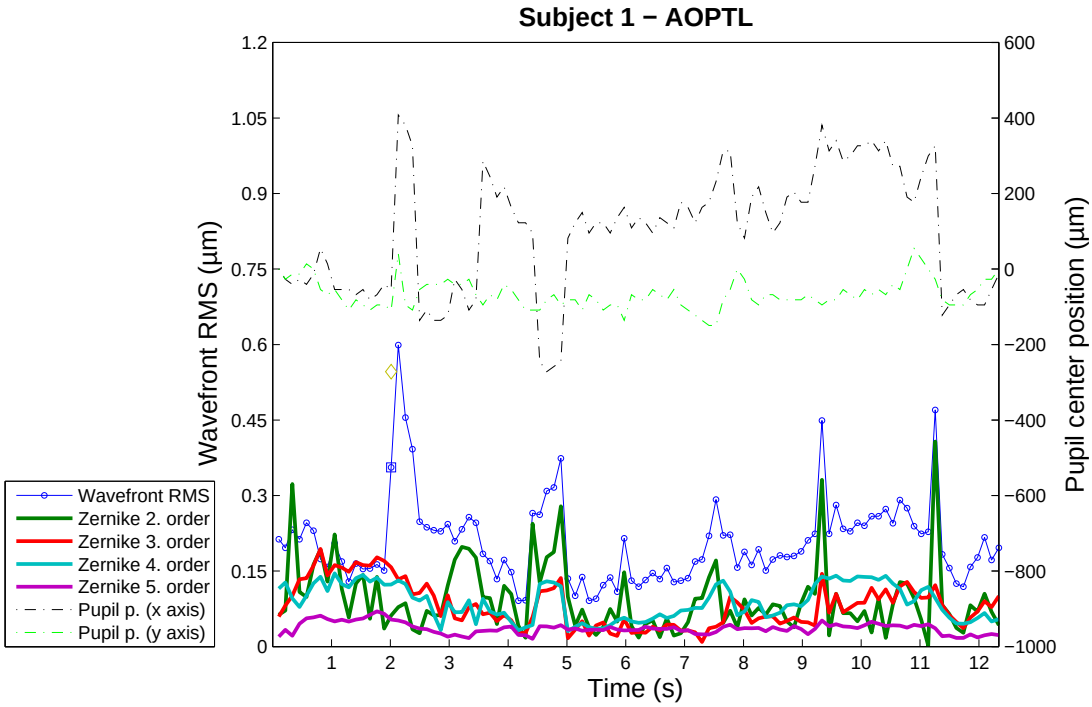

(top) Loop which incorporates the wavefront sensor, the deformable mirror, the pupil tracker and the control algorithm based on pupil tracking (AOPTL1)(tilt or defocus terms are not included in the total RMS or in the Zernike coefficients)

AOPTL1 - Mean (μm)

RMS	PS	NA	PD	NL
0.21 ± 0.08	66 ± 92	310×80 μm^2	7000 ± 200	416 ± 5 $(lenslets)$

(middle) Mean wavefront RMS (RMS), mean pupil shift in between two pupil tracking measurements (PS), dimensions of the area in which the eye normally was (NA) ($2\sigma_x \times 2\sigma_y$), mean pupil diameter (PD), and mean number of lenslets that were used during the measurement (NL).

AOPTL1- Correlation of the WF RMS with

PP (x axis)	PP (y axis)	PP (ρ)	PS (x axis)	PS (y axis)	PS (ρ)
0.22	0.23	0.55	0.21	0.38	0.25

(bottom) Correlation of the measured wavefront RMS with the measured pupil position (PP) and with the pupil shift in between each pupil tracking measurement (PS) on x axis and y axis. ρ stands for the radial position.

Figure 5.20: Subject 1: the AOPTL1 loop.

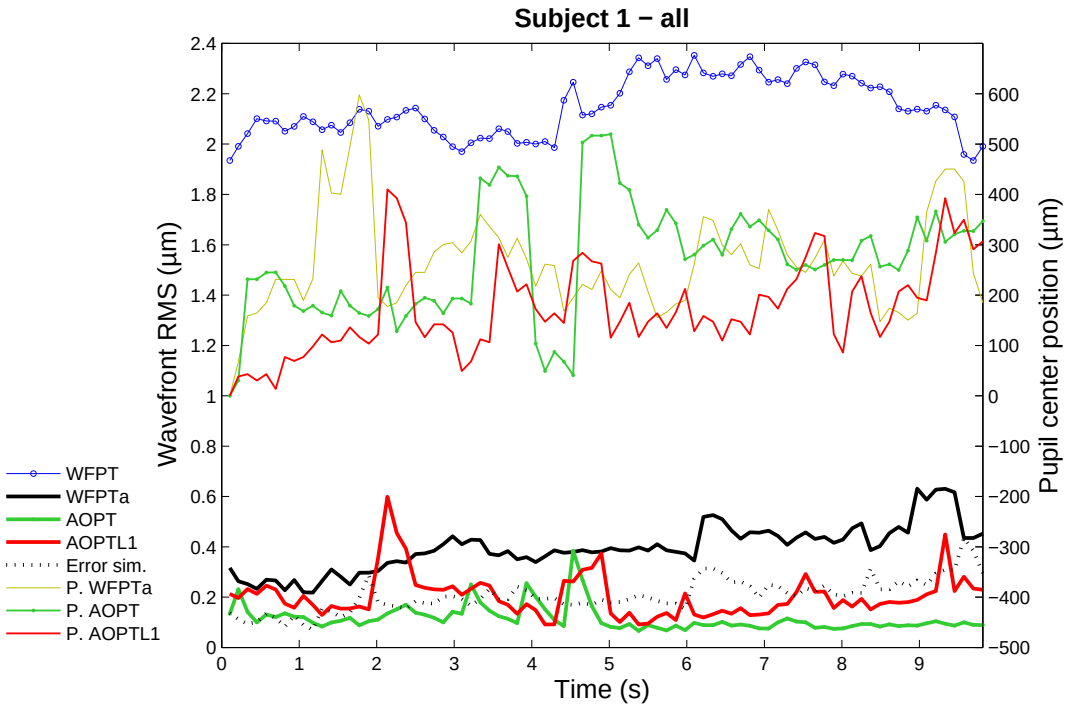

(top) Wavefront RMS of the WFPT, AOPT, WFPTa and AOPTL1 experiments and the residual error of the simulations and their respective pupil positions shown with the same color (P).

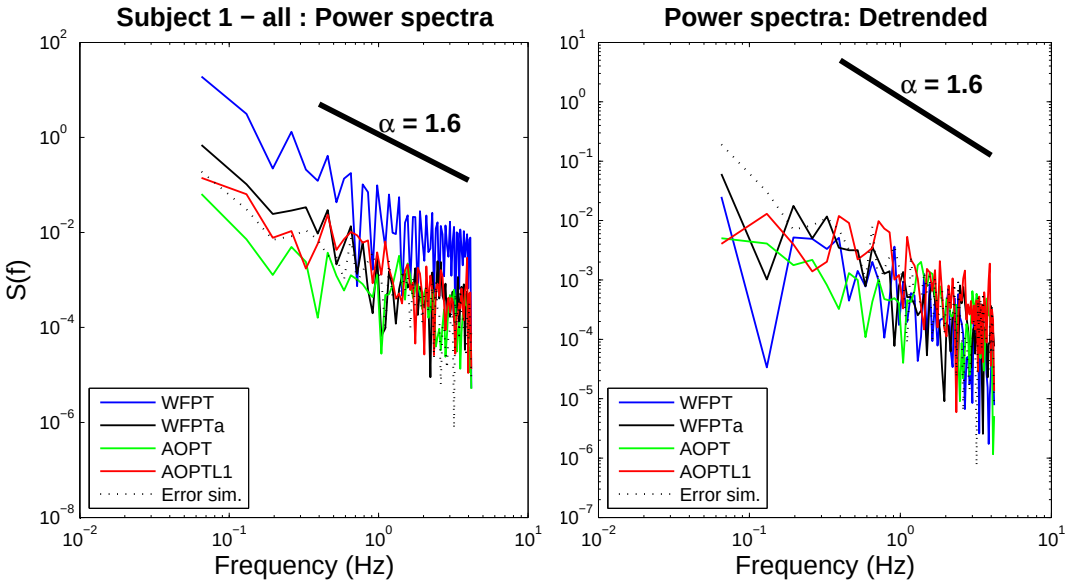

(bottom) Power spectra of the RMS of all the measurements and the residual error wavefront of the simulations (left). The detrended spectra (done after the mean of the each data set were subtracted) was made to compare the fluctuations of the signals.

Figure 5.21: Subject 1: summary of the experiments.

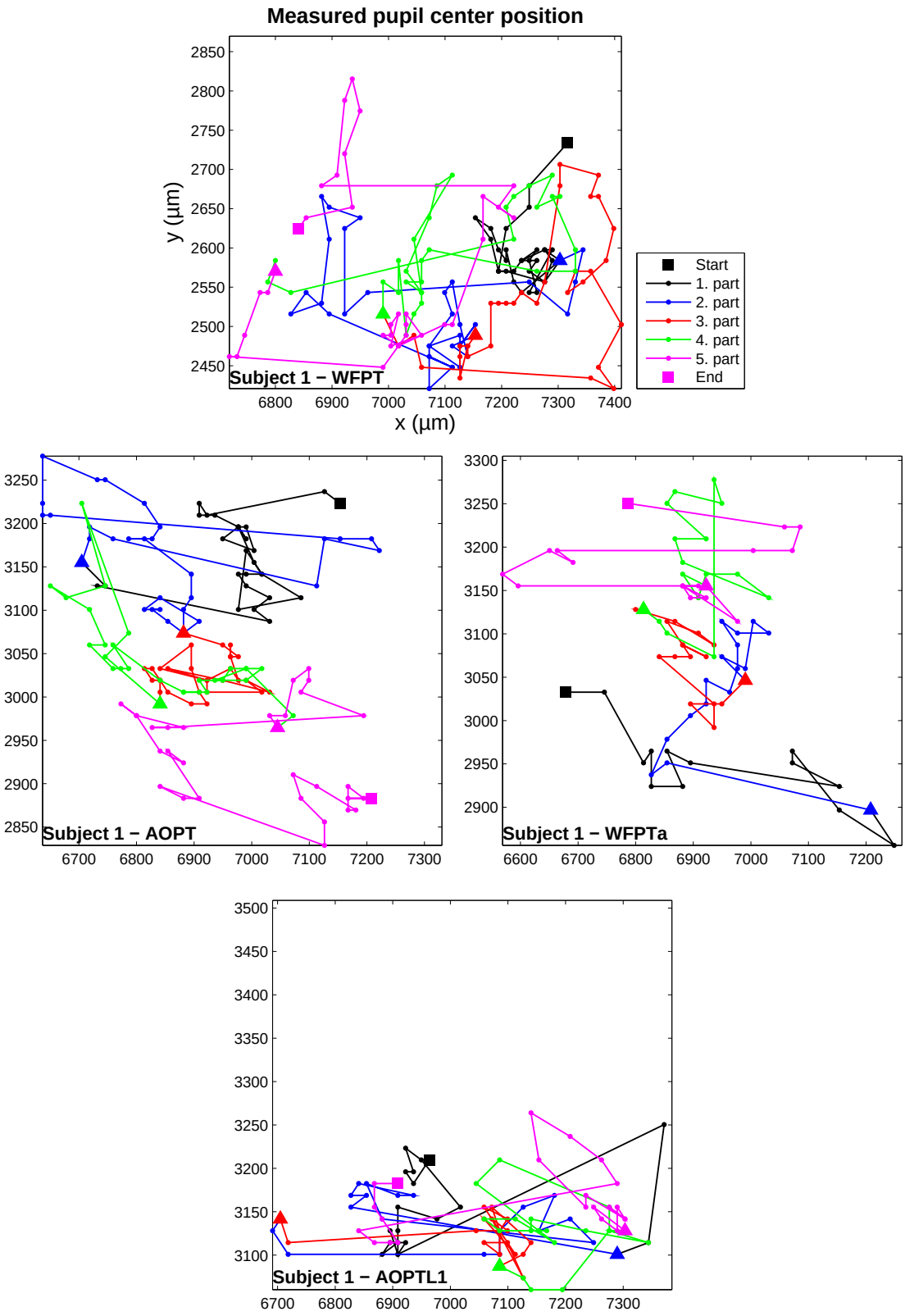

Figure 5.22: Pupil positions recorded during each experiment. All the plots have x and y axes scaled to 690×450 μm. For visual clarity the data was divided into five parts, colored differently and beginning and the end of the data were indicated by square markers.

5.3.2 Experimental results for Subject 2

First, the WFPT[23] loop was executed, see Figure 5.23. There were no relations between the RMS of the wavefronts and the pupil shift at each loop but the correlation of the RMS values with the pupil position on x axis was 0.54. The aberration changes were due to both Zernike second and third orders while the abrupt changes in these two coefficients were not represented the same way in the total wavefront RMS. This might be due to the changes in the pupil shape because Zernike reconstruction requires a circular pupil and is not successful for non circular pupil shapes. On the other hand the zonal reconstruction which was used to calculate the total RMS can estimate the wavefront at any pupil shape. This proves the zonal reconstruction method more efficient to estimate the wavefronts in case of non circular pupil shapes.

Next, the AOPT[24] and the WFPTa[25] loops was executed with the second subject's eye, Figures 5.24 and 5.25 . For the WFPTa loop the correlation of the RMS of the wavefront measurements with the pupil position on x axis was 0.79. Figure 5.26 shows the RMS of the measured, simulated wavefronts (as described in the section of the measurements done by the model eye) and residual error of the simulations.

[23]Loop which incorporates the wavefront sensor and the pupil tracker only (WFPT)

[24]Loop which incorporates the wavefront sensor, the deformable mirror, the pupil tracker and the control algorithm based on wavefront sensing (AOPT)

[25]Loop which incorporates the wavefront sensor, the pupil tracker and the deformable mirror that corrects the aberrations statically (WFPTa)

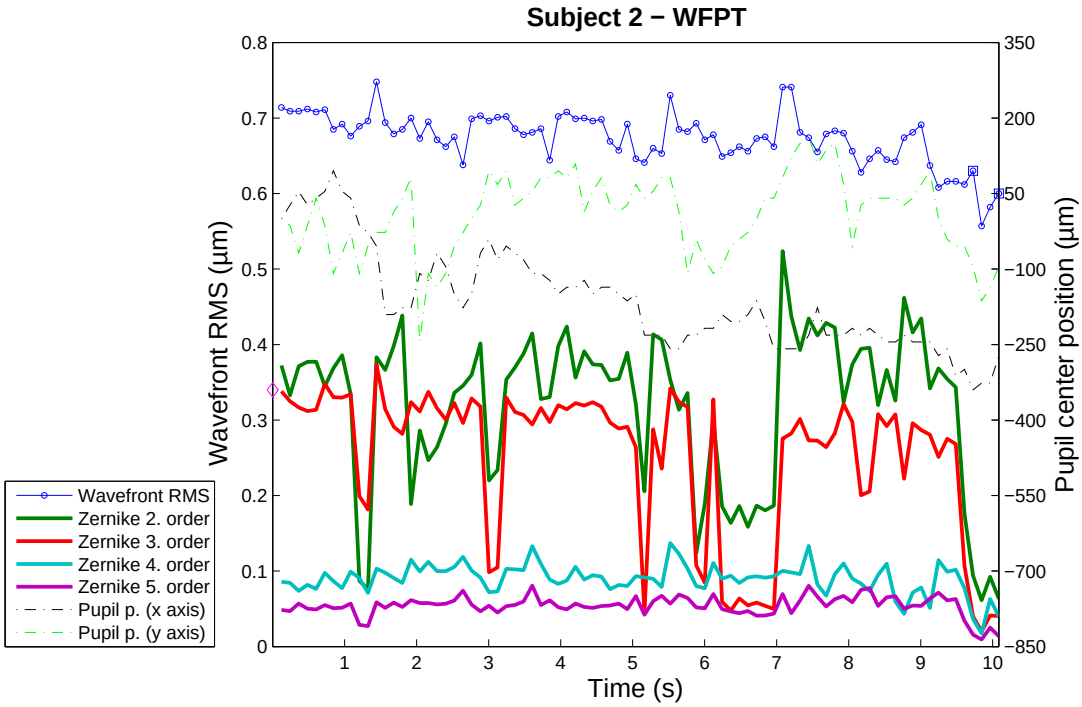

(top) Loop which incorporates the wavefront sensor and the pupil tracker only (WFPT)(tilt or defocus terms are not included in the total RMS or in the Zernike coefficients).

WFPT - Mean (μm)

RMS	PS	NA	PD	NL
0.67 ± 0.03	53 ± 43	200×160 μm^2	6300 ± 100	$408 \pm 14(lenslets)$

(middle) Mean wavefront RMS (RMS), mean pupil shift in between two pupil tracking measurements (PS), dimensions of the area in which the eye normally was (NA) ($2\sigma_x \times 2\sigma_y$), mean pupil diameter (PD), and mean number of lenslets that were used during the measurement (NL).

WFPT - Correlation of the WF RMS with

PP (x axis)	PP (y axis)	PP (ρ)	PS (x axis)	PS (y axis)	PS (ρ)
0.54	-0.32	-0.57	-0.01	0.03	0.03

(bottom) Correlation of the measured wavefront RMS with the measured pupil position (PP) and with the pupil shift in between each pupil tracking measurement (PS) on x axis and y axis. ρ stands for the radial position.

Figure 5.23: Subject 2: the WFPT loop.

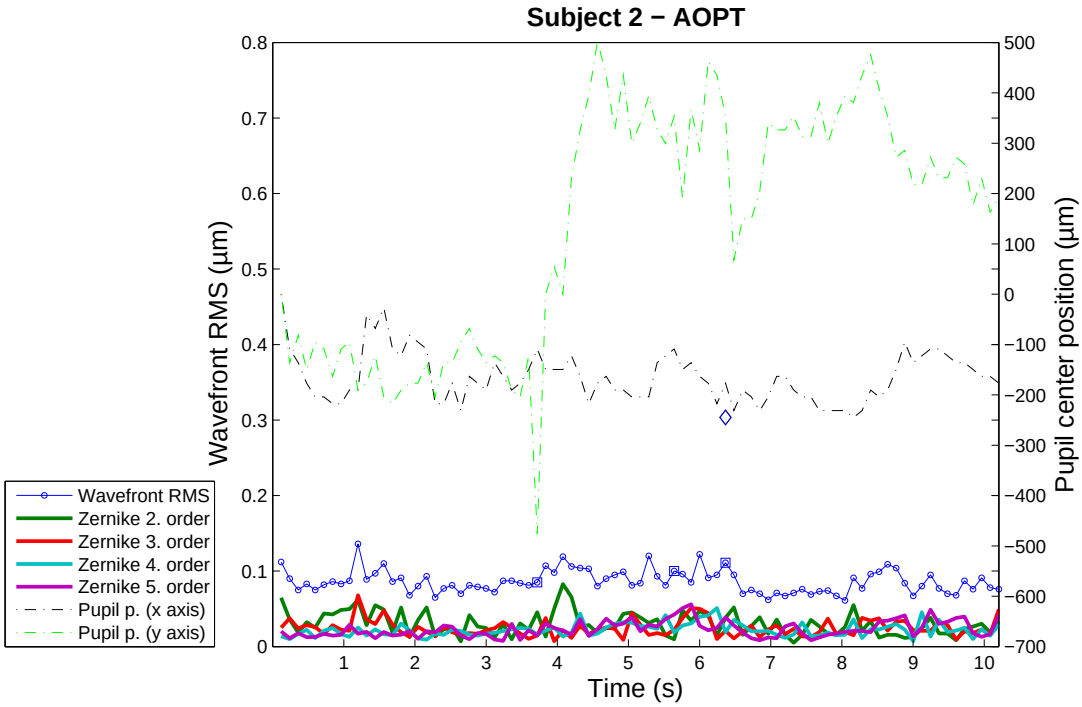

(top) Loop which incorporates the wavefront sensor, the deformable mirror, the pupil tracker and the control algorithm based on wavefront sensing (AOPT)

AOPT - Mean (μm)

RMS	PS	NA	PD	NL
0.09 ± 0.01	79 ± 73	100×470 μm^2	6900 ± 60	401 ± 7 ($lenslets$)

(middle) Mean wavefront RMS (RMS), mean pupil shift in between two pupil tracking measurements (PS), dimensions of the area in which the eye normally was (NA) ($2\sigma_x \times 2\sigma_y$), mean pupil diameter (PD), and mean number of lenslets that were used during the measurement (NL).

AOPT - Correlation of the WF RMS with

PP (x axis)	PP (y axis)	PP (ρ)	PS (x axis)	PS (y axis)	PS (ρ)
-0.23	-0.02	-0.04	-0.01	0.29	0.27

(bottom) Correlation of the measured wavefront RMS with the measured pupil position (PP) and with the pupil shift in between each pupil tracking measurement (PS) on x axis and y axis. ρ stands for the radial position.

Figure 5.24: Subject 2: the AOPT loop.

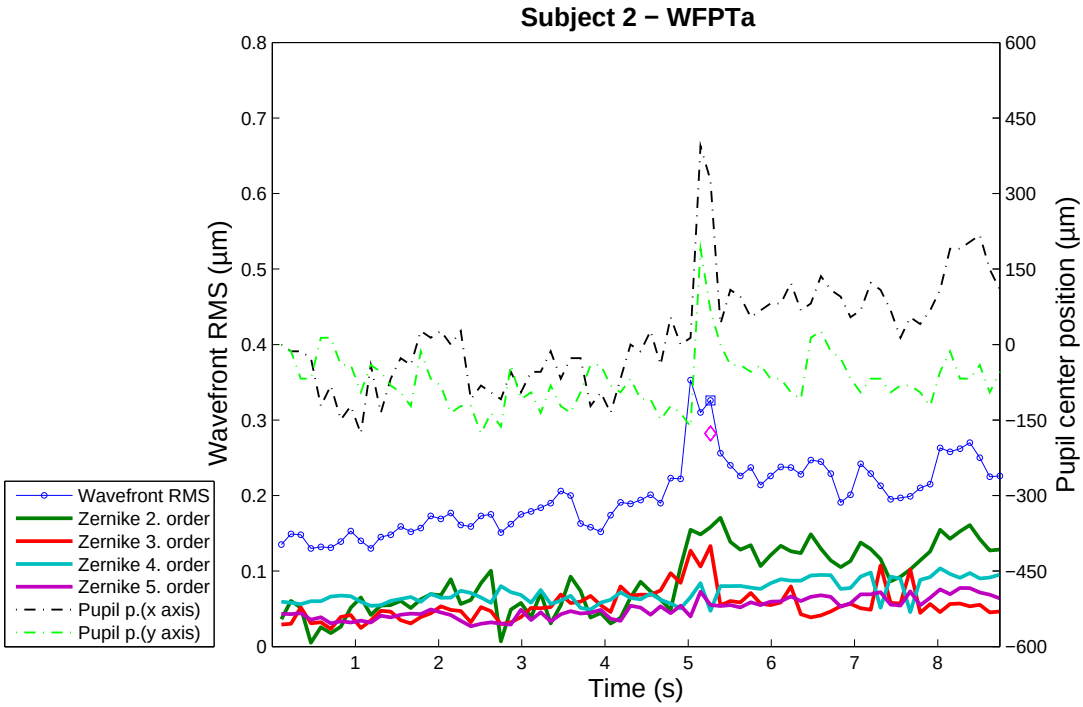

(top) Loop which incorporates the wavefront sensor, the pupil tracker and the deformable mirror that corrects the aberrations statically (WFPTa)(tilt or defocus terms are not included in the total RMS or in the Zernike coefficients).

WFPTa - Mean (μm)

RMS	PS	NA	PD	NL
0.20 ± 0.05	68 ± 70	220×120 μm^2	6430 ± 90	396 ± 10 $(lenslets)$

(middle) Mean wavefront RMS (RMS), mean pupil shift in between two pupil tracking measurements (PS), dimensions of the area in which the eye normally was (NA) ($2\sigma_x \times 2\sigma_y$), mean pupil diameter (PD), and mean number of lenslets that were used during the measurement (NL).

WFPTa - Correlation of the WF RMS with

PP (x axis)	PP (y axis)	PP (ρ)	PS (x axis)	PS (y axis)	PS (ρ)
-0.79	0.21	0.48	0.18	0.27	0.24

(bottom) Correlation of the measured wavefront RMS with the measured pupil position (PP) and with the pupil shift in between each pupil tracking measurement (PS) on x axis and y axis. ρ stands for the radial position.

Figure 5.25: Subject 2: the WFPTa loop.

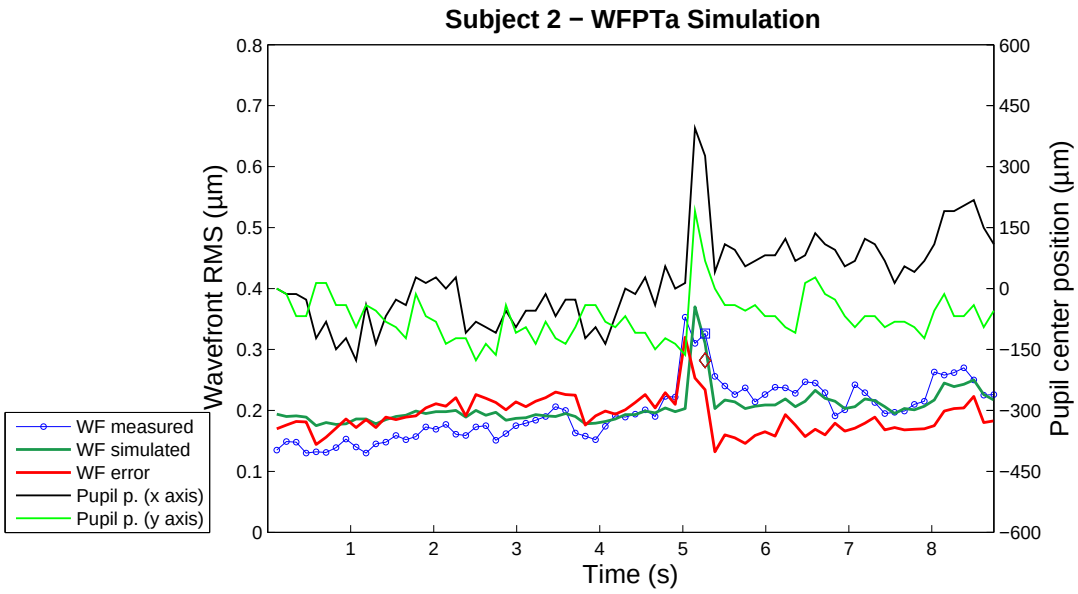

(top) RMS of the simulations of the measured wavefront aberrations changing due to eye movements (green solid line) and the residual error of the simulations (red solid line)

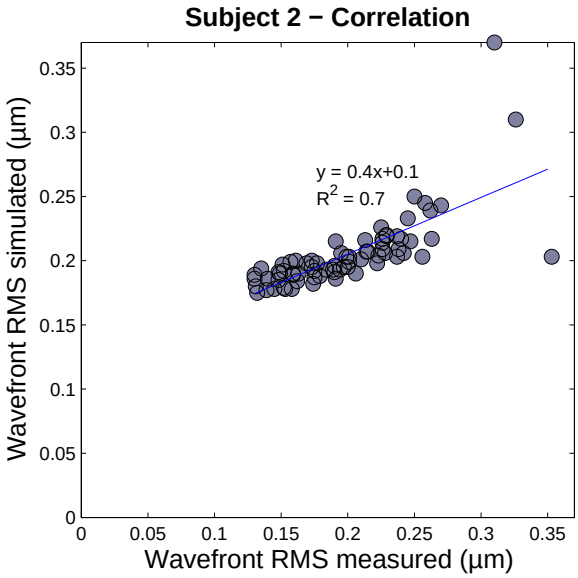

(bottom) Correlation of the RMS of the measured and the simulated wavefronts of the moving eye.

Figure 5.26: Subject 2: simulation of the WFPTa loop measurements.

In the Figure 5.26 - top, the mean RMS of the simulated wavefronts and the residual error of the simulation was 0.20 ± 0.05 and 0.19 ± 0.03 μm respectively. The experiment can be divided into two time periods; before and after the spike at the $\sim 5^{th}$ second. In the first half of the simulation the simulated wavefronts over-estimated the aberration whereas in the second half just after the spike, the simulation estimated the measured aberrations better. In the first half probably the estimation was not good because of the not suitable reference wavefront (tear film rupture just before the blink). It is probable that whatever happened after the spike changed the aberrations of the eye and the estimations was able to follow the changes. The square and diamond markers indicate discontinuity in the wavefront sensor and the pupil tracker measurement data respectively due to a blink or other reasons. When the fast eye movement was followed by the blink and aberrations of the eye were changed, the reference wavefront became relevant and the estimation gave good results. At the first part of the measurements the estimation was quite static and was not able to follow changes in the wavefront RMS which showed itself as a linear distribution concentrated at 0.2 μm RMS in the correlation graph of the RMS of the simulated and the measured wavefronts in Figure 5.26 - bottom.

Finally, the AOPTL1[26] and AOPTL2[27] loops were performed, Figures 5.27 and 5.28. Figure 5.29 - top shows the results of all the experiments.

[26]Loop which incorporates the wavefront sensor, the deformable mirror, the pupil tracker and the control algorithm based on pupil tracking (AOPTL1)

[27]Loop which incorporates the wavefront sensor, the deformable mirror, the pupil tracker and the control algorithms based on wavefront sensing and pupil tracking (AOPTL2)

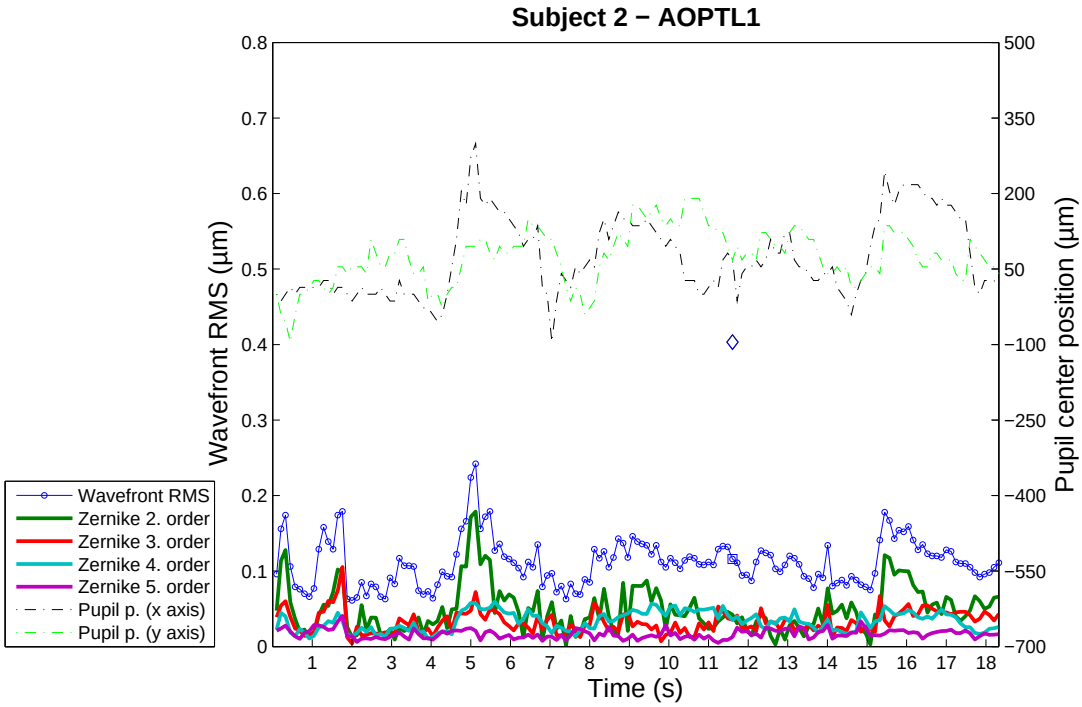

(top) Loop which incorporates the wavefront sensor, the deformable mirror, the pupil tracker and the control algorithm based on pupil tracking (AOPTL1)

AOPTL1 - Mean (μm)

RMS	PS	NA	PD	NL
0.11 ± 0.03	32 ± 26	160×110 μm^2	7030 ± 60	404 ± 4 ($lenslets$)

(middle) Mean wavefront RMS (RMS), mean pupil shift in between two pupil tracking measurements (PS), dimensions of the area in which the eye normally was (NA) ($2\sigma_x \times 2\sigma_y$), mean pupil diameter (PD), and mean number of lenslets that were used during the measurement (NL).

AOPTL1- Correlation of the WF RMS with

PP (x axis)	PP (y axis)	PP (ρ)	PS (x axis)	PS (y axis)	PS (ρ)
-0.66	0.29	0.66	0.12	0.01	0.11

(bottom) Correlation of the measured wavefront RMS with the measured pupil position (PP) and with the pupil shift in between each pupil tracking measurement (PS) on x axis and y axis. ρ stands for the radial position.

Figure 5.27: Subject 2: the AOPTL1 loop.

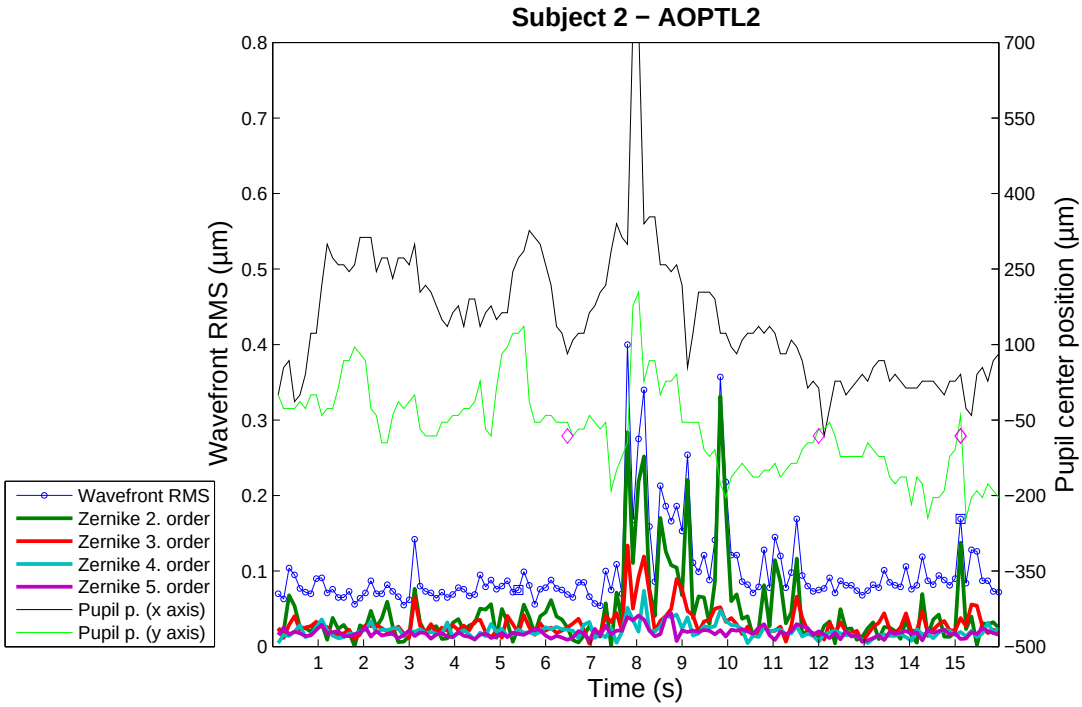

(top) Loop which incorporates the wavefront sensor, the deformable mirror, the pupil tracker and the control algorithms based on wavefront sensing and pupil tracking (AOPTL2)

AOPTL2 - Mean (μm)

RMS	PS	NA	PD	NL
0.10 ± 0.06	50 ± 65	260×180 μm^2	7000 ± 100	395 ± 8 $(lenslets)$

(middle) Mean wavefront RMS (RMS), mean pupil shift in between two pupil tracking measurements (PS), dimensions of the area in which the eye normally was (NA) ($2\sigma_x \times 2\sigma_y$), mean pupil diameter (PD), and mean number of lenslets that were used during the measurement (NL).

AOPTL2- Correlation of the WF RMS with

PP (x axis)	PP (y axis)	PP (ρ)	PS (x axis)	PS (y axis)	PS (ρ)
0.25	-0.06	0.3	0.34	0.24	0.34

(bottom) Correlation of the measured wavefront RMS with the measured pupil position (PP) and with the pupil shift in between each pupil tracking measurement (PS) on x axis and y axis. ρ stands for the radial position.

Figure 5.28: Subject 2: the AOPTL2 loop.

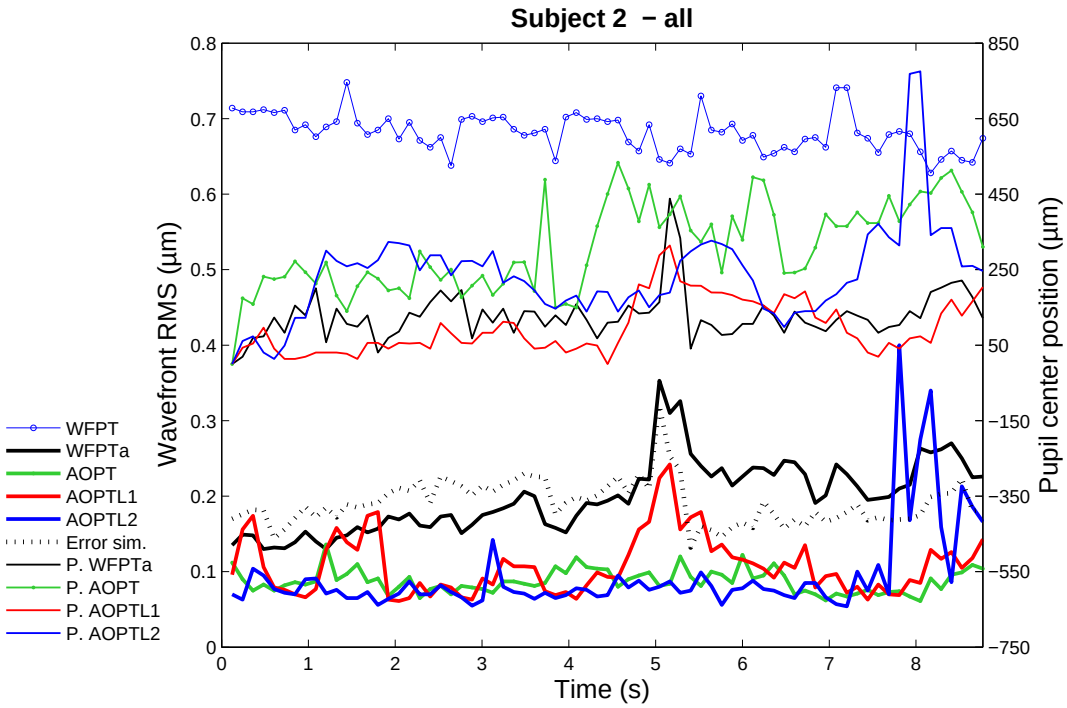

(top) Wavefront RMS of the WFPT, AOPT, WFPTa, AOPTL1 and AOPTL2 experiments and the residual error of the simulations and their respective pupil positions shown with the same color (P).

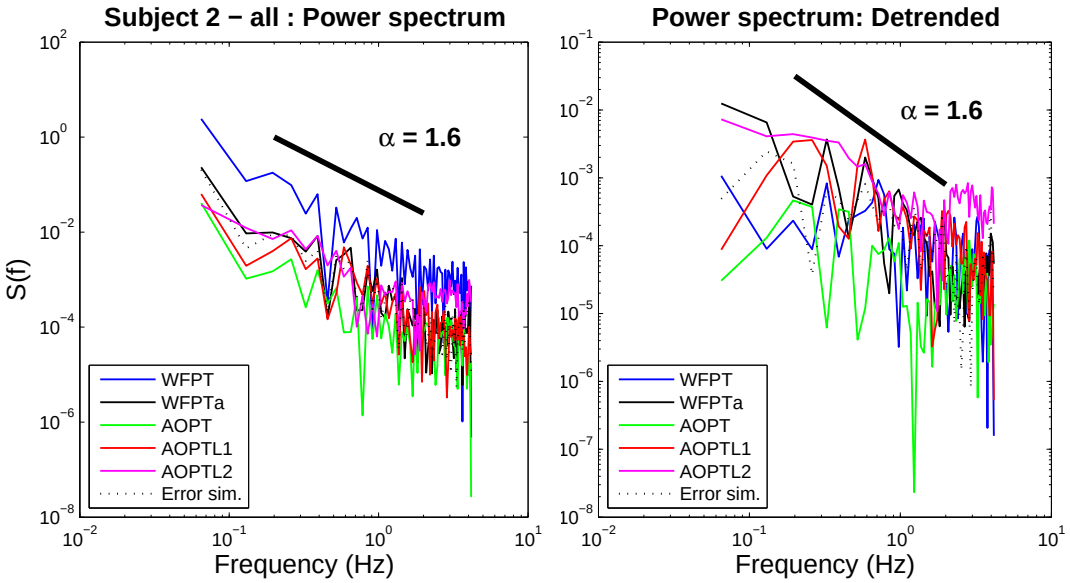

(bottom) Power spectra of the RMS of all the measurements and the residual error wavefront of the simulations (left). The detrended spectra (done after the mean of the each data set were subtracted) was made to compare the fluctuations of the signals.

Figure 5.29: Subject 2: summary of the experiments.

The AOPTL2[28] loop which used both control algorithms did a better job than the AOPT[29] except the spike at the end. Possibly because of the long acquisition times of the pupil camera and the time lag, AOPTL2 might have introduced errors when there was a sudden shift; therefore it is possible that AOPT might have handled this shift much better than the AOPTL2 loop. But for gentle movements of the eye, AOPTL2 might be more advantageous than the AOPT even at this rate of pupil tracking as we can see in the measurements just before the spike, Figure 5.29 - top.

Figure 5.29 - bottom shows the spectra of all the experiments. The spectra spanned two frequency decades from 0.07 to 4.2 Hz. The AOPT loop had the lowest amplitude and fluctuation as seen from the spectra on the left and the detrended spectra on the right. Amplitude of all the spectra decreased by increasing frequencies with the same $1/f^{\alpha}$ like trend as seen in the Subject 1 and the model eye. The value of α may have important implications in terms of health as revealed by several authors but this will be discussed in the final section.

Finally Figure 5.30 shows the recorded pupil positions during each experiment on the x-y plane.

[28]Loop which incorporates the wavefront sensor, the deformable mirror, the pupil tracker and the control algorithms based on wavefront sensing and pupil tracking (AOPTL2)

[29]Loop which incorporates the wavefront sensor, the deformable mirror, the pupil tracker and the control algorithm based on wavefront sensing (AOPT)

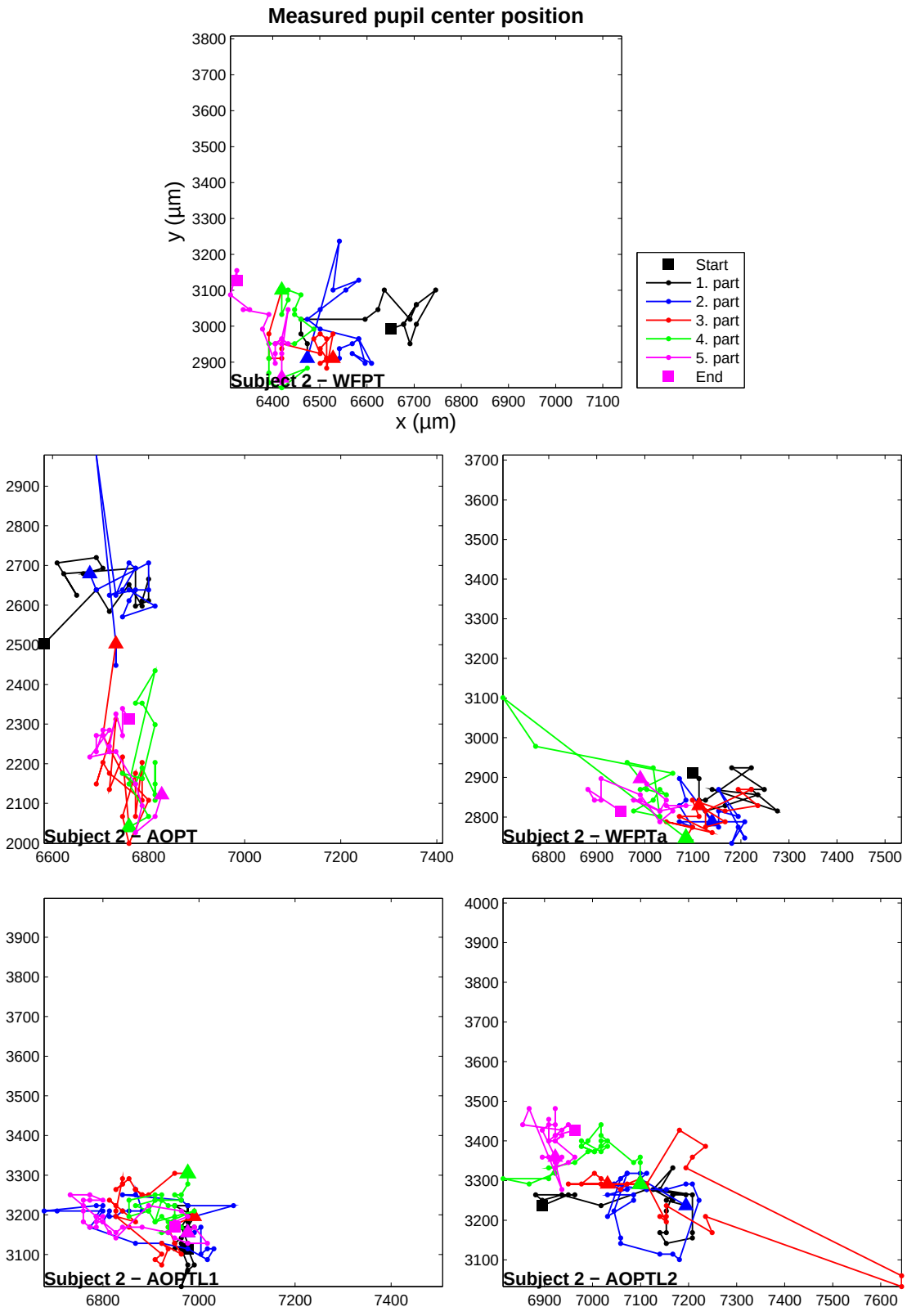

Figure 5.30: Pupil positions recorded during each experiment. All the plots have x and y axes scaled to 830×980 μm. For visual clarity the data was divided into five parts, colored differently and beginning and the end of the data were indicated by square markers.

5.3.3 Experimental results for Subject 3

First, the WFPT[30] loop was executed, see Figure 5.31. The wavefront RMS was related to the pupil position on x axis was with a correlation coefficient of 0.3. Zernike second, third and fourth orders contributed to the aberration changes; they were even more related to the pupil displacement than the total RMS. The square markers on the wavefront RMS curve indicate the discontinuities where the measurement was interrupted and the slopes could not be acquired due to a blink or a misalignment. The downward spikes of the Zernike curves are probably due to the changes in pupil shape and are calculation errors.

Second, the AOPT[31] loop was performed, Figure 5.32. There was not a significant relation between the wavefront RMS and the pupil displacement at each loop or the pupil position. The correction done with the control algorithm based on wavefront sensor measurements had higher residual error than usual for a reason unknown. It might have been because of an erroneous wavefront sensor measurement at the beginning of the loop. In fact to avoid the affect of random wrong sensor measurements on the overall correction, the gain of the deformable mirror had been chosen to be 0.5. In this case it takes longer to correct (10 loops in average) but it is more effective in handling wrong wavefront sensor measurements.

[30]Loop which incorporates the wavefront sensor and the pupil tracker only (WFPT)

[31]Loop which incorporates the wavefront sensor, the deformable mirror, the pupil tracker and the control algorithm based on wavefront sensing (AOPT)

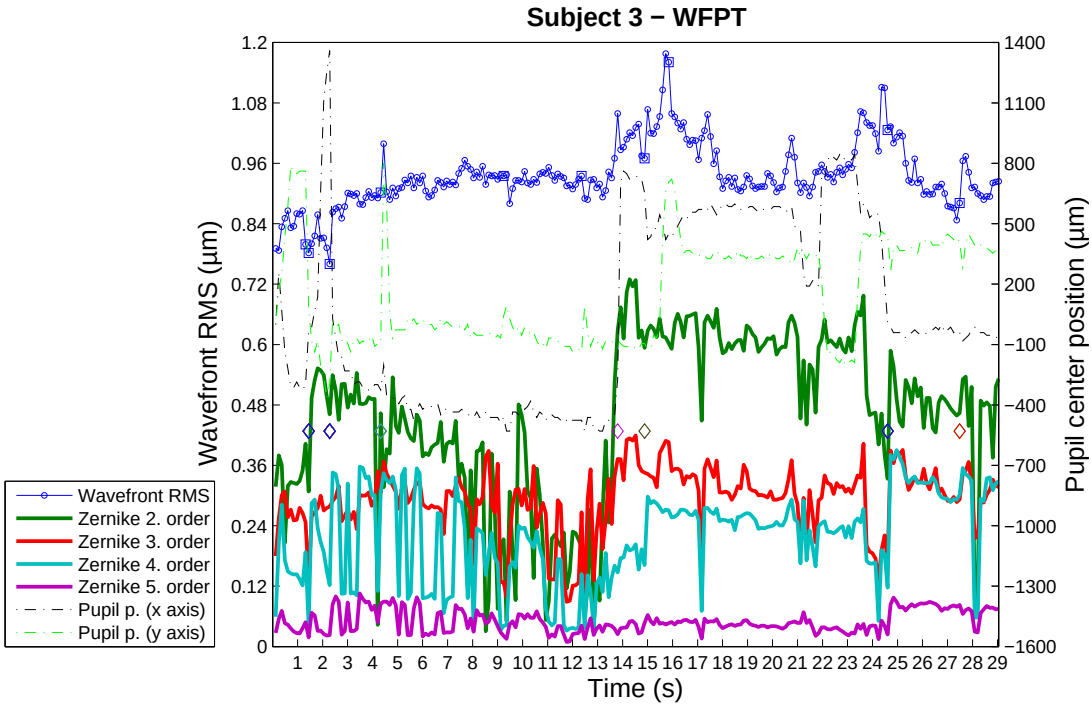

(top) Loop which incorporates the wavefront sensor and the pupil tracker only (WFPT) (tilt or defocus terms are not included in the total RMS or in the Zernike coefficients).

WFPT - Mean (μm)

RMS	PS	NA	PD	NL
0.94 ± 0.06	77 ± 173	940×520 μm^2	6300 ± 100	361 ± 33 ($lenslets$)

(middle) Mean wavefront RMS (RMS), mean pupil shift in between two pupil tracking measurements (PS), dimensions of the area in which the eye normally was (NA) ($2\sigma_x \times 2\sigma_y$), mean pupil diameter (PD), and mean number of lenslets that were used during the measurement (NL).

WFPT - Correlation of the WF RMS with

PP (x axis)	PP (y axis)	PP (ρ)	PS (x axis)	PS (y axis)	PS (ρ)
0.31	0.19	0.25	-0.08	-0.01	-0.05

(bottom) Correlation of the measured wavefront RMS with the measured pupil position (PP) and with the pupil shift in between each pupil tracking measurement (PS) on x axis and y axis. ρ stands for the radial position.

Figure 5.31: Subject 3: the WFPT loop.

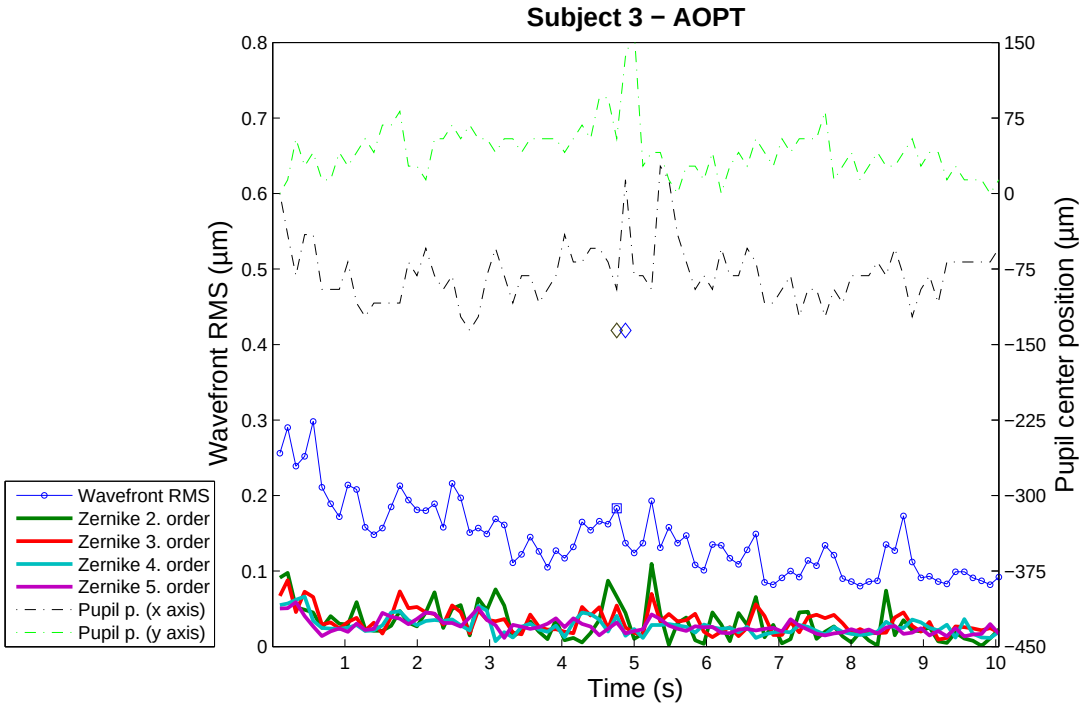

(top) Loop which incorporates the wavefront sensor, the deformable mirror, the pupil tracker and the control algorithm based on wavefront sensing (AOPT)

AOPT - Mean (μm)

RMS	PS	NA	PD	NL
0.14 ± 0.05	33 ± 26	60×60 μm^2	6500 ± 60	394 ± 7 $(lenslets)$

(middle) Mean wavefront RMS (RMS), mean pupil shift in between two pupil tracking measurements (PS), dimensions of the area in which the eye normally was (NA) ($2\sigma_x \times 2\sigma_y$), mean pupil diameter (PD), and mean number of lenslets that were used during the measurement (NL).

AOPT - Correlation of the WF RMS with

PP (x axis)	PP (y axis)	PP (ρ)	PS (x axis)	PS (y axis)	PS (ρ)
-0.19	-0.07	-0.16	0.08	0.10	0.09

(bottom) Correlation of the measured wavefront RMS with the measured pupil position (PP) and with the pupil shift in between each pupil tracking measurement (PS) on x axis and y axis. ρ stands for the radial position.

Figure 5.32: Subject 3: the AOPT loop.

Next, the WFPTa[32] loop was executed with the third subject's eye, Figure 5.33. The correlation of the RMS of the wavefront measurements with the pupil position on x axis was 0.94. In the first nine seconds the eye was fixating well and the static deformable mirror correction was valid but then subject slightly changed the point of fixation and continued fixating at around 500 microns away. This shift was different than a micro saccade, because it was not towards the center and the way the eye continued being stable afterwards shows that it was indeed a conscious displacement of the eye.

The aberrations were simulated using the methodology of the control algorithm based on pupil tracking, see the RMS of measured, simulated and error wavefronts in Figure 5.34. The mean RMS of the simulated wavefronts and the residual error of the simulation was 0.47 ± 0.30 and 0.16 ± 0.09 μm respectively. The estimation was accurate except for the 2^{th}, 5^{th}, 7^{th} and 14^{th} seconds at which the eye made quick round trips which were not sensed during the exposure of the wavefront sensing camera and did not effect wavefront RMS measured but were measured as pupil shifts by the pupil tracking camera because of its shorter exposure time and effected the estimation done based on pupil tracking. Also the big error spike on 9^{th} second was probably due to the fact that there was a time lag between the pupil tracker and the wavefront sensor and the estimation was late. In the Figure 5.34 - bottom the distribution of the data points for the measured and the simulated data showed a high correlation and the two distinct points indicate the two different fixation levels. The data that the red arrow points to belongs to the 9^{th} second where although the pupil moved to the next level of fixation and the wavefront RMS changed, the pupil tracker and as a result the simulation was late to follow.

[32]Loop which incorporates the wavefront sensor, the pupil tracker and the deformable mirror that corrects the aberrations statically (WFPTa)

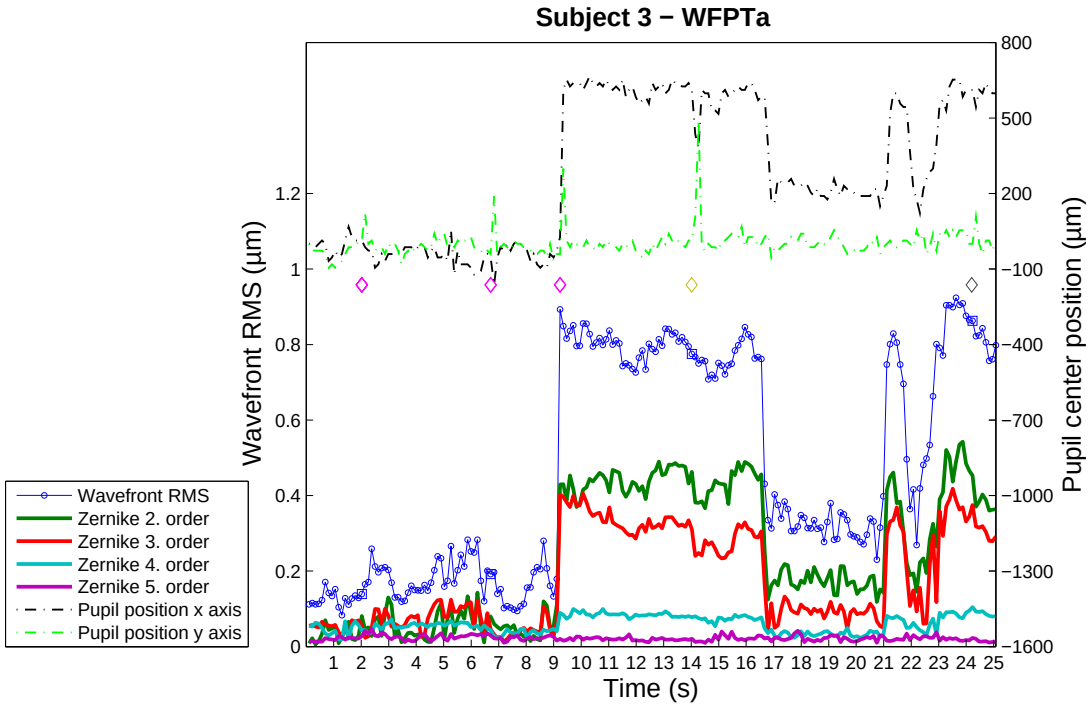

(top) Loop which incorporates the wavefront sensor, the pupil tracker and the deformable mirror that corrects the aberrations statically (WFPTa)(tilt or defocus terms are not included in the total RMS or in the Zernike coefficients).

WFPTa - Mean (μm)

RMS	PS	NA	PD	NL
0.47 ± 0.29	54 ± 78	580×110 μm^2	6300 ± 300	357 ± 19 $(lenslets)$

(middle) Mean wavefront RMS (RMS), mean pupil shift in between two pupil tracking measurements (PS), dimensions of the area in which the eye normally was (NA) ($2\sigma_x \times 2\sigma_y$), mean pupil diameter (PD), and mean number of lenslets that were used during the measurement (NL).

WFPTa - Correlation of the WF RMS with

PP (x axis)	PP (y axis)	PP (ρ)	PS (x axis)	PS (y axis)	PS (ρ)
0.94	-0.26	0.95	0.11	0.11	0.13

(bottom) Correlation of the measured wavefront RMS with the measured pupil position (PP) and with the pupil shift in between each pupil tracking measurement (PS) on x axis and y axis. ρ stands for the radial position.

Figure 5.33: Subject 3: the WFPTa loop.

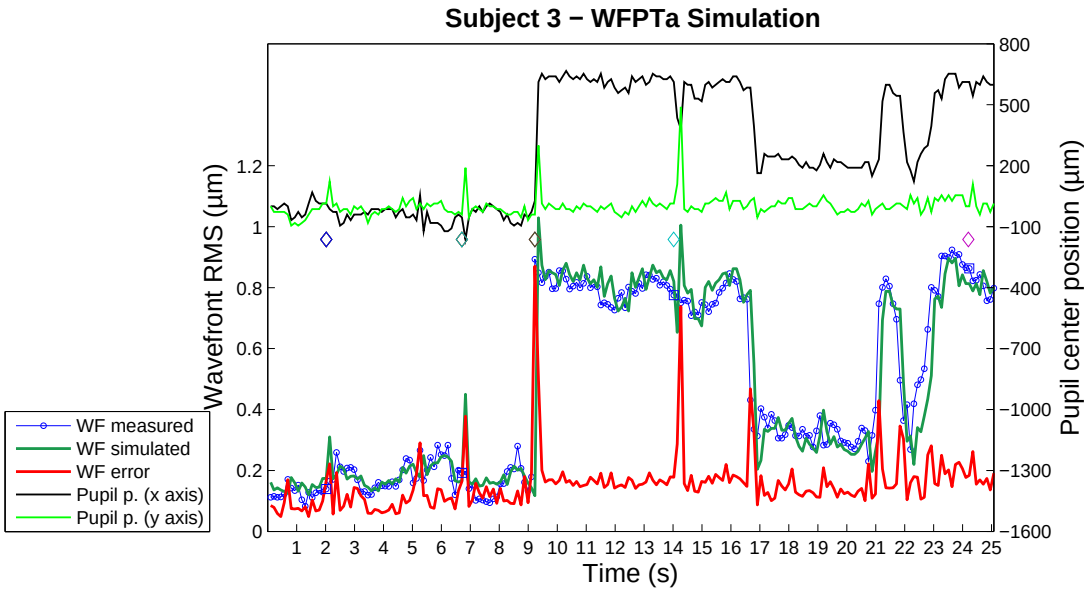

(top) RMS of the simulations of the measured wavefront aberrations changing due to eye movements (green solid line) and the residual error of the simulations (red solid line)

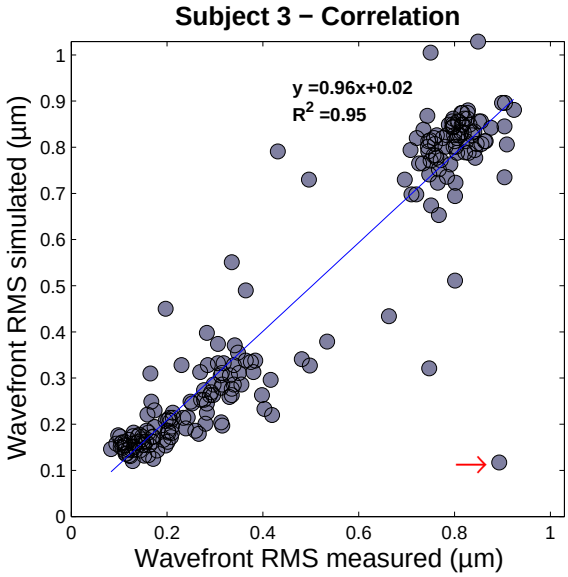

(bottom) Correlation of the RMS of the measured and the simulated wavefronts of the moving eye.

Figure 5.34: Subject 3: simulation of the WFPTa loop measurements.

Finally, the AOPTL1[33] and AOPTL2[34] loops were performed, Figures 5.35 and 5.36. Figure 5.37 - top shows results of the all types of correction loops together.

The simulations estimated the pupil shift well until the large movement of the eye at the 9^{th} second because of the time lag between the pupil tracker and the wavefront sensor. AOPTL1 corrected as well as AOPT[35] taking into account the fact that the quality of the AOPT correction was not good probably because of an erroneous wavefront sensor measurement.

Figure 5.37 - bottom shows the spectra of all the experiments. The spectra spanned two frequency decades from 0.07 to 4.2 Hz. The AOPTL2 loop had the lowest amplitude as seen from the spectra on the left and while the WFPTa loop had the largest magnitude of fluctuations in the detrended spectra on the right. Amplitude of all the spectra decreased by increasing frequencies with the same $1/f^{\alpha}$ like trend as seen in the previous experiments α being ~ 1.4.

Finally Figure 5.38 shows the recorded pupil positions during each experiment on the x-y plane.

[33]Loop which incorporates the wavefront sensor, the deformable mirror, the pupil tracker and the control algorithm based on pupil tracking (AOPTL1)

[34]Loop which incorporates the wavefront sensor, the deformable mirror, the pupil tracker and the control algorithms based on wavefront sensing and pupil tracking (AOPTL2)

[35]Loop which incorporates the wavefront sensor, the deformable mirror, the pupil tracker and the control algorithm based on wavefront sensing (AOPT)

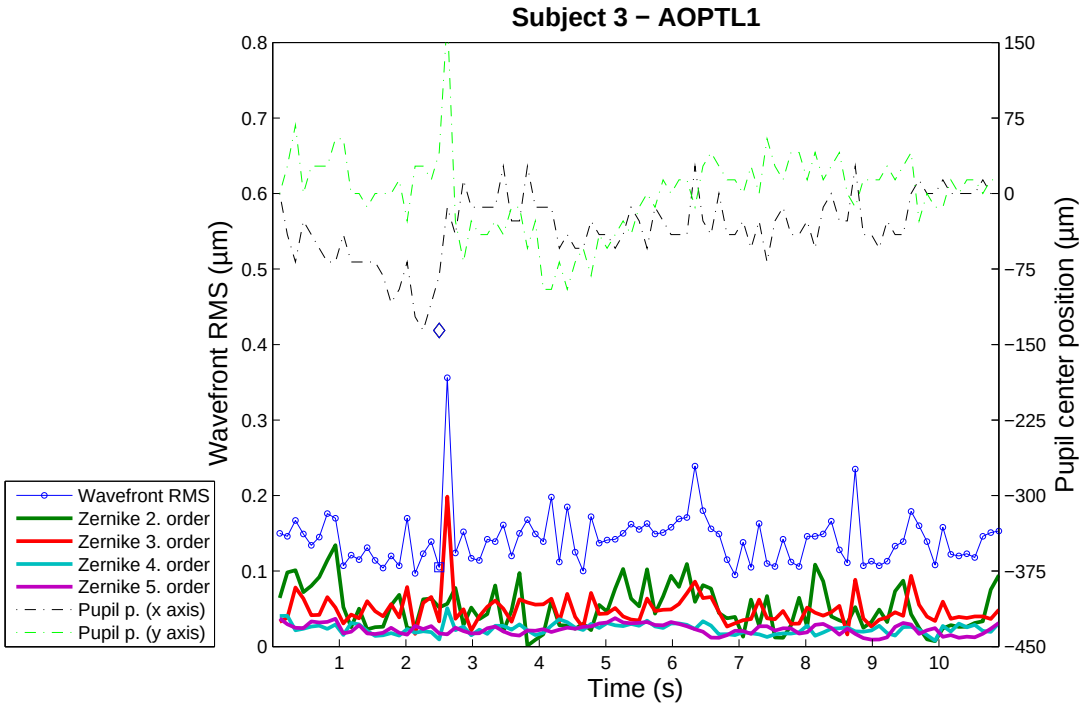

(top) Loop which incorporates the wavefront sensor, the deformable mirror, the pupil tracker and the control algorithm based on pupil tracking (AOPTL1)

AOPTL1 - Mean (μm)

RMS	PS	NA	PD	NL
0.14 ± 0.04	34 ± 31	70×80 μm^2	6500 ± 40	389 ± 3 $(lenslets)$

(middle) Mean wavefront RMS (RMS), mean pupil shift in between two pupil tracking measurements (PS), dimensions of the area in which the eye normally was (NA) ($2\sigma_x \times 2\sigma_y$), mean pupil diameter (PD), and mean number of lenslets that were used during the measurement (NL).

AOPTL1- Correlation of the WF RMS with

PP (x axis)	PP (y axis)	PS (x axis)	PS (y axis)		
-0.36	-0.15	0.17	0.33	0.26	0.32

(bottom) Correlation of the measured wavefront RMS with the measured pupil position (PP) and with the pupil shift in between each pupil tracking measurement (PS) on x axis and y axis. ρ stands for the radial position.

Figure 5.35: Subject 3: the AOPTL1 loop.

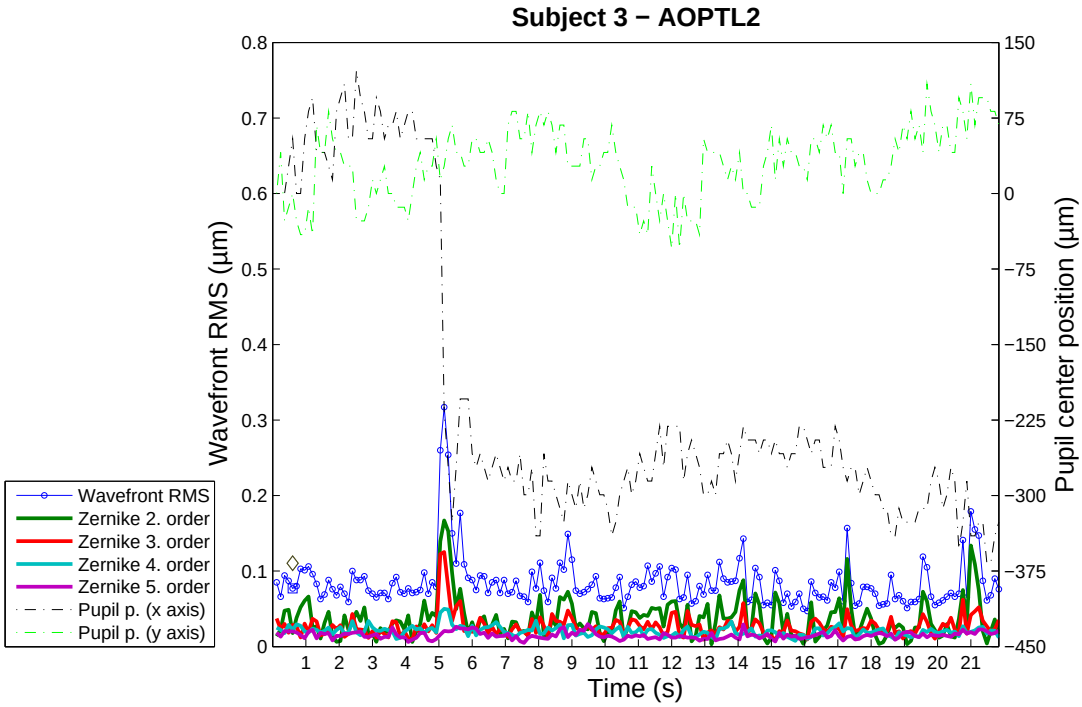

(top) Loop which incorporates the wavefront sensor, the deformable mirror, the pupil tracker and the control algorithms based on wavefront sensing and pupil tracking (AOPTL2)

AOPTL2 - Mean (μm)

RMS	PS	NA	PD	NL
0.08 ± 0.03	32 ± 26	290×70 μm^2	6000 ± 300	330 ± 17 $(lenslets)$

(middle) Mean wavefront RMS (RMS), mean pupil shift in between two pupil tracking measurements (PS), dimensions of the area in which the eye normally was (NA) ($2\sigma_x \times 2\sigma_y$), mean pupil diameter (PD), and mean number of lenslets that were used during the measurement (NL).

AOPTL2- Correlation of the WF RMS with

PP (x axis)	PP (y axis)	PP (ρ)	PS (x axis)	PS (y axis)	PS (ρ)
0	0.03	-0.03	0.47	0.13	0.47

(bottom) Correlation of the measured wavefront RMS with the measured pupil position (PP) and with the pupil shift in between each pupil tracking measurement (PS) on x axis and y axis. ρ stands for the radial position.

Figure 5.36: Subject 3: the AOPTL2 loop.

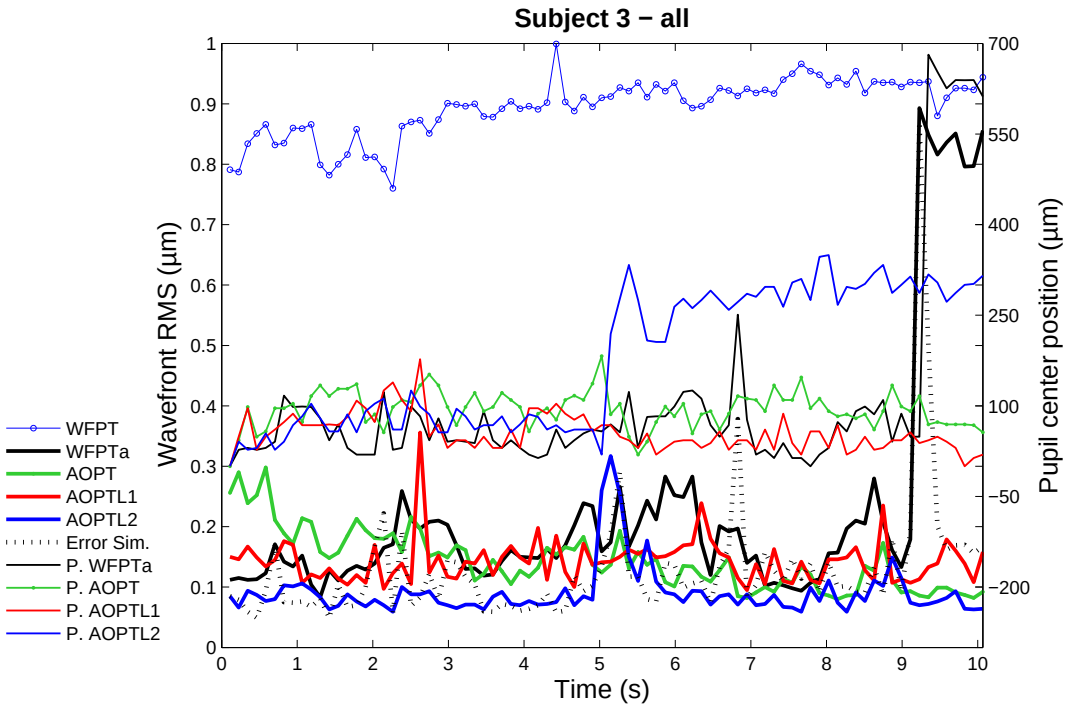

(top) Wavefront RMS of the WFPT, AOPT, WFPTa, AOPTL1 and AOPTL2 experiments and the residual error of the simulations and their respective pupil positions shown with the same color (P).

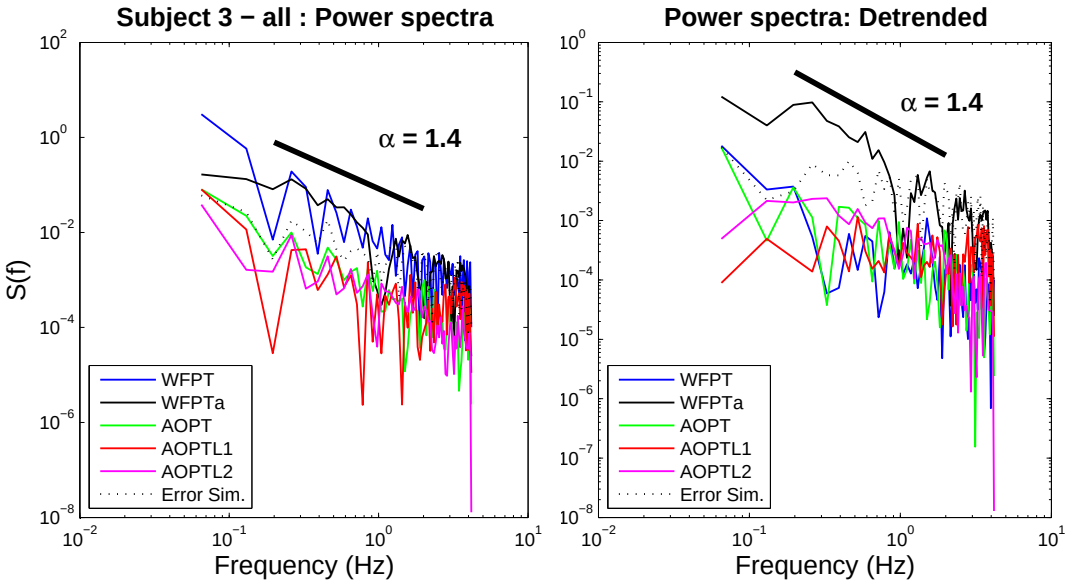

(bottom) Power spectra of the RMS of all the measurements and the residual error wavefront of the simulations (left). The detrended spectra (done after the mean of the each data set were subtracted) was made to compare the fluctuations of the signals.

Figure 5.37: Subject 3: summary of the experiments.

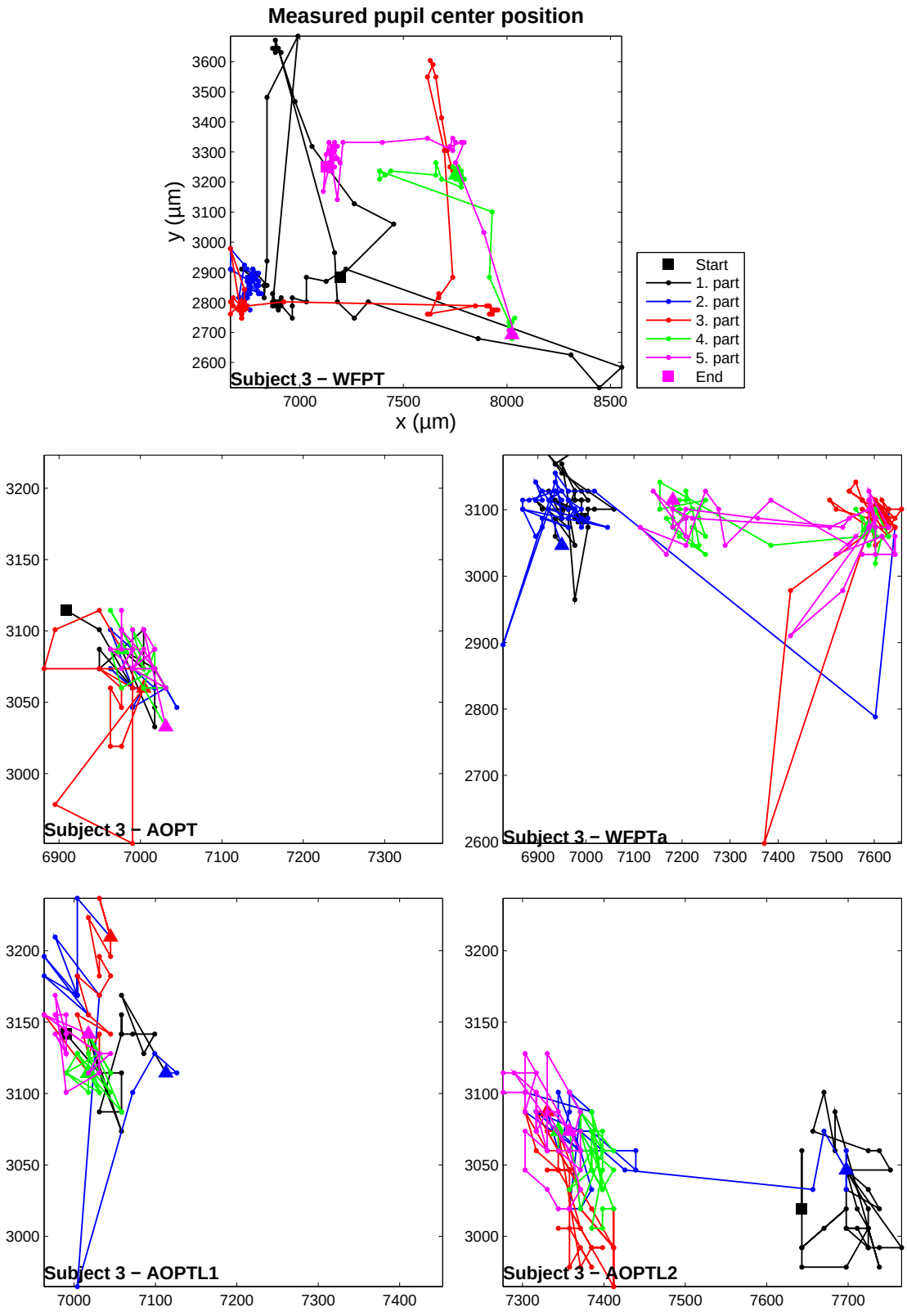

Figure 5.38: Pupil positions recorded during each experiment. The axes of the plots are not scaled to a specific value. For visual clarity the data was divided into five parts, colored differently and beginning and the end of the data were indicated by square markers.

5.4 Summary and discussion

Measurements of the wavefront aberrations and pupil positions, corrections of the aberrations with open and closed loops based on wavefront sensing and pupil tracking were performed with a moving model eye and *in vivo* on three subjects. A summary of all the data acquired is given in Table 5.1.

The model eye had the advantage of its aberration changes being solely dependent on pupil movements. It had no other intrinsic parameters that changed and caused high order aberration changes therefore we expected that it served as the gold standard for the evaluation of the method. However it had an important spherical aberration which none of the real eye aberrations had and a large pupil diameter. The correlation plot of the measurements and the simulations of the open WFPTa[36] loop was elliptical revealing a time lag. The time lag was probably due to the fact that the pupil tracker and wavefront sensor started exposure at the same time while the former had a 10 ms and latter had a 30 ms exposure time. The remaining 20 ms was the factor that pupil tracker followed the eye movements behind. The solution to this problem can be to start the pupil tracking camera exposure 10-15 ms later than the exposure of the wavefront sensing camera. The 7 mm pupil of the model eye moving in front of the 6 mm pupil of the system might have introduced some other aberrations as it continued to full the systems pupil although it was shifted.

The WFPTa measurements and the simulations of the Subject 2 demonstrated how the aberration profile of the subject changed at the middle of the measurement and effected the outcome of the estimation done with the control algorithm based on pupil tracking. The estimation was not good at the beginning of the measurement but after a blink the estimation became relevant. It is worth underlining that the estimation depends highly on the selection of a good reference wavefront that will represent the aberrations of the eye on axis and this becomes

[36]Loop which incorporates the wavefront sensor, the pupil tracker and the deformable mirror that corrects the aberrations statically (WFPTa)

Model Eye	RMS	PS	NA	NL	PD
WFPT	0.67 ± 0.02	32 ± 17	250×40 μm^2	437 ± 1	7072 ± 0
AOPT	0.08 ± 0.04	30 ± 22	170×40 μm^2	438 ± 1	7072 ± 0
WFPTa	0.14 ± 0.08	23 ± 16	180×40 μm^2	438 ± 1	7072 ± 0
WFPTa Sim	0.1 ± 0.06				
WFPTa Err	0.07 ± 0.03				
AOPTL1	0.1 ± 0.02	30 ± 19	230×40 μm^2	438 ± 1	7072 ± 0
AOPTL2	0.07 ± 0.02	26 ± 15	230×40 μm^2	438 ± 1	7072 ± 0
Subject 1	RMS	PS	NA	NL	PD
WFPT	2.16 ± 0.11	51 ± 57	330×160 μm^2	405 ± 9	6800 ± 300
AOPT	0.12 ± 0.05	51 ± 67	280×200 μm^2	417 ± 5	6800 ± 90
WFPTa	0.39 ± 0.09	67 ± 72	250×210 μm^2	396 ± 12	6300 ± 200
WFPTa Sim	0.35 ± 0.10				
WFPTa Err	0.21 ± 0.07				
AOPTL1	0.21 ± 0.08	66 ± 92	310×80 μm^2	416 ± 5	7000 ± 200
Subject 2	RMS	PS	NA	NL	PD
WFPT	0.67 ± 0.03	52 ± 43	200×160 μm^2	408 ± 14	6300 ± 100
AOPT	0.09 ± 0.01	79 ± 73	100×470 μm^2	401 ± 7	6900 ± 60
WFPTa	0.20 ± 0.05	68 ± 70	220×120 μm^2	396 ± 10	6430 ± 90
WFPTa Sim	0.20 ± 0.05				
WFPTa Err	0.19 ± 0.03				
AOPTL1	0.14 ± 0.04	34 ± 31	160×110 μm^2	389 ± 3	7030 ± 60
AOPTL2	0.10 ± 0.06	50 ± 65	260×180 μm^2	395 ± 8	7000 ± 100
Subject 3	RMS	PS	NA	NL	PD
WFPT	0.94 ± 0.06	77 ± 153	940×520 μm^2	361 ± 33	6300 ± 100
AOPT	0.14 ± 0.05	33 ± 26	60×60 μm^2	394 ± 7	6500 ± 60
WFPTa	0.47 ± 0.29	54 ± 78	580×110 μm^2	357 ± 19	6300 ± 300
WFPTa Sim	0.47 ± 0.30				
WFPTa Err	0.16 ± 0.09				
AOPTL1	0.14 ± 0.04	34 ± 31	70×80 μm^2	389 ± 3	6500 ± 40
AOPTL2	0.08 ± 0.03	32 ± 26	290×70 μm^2	330 ± 17	6000 ± 300

Table 5.1: Summary of all the measurements where; PS means pupil shift at each loop; NA is the dimensions of the area in which the eye normally was ($2\sigma_x \times 2\sigma_y$); NL means number of lenslets that was used for wavefront sensor measurements; PD means diameter of the pupil of the subject during the measurements; WFPTa Sim means the RMS of the simulated wavefront, WFPTa Err means the RMS of the residual wavefront error of the simulations. ***All the units are in micrometers, except the NA and NL which were in μm^2 and lenslets respectively.***

harder during the *in vivo* measurements. An automated selection of the reference wavefronts based on the quality of the measurements, *i.e.* number of active lenslets and the pupil position would increase the success of the correction done with control algorithm based on pupil tracking.

Measurements done with Subject 3 showed a case where the AOPT[37] correction quality was below the average. In the simulations of the WFPTa[38] loop one of the error sources was that at certain instants of measurements the displacements of the pupil did not affect the measured wavefront RMS. These changes in pupil position that appeared like spikes in the graph took place in a short time where the pupil came back to its original position shortly. The movement of the pupil might have been unnoticed and only contributed to the noise of the wavefront sensor measurement if it happened within the long 30 ms exposure time of the wavefront sensor camera although it might have been caught in the 10 ms exposure time of the pupil camera. The solution to this problem could be to use multiple pupil tracking measurements with a fast pupil tracker and improve the algorithm to ignore the round trip pupil shifts if they took place in the exposure time of the wavefront sensor camera. By this way the aberrations estimated by the algorithm based on pupil tracking would not take into account such pupil trips and create an estimation error in the AOPTL2[39] loop.

We also looked at the power spectra of all the experiments to see the results in terms of amplitude fluctuations if the control algorithm pupil tracking was able to further enhance the adaptive optics correction. Generally the AOPT provided the best correction with lowest fluctuations but we observed that all the spectra had a $1/f^{\alpha}$ like trend α being $\sim 1.5 \pm 0.1$. Having acquired enough evidence that most of the aberration changes of the eye with respect to the wavefront sensor are due to eye movements, it was straightforward to guess that the spectra of the eye

[37]Loop which incorporates the wavefront sensor, the deformable mirror, the pupil tracker and the control algorithm based on wavefront sensing (AOPT)

[38]Loop which incorporates the wavefront sensor, the pupil tracker and the deformable mirror that corrects the aberrations statically (WFPTa)

[39]Loop which incorporates the wavefront sensor, the deformable mirror, the pupil tracker and the control algorithms based on wavefront sensing and pupil tracking (AOPTL2)

movements which have not been addressed yet would have a similar trend. Several separate wavefront measurements of a fourth subject were summed up to have a longer data set. The spectra of the measured wavefront RMS and pupil position and diameter was shown in Figure 5.39 - left.

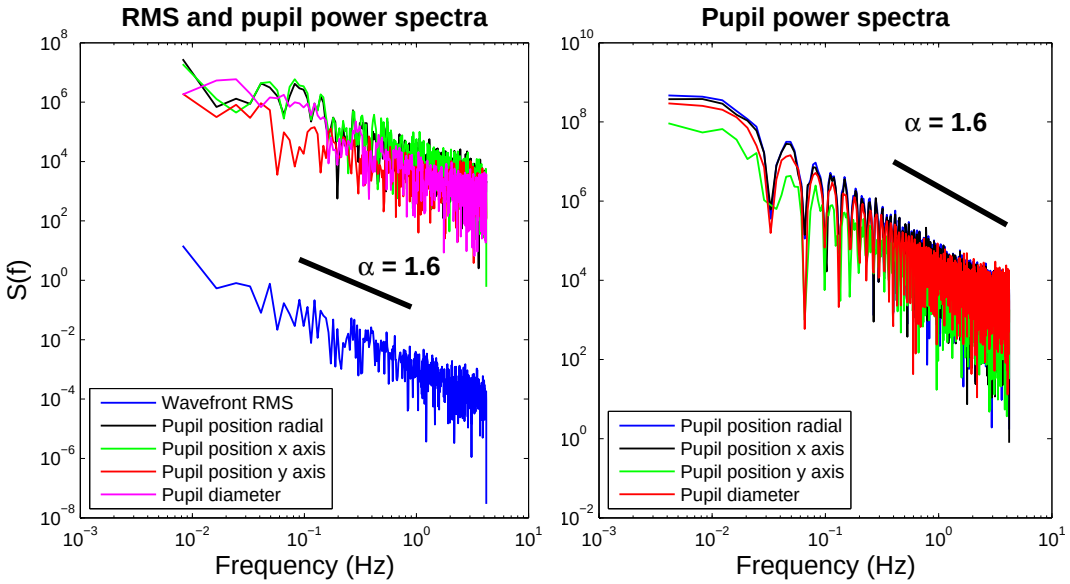

Figure 5.39: Power spectra calculated after different WFPT and pupil tracking recordings were summed up for longer data. 585 data points (70 s) of WFPT loop with pupil tracking (detrended)(left) and 1794 data points (214 s) of pupil tracking only (right).

Similarly, separate pupil tracking measurements of the same subject was added up to acquire a single longer data set, see the spectra in Figure 5.39 - right. All the spectra including the pupil diameter showed a similar trend of $\alpha \sim 1.6$. A similar trend, decrease of approximately 4dB per octave by frequency was observed by several authors [52, 114, 46, 50]. The value of α may be indicative of the health and disease and the implication of this to these data set shall be discussed in the conclusions chapter.

Table 5.2 shows the experiments done at 20 Hz, to explore if the correction with AOPT, the simulations of WFPTa or AOPTL1[40] loop could be better at this rate. The pupil tracking and wavefront sensing takes 50 ms approximately to measure so the fastest loop that can be run had 20 Hz frame rate. AOPTL2 could

[40]Loop which incorporates the wavefront sensor, the deformable mirror, the pupil tracker and the control algorithm based on pupil tracking (AOPTL1)

not be tried as it requires two pupil tracking measurements.

Subject 2f	RMS	PS	NA	NL	PD
WFPT	0.71 ± 0.03	26 ± 22	110×60 μm^2	378 ± 5	6600 ± 70
AOPT	0.11 ± 0.10	20 ± 16	50×60 μm^2	408 ± 8	7000 ± 30
WFPTa	0.16 ± 0.03	32 ± 38	220×160 μm^2	402 ± 5	6600 ± 100
WFPTa Sim	0.13 ± 0.03				
WFPTa Err	0.14 ± 0.03				
AOPTL1	0.12 ± 0.03	36 ± 34	240×140 μm^2	408 ± 2	6900 ± 50

Subject 4f	RMS	PS	NA	NL	PD
WFPT	0.60 ± 0.03	46 ± 65	710×180 μm^2	402 ± 8	7800 ± 40
AOPT	0.09 ± 0.05	31 ± 32	750×170 μm^2	386 ± 18	7880 ± 80
WFPTa	0.09 ± 0.05	27 ± 33	140×80 μm^2	397 ± 8	7700 ± 50
WFPTa Sim	0.09 ± 0.03				
WFPTa Err	0.09 ± 0.04				
AOPTL1	0.08 ± 0.02	34 ± 32	180×30 μm^2	404 ± 4	7400 ± 90

Table 5.2: Summary of the measurements made at 20 Hz; PS means pupil shift at each loop; NA is the dimensions of the area in which the eye normally was ($2\sigma_x \times 2\sigma_y$); NL means number of lenslets that was used for wavefront sensor measurements; PD means diameter of the pupil of the subject during the measurements; WFPTa Sim means the RMS of the simulated wavefront, WFPTa Err means the RMS of the residual wavefront error of the simulations. ***All the units are in micrometers, except the NA and NL which were in μm^2 and lenslets respectively.***

In conclusion the adaptive optics control algorithm based on pupil tracking was successful in correction of the aberrations of a moving model eye and *in vivo*. In spite of the long exposure times the pupil tracking was able to follow and help compensate for eye movements. At this acquisition time of pupil tracking, running faster loops provided no enhancement in the correction as tried at 20 Hz for two subjects.

Chapter 6

Conclusions and future work

Using an adaptive optics retinal camera developed for clinical research it was shown that changes of higher order aberrations of the eye including the astigmatism were highly correlated with the pupil displacements. Based on this fact it was possible to correct for the aberrations of the eye real time using a reference wavefront measurement, a pupil tracker and a deformable mirror without the real time contribution of the wavefront sensor measurements.

Alternatively, a fast pupil tracker, instead of replacing the wavefront sensor can also work in collaboration with the wavefront sensor to enhance the correction in a loop where the deformable mirror can be called more than once. Unfortunately this could not be tested due to the fact that the pupil tracker that worked at 85 Hz at continuous mode worked at 20 Hz when triggered in the retinal imaging system. Another configuration where a pupil tracker can be used in an adaptive optics loop may be to feed a scanning mirror and using it to directly correct for the displacements similar to the use of two deformable mirrors as woofer and tweeter. Also a moving phase plate (specific to the individual's ocular aberrations) and a pupil tracker can be used to upgrade an ordinary old fashioned retinal camera to an adaptive optics retinal camera with a little cost.

We observed certain times that the correction based on pupil tracking did not work and we attributed this to the tear film rupture or to a bad choice of

reference wavefront measurement. As we observed and the control algorithm that is suggested here is based on, this algorithm is best for correcting for the aberrations that have a linear relationship with the field angle. As the relationship becomes nonlinear, like the quadratic relationship of the astigmatism with the field, the error of the method increases. A selective correction of the higher order aberrations depending on their relationship with field angle and the error induced would be more efficient.

The power spectra of the recordings of the wavefront RMS and the pupil positions showed a similar $1/f^{\alpha}$ like trend where α was $\sim 1.5 \pm 0.1$. A linear relationship on a log-log graph indicates the presence of scaling (self similarity), such that fluctuations in small time scales are related to the fluctuations in larger time scales in a power law fashion [132]. 1/f noise is ubiquitous in nature: spatially extended subjects, *e.g.*, mountain landscapes, coastal lines, river branches, appear to be self similar structures [133, 134, 131, 135, 136]. Also atmospheric turbulence is a phenomenon where self similarity is believed to occur both in time and space [133].

The value of α was consistent with the previous studies [52, 114, 46, 50]. Implications of the magnitude of α of physiological data in terms of the health and disease was studied by several authors [137, 132, 138, 139]. Using power spectral analysis it was possible to differentiate between the time series of healthy hearts and hearts with severe illnesses in humans [132, 139]. A spectrum that belonged to a healthy heart would have $\alpha \approx 1$ and α would vary between 0 and 2 in the diseased states. $\alpha = 1$ is a compromise between the complete unpredictability of the white noise *i.e.*, $\alpha = 0$ and the much smoother landscape of the Brownian noise (random walk) *i.e.*, $\alpha = 2$.

There is no general theory that explains the wide spread occurrence of 1/f noise. 1/f noise (or signal) signifies that when the power spectrum of these time series is considered, each frequency has power proportional to its period of oscillation. As such, power is distributed across the entire spectrum and not concentrated at a certain portion. Consequently, fluctuations at one time scale are only loosely

correlated with those of another time scale. This relative independence of the underlying processes acting at different time scales suggests that a localized perturbation at one time scale will not necessarily alter the stability of the global system. In other words, 1/f noise renders the system more stable and more adaptive to internal and external perturbations [140]. This is exactly what is needed for a dynamical, biological system which has to provide vision at different light levels and compensate for the continuous movement and changing aberrations via stochastic[1] feedback mechanisms as proposed by Ivanov *et al.* [138].

1/f like scaling of the power spectrum characterizes the fractal behaviour (i.e., repeating self similarity of a process) of healthy free running biological system [141]. Neither our data nor the data of previous studies had spectra with $\alpha = 1$. This can be followed by a straight forward explanation: the process which the data is taken renders the eye an unhealthy state. Fixation for long times with a special effort to prevent blinking is definitely not what a healthy eye does every day. In the real life we do not stare at a point continuously because either the visual target is moving or us. This explanation can be proven right or wrong by applying the same analysis to the *eye tracking* (at least $\pm 40^\circ$ visual field) data of healthy subjects who are outdoors and whose gazes are not restricted. Also it can be argued that forcing the eye to stay in a unhealthy state for a long time might also render the healthy eye unhealthy which might explain why would people with certain occupations statically have bigger chances to develop refractive errors [88, 86].

Biological data is far more complex than being monofractal *i.e.*, having only one α value. Further studies on fractal analysis showed that actually healthy systems have α values changing by time and the range of these values being wide is also a sign of health. With the application of this relatively new technique to the biological data, the previous theory of physiological control was challenged [137]. In contrast to the previous statement, it seems healthy systems do not seek

[1] opposite of deterministic that produces the same result for a given initial condition; for a known initial condition there are many possibilities that a process may go to

to attain a constant steady state, but rather a complex variability defines a free functioning biological system [137]. This makes us feel more comfortable with the continuous chaotic movement [142] (i.e., indecomposable yet contains regularity) of the eyes.

Multifractal analysis which was applied to many physiological data such as brain, heart, gait [132, 139], was applied to ocular aberration dynamics by Hampson *et al.* [50] recently. Similar to Goldberger and Ivanov *et al.*, they performed wavelet analysis[2] to represent the temporal self similarity of the signal and wavelet based method for multifractal analysis[3] and confirmed the multifractal nature of the ocular dynamics (containing more than one process with self similarity). The wavelet analysis of ocular dynamics of the *fixating eye* showed flame like patterns similar to the wavelet analysis of the diseased heart in the study of Golberger *et al.*. Hampson *et al.* [50] argued that multifractal analysis can give an insight into subjects that may have problems with accommodation function such as progressing myopic subjects reminding that progressing myopes showed prominent low frequency fluctuations which might indicate the breakdown of the multifractal spectrum.

Dynamics of the aberrations of the eye is a very advanced and complex topic which raised interest in modelling [43] and which has to be addressed for a better understanding of the capabilities and the limits of the high resolution retinal imaging. Use of wavelet based approach to assess fractal nature in assessing ocular aberrations and retinal images may prove right in the near future because of the self repeating multifractal nature of these data.

Having a limited knowledge on the nature of the change of aberrations, developing faster adaptive optics components seems to be the closest option for further improvements in retinal imaging. For instance wavefront sensors based on complementary metal-oxide semiconductor (CMOS) technology are promising for the

[2] a wavelet when convolved, will resonate if the unknown signal contains information of similar frequency

[3] a measure of how complicated a self-similar process is

future, offering high quantum efficiency (less need for light power) and bandwidths in kilohertz with some other unique properties such as they can be read at a desired pattern although they have the handicaps of having limited size and resolution at the moment [46]. Faster components raise a need for faster and more efficient control algorithms as the standard adaptive optics algorithms based on singular value decomposition has linear computation cost: increases as the number of actuators increases. An alternative to this may be a wavelet based phase reconstruction whose time cost is not related to the number of actuators [143]. Also a more adaptable control algorithm that can predict the deformable mirror gain in real time was proposed [144].

A faster adaptive optics system may provide a better correction for the ocular aberrations as measured by the wavefront sensor but a low RMS does not assure always high resolution retinal images even with healthy eyes. To overcome the challenges of retinal imaging with all types of eyes in high resolution and develop a modality that is suitable for clinical use seems to require a dense interdisciplinary research, a better understanding of the visual processes including all the physical, chemical and the biological phenomena.

Appendix A

Specifications of the Components

Pupil Tracking System	
Light source	Osram SFH 4503LED, 950 nm, $\pm 4^o$
	Spectral bandwidth, $\Delta\lambda = 40$ nm
	Radiant Intensity, 250 mW/sr
	LED Alignment, E-Tec Dual socket strips
Image formation	Achromatic Doublet 100 mm
	Pentax C3516-M 35 mm 1:1.6
CCD	SVS Vistek - SVCam CP SVS204(Camera Link)
	Active area, 1024×768 $pixel^2$
	Active area, 3.5×4.8 mm^2
	Pixel size, 4.65×4.65 μm^2
	50 fps 10 bit monochrome signal
	Spectral response, 380-950 nm
Framegrabber	Euresys - Grablink Value PCI Express
Area imaged on the pupil plane	13.59×5.31 mm^2
Software	C++
	Execution speed, ~ 2 ms
Experiments	
Artificial Eye	Pupil diameter 7 mm
	Corneal radius, 8 mm
Motion Controller	Newport Motion Controller MM4006
	Stages, precision 0.1 μm
Time response	Motor, EBM PAPST Variodrive VD - 3 - 43.10
	Motor driver card, EBM PAPST
	Variotonic DRIVECONTROL VT - A
Ocular Safety	Newport 818-SL Photodetector Head
	Newport 2835-C Multi-Function Optical Meter

Table A.1: The materials used in the experiments.

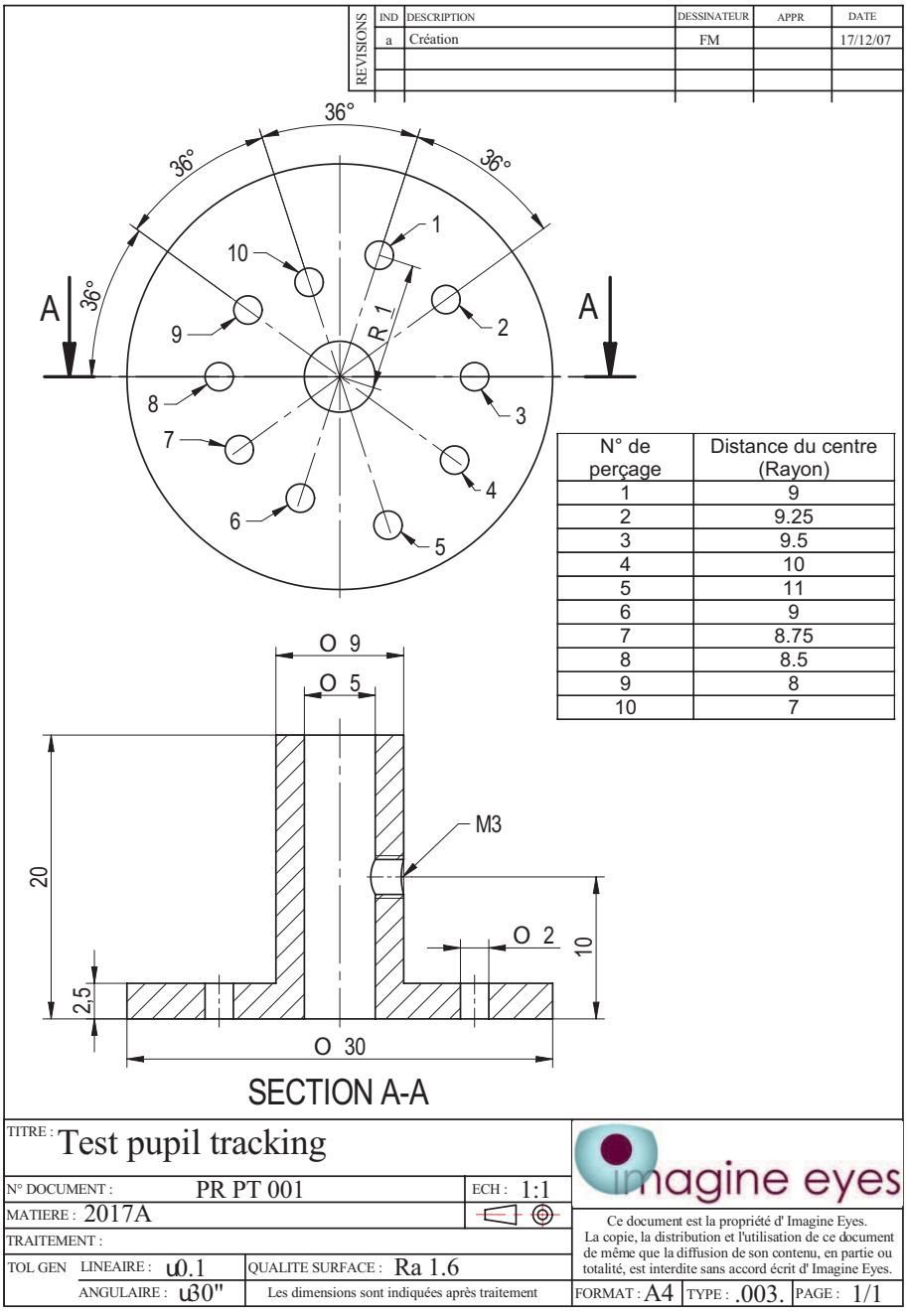

Figure A.1: Mechanical piece to attach the model eye with two screws to the motor arm at different eccentricities (Imagine Eyes, France).

Deformable Mirror	Imagine Eyes, mirao 52-e Electromagnetic deformable mirror
	52 actuators
	Max. generated wavefront peak to valley, 50 μm (tilt)
	Effective diameter, 15 mm
	Linearity, $> 95\%$
	Coating, protected silver
	Bandwidth at ~ 200 Hz.
Wavefront Sensor	Imagine Eyes, HASO 32-eye Shack-Hartmann wavefront sensor
	Aperture dimension, 4.5×3.6 mm^2
	Lenslet array, $40 \times 32 = 1280$
	Accuracy, $\sim \frac{\lambda}{100}$
	Spatial resolution, $\sim 114\mu$m
	Maximum acquisition frequency, 60 Hz
AO Control Software	Casao, Imagine Eyes
WFS Control Software	Haso, Imagine Eyes

Table A.2: Components of the adaptive optics system

Appendix B

Ocular Safety

Ocular safety measurements for the adaptive optics retinal camera were performed in compliance with the European standard for ophthalmic instruments using a broadband photodetector [123]. The retinal camera had four types of light sources; an array of ten near infrared LEDs for pupil imaging, one Super Luminescent Diode (SLD) for wavefront sensing, one Organic Light Emitting Diode (OLED) to serve as a fixation target for the subject's eye and finally one infrared LED for retinal image acquisition.

Table B.1 summarizes the parameters to be calculated according to the standard[1]. E_{IR-CL} stands for the infrared radiation irradiance on the cornea and the crystalline lens where E_λ ($\frac{W}{cm^2 \cdot nm}$) is the spectral irradiance and $\Delta\lambda$ (nm) is the bandwidth of the light source in which the summation is made. E_{VIR-R} is thermal visible and infrared radiation irradiance on the retina where $R(\lambda)$ is the spectral weighing factor whose predefined values for each wavelength were supplied by the standard[2].

Parameter	Wavelength (nm)	Equation	Limit
E_{IR-CL}	770 to 2500	$\sum_{770}^{2500} E_\lambda \cdot \Delta\lambda$	20 $\frac{mW}{cm^2}$
E_{VIR-R}	380 to 1400	$\sum_{380}^{1400} E_\lambda \cdot R(\lambda) \cdot \Delta\lambda$	0.7 $\frac{W}{cm^2}$

Table B.1: Ocular safety limits for corneal E_{IR-CL} and retinal irradiance E_{VIR-R} defined by European standard for ophthalmic devices, ISO 15004-2[123].

[1] pg. 9, Table 2[123]
[2] pg. 23, Table A.1[123]

The tests to be performed require spectral weighing of the radiation; however it is possible to use a broadband photodetector instead of a spectrometer if the spectral characteristics of the photodetector and the spectral distribution of the light sources are known[3]. The manufacturers yearly calibration report includes the responsivity curve of the powermeter in the spectral range of 400-1100 nm and all the light sources in the system are supplied with data showing their spectral distribution, see for example Figure B.1.

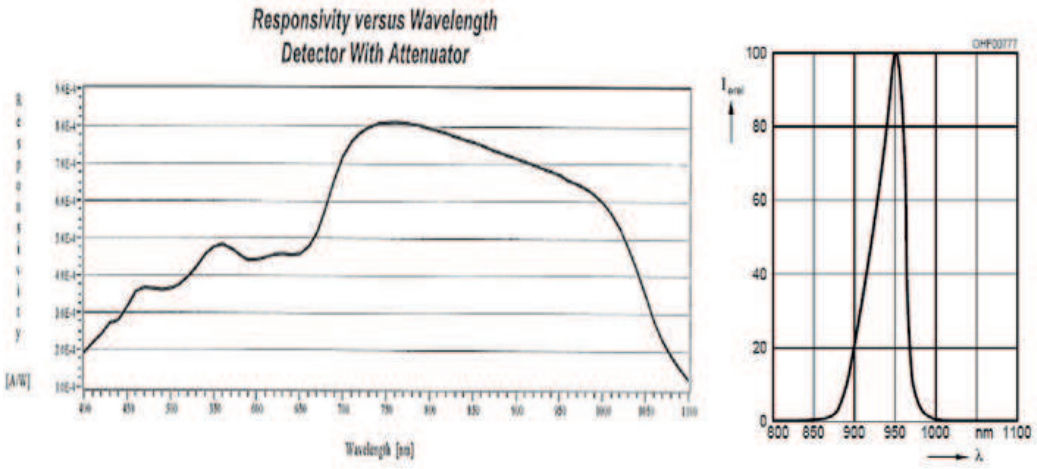

Figure B.1: Responsivity curve of the photodetector (left) and spectral distribution of the LEDs for pupil tracking (right).

The photodetector head was placed in the place of the eye using the eye camera in a similar manner to in vivo measurements. Measurements and calculations done for one LED of mean wavelength 950 nm are described as follows. To estimate E_{IR-CL}, one has to measure the power across a 1 mm diameter pupil and divide this value with the area of the surface[4]. Spectral interval of the LED was 925-965 nm full width half maximum; the maximum of the sensitivity of the photodetector within this interval was situated at 925 nm, Figure B.1 - left. Therefore the detector was adjusted to measure at this wavelength to increase the power measured and to overestimate the risk. A diaphragm of 1 mm was placed before the photodetector head and the value measured was divided by the area of the pupil of the diaphragm $A = \pi(0.5)^2 = 7.9 \times 10^{-3}\ cm^2$, see Table B.2.

[3]pg. 30, Appendix C[123]
[4]Appendix D.2 and E.1[123]

Figure B.2 shows the schematics for the experiment done to estimate E_{VIR-R}. To estimate E_{VIR-R} the power across a 7 mm pupil had to be measured and

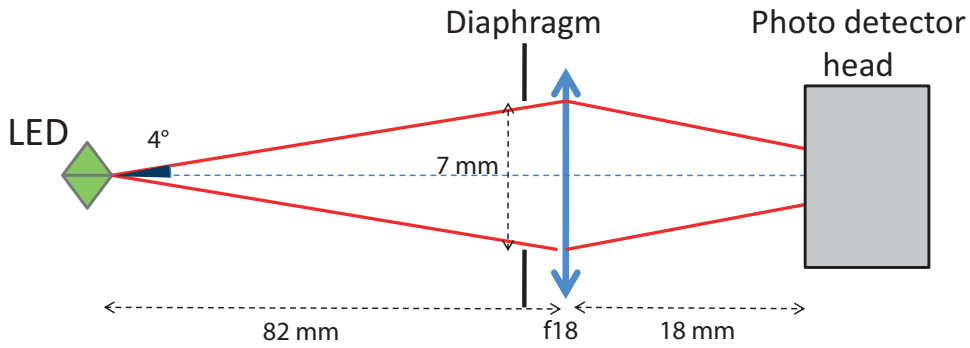

Figure B.2: Measuring the power due to one LED (mean wavelenght 950 nm) for pupil illumination on the retina. The LED array was 85 mm away from the detector; the power of only one LED was measured by covering the others.

divided by the area of surface illuminated on the retina (0.023 cm^2 maximum as defined by the standard)[5]. The measurement wavelength of the powermeter was adjusted to 925 nm where its maximum sensitivity was situated, see Figure B.1. A diaphragm of 7 mm diameter was placed in front of the photodetector and a lens (f18 mm) with a similar power to the human eye lens (f17 mm) was placed behind it to collect all the flux emerging the diaphragm on the detector surface. After the power on the detector surface was measured it was divided by the permissible circular area on the retina, as given by the standard 0.023 cm^2. Table B.2 shows the result for ten LEDs after the calculated irradiance on the retina was multiplied by the maximum weighing factor on the spectra which was 0.35 at 925 nm[6], $\frac{1}{0.023} \times 0.35 \sim 16\ \frac{mW}{cm^2}$. This is an overestimated value because illumination of the LED array is distributed over the face of the eye rather than being exactly at the same point. All the four light sources in the retinal camera were examined one by one and they were found below the safety limits, Table B.2.

Table B.2 shows the results for four sources when they were operating alone but in the adaptive optics retinal camera ten LEDs and other sources are operating all together. Total irradiances on the cornea and the retina when all the sources

[5]Appendix D.3 and E.2[123]
[6]pg. 23, Table A.[123]

Source	Parameter	Power	Irradiance	Limit	Status
(10) LED@950 nm	E_{IR-CL}	12 μW	1.52 $\frac{mW}{cm^2}$	20 $\frac{mW}{cm^2}$	OK
	E_{VIR-R}	1 mW	0.016 $\frac{W}{cm^2}$	0.7 $\frac{W}{cm^2}$	OK
LED@850 nm	E_{IR-CL}	75 μW	0.82 $\frac{mW}{cm^2}$	20 $\frac{mW}{cm^2}$	OK
	E_{VIR-R}	41 μW	0.0018 $\frac{W}{cm^2}$	0.7 $\frac{W}{cm^2}$	OK
OLED@570 nm	E_{VIR-R}	2 mW	32×10^{-6} $\frac{W}{cm^2}$	0.7 $\frac{W}{cm^2}$	OK
SLD@750 nm	E_{VIR-R}	50 μW	0.07 $\frac{W}{cm^2}$	0.7 $\frac{W}{cm^2}$	OK

Table B.2: Ocular safety measurement results for the four light sources of adaptive optics retinal camera showing the parameter to be measured, the power measured on the detector, the power per cm^2 on the specific area and the limit of the power per cm^2 of the parameter defined by the standard[123] and the safety status of the source.

of the adaptive optics retinal camera are active are calculated. According to the standard only the array of ten LEDs of 950 nm mean wavelength and the LED of of 850 nm mean wavelength contribute to the irradiance on cornea E_{IR-CL},

$$E_{IR-CL}(LED@950) + E_{IR-CL}(LED@850) \leq Limit_{E_{IR-CL}}, \tag{B.1}$$

equals to $1.52 + 0.82 = 2.4$ $\frac{mW}{cm^2}$ and is less than the limit of 20 $\frac{mW}{cm^2}$. All of the four sources take part in the thermal irradiance on the retina E_{VIR-R} and their sum,

$$\begin{aligned} E_{VIR-R}(LED@950) + E_{VIR-R}(LED@850) &+ \ldots \\ E_{VIR-R}(OLED@570) + E_{VIR-R}(SLD@750) &\leq Limit_{E_{VIR-R}}, \end{aligned}$$

equals to $0.016 + 0.0018 + 0.000032 + 0.07 = 0.09$ $\frac{W}{cm^2}$ and is less than the limit of 0.7 $\frac{W}{cm^2}$.

In conclusion both total irradiance of the pupil tracking system and the adaptive optics retinal camera for corneal and retinal hazard were found below the limits and safe for in vivo measurements.

Appendix C

The Model Eyes

There were two different model eyes that were used in the experiments. First, a model eye with spherical aberration was used in pupil tracking tests and in adaptive optics correction to replace the human eye. Its image taken by the pupil tracking camera under near infrared light resembled a human eye with 7 mm diameter, see Figure C.1.

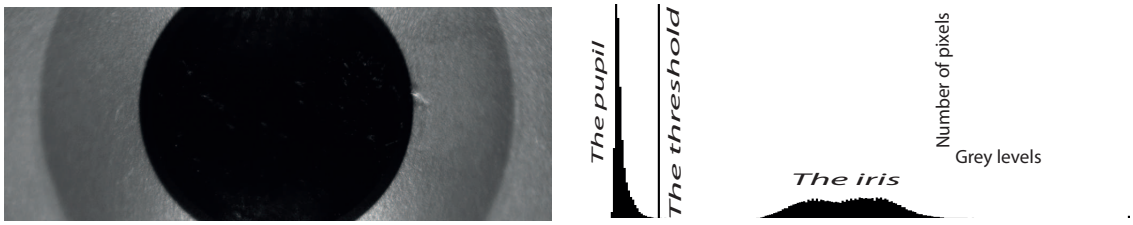

Figure C.1: An 8 bit snapshot of the model eye which had 7 mm entrance pupil (left) and its histogram of grey levels from 0 to 255 (right).

The model eye was comprised of a rod lens with a convex top, a metal cover and a diffusing surface at rear to serve as retina, Figure C.2. The dimensions of the rod lens was 8.50×22 mm and the radius of curvature of the convex top was 8 mm.

As the light streak the retina, it was diffused by the material and its reflection acted like a point source on the retina to which the convex surface introduced the spherical aberration. Nevertheless because it was impossible to align the eye with the system perfectly, the tilted model resulted in more aberration terms,

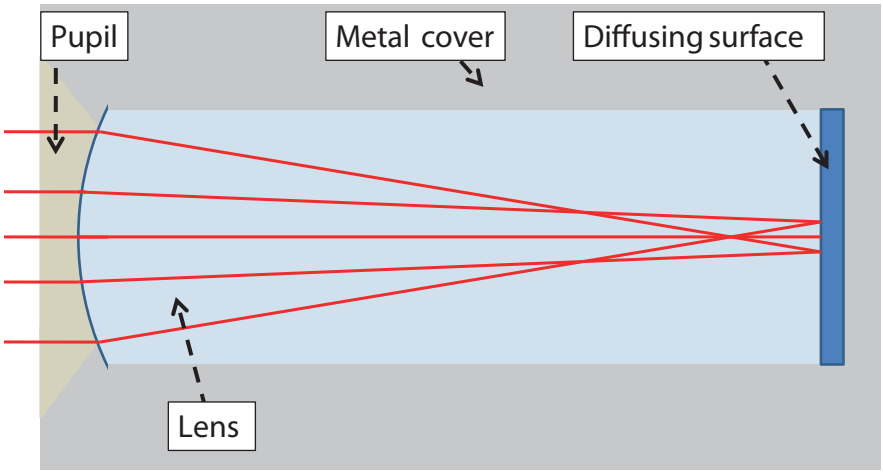

Figure C.2: The model eye was a rod lens that produced spherical aberration (the aberration was exaggerated in the figure).

especially astigmatism and coma whose magnitude might change depending on the alignment.

The second model eye used in the experiments was a model eye that theoretically had no aberrations. It was comprised of a lens, an alignment hole and a diffusing surface behind it that was attached to a motor arm, Figure C.3 and C.4.

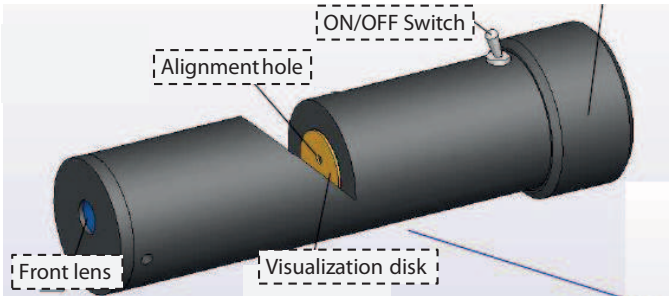

Figure C.3: An image of the model as it is commercialized with the name Modo, courtesy of Imagine Eyes.

The incoming light beam was focused by the lens at the entrance pupil to the plane of diffusing surface. The user aligned the model eye by observing the reflection of the incoming beam from the visualization disk and moving the eye until finding the position at which the beam passes through the alignment hole C.4.

The beam that stroke the diffusing surface acted like a point source and the

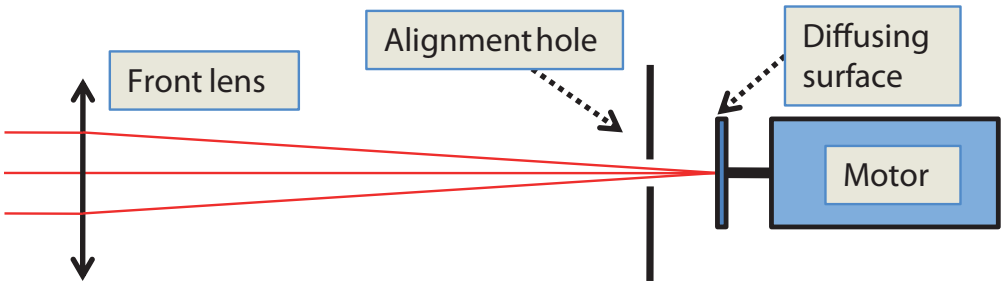

Figure C.4: The schematics of the model eye with no aberrations.

small diameter of the focusing lens and the alignment hole ensured that the beam emerging the eye was free from aberrations. If the diffuser was kept still the CCD of the wavefront sensor displayed interference patterns, see Figure C.5 (left). The spot diagram was clearer when the motor was running, Figure C.5 (right).

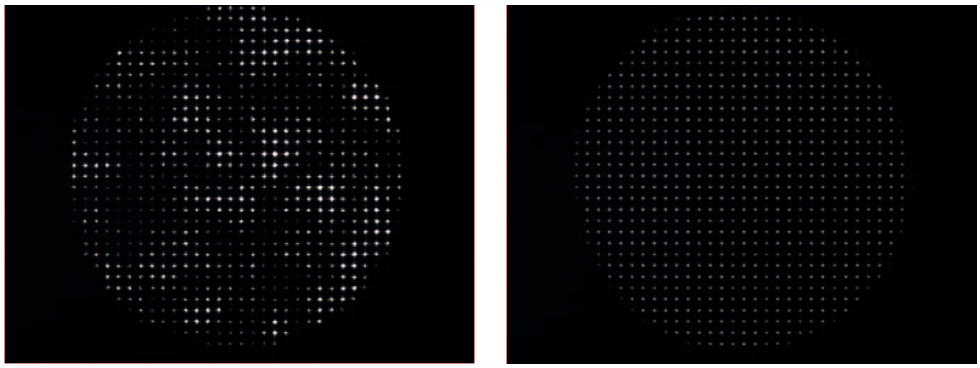

Figure C.5: The spot diagram of the plane wavefront of the model eye when the diffuser is still (left) and when it is rotated by the motor(right).

Appendix D

Computer programs

The computer programs developed to simulate, test and calibrate the control algorithm based on pupil tracking were described step by step in Tables D.1 and D.2.

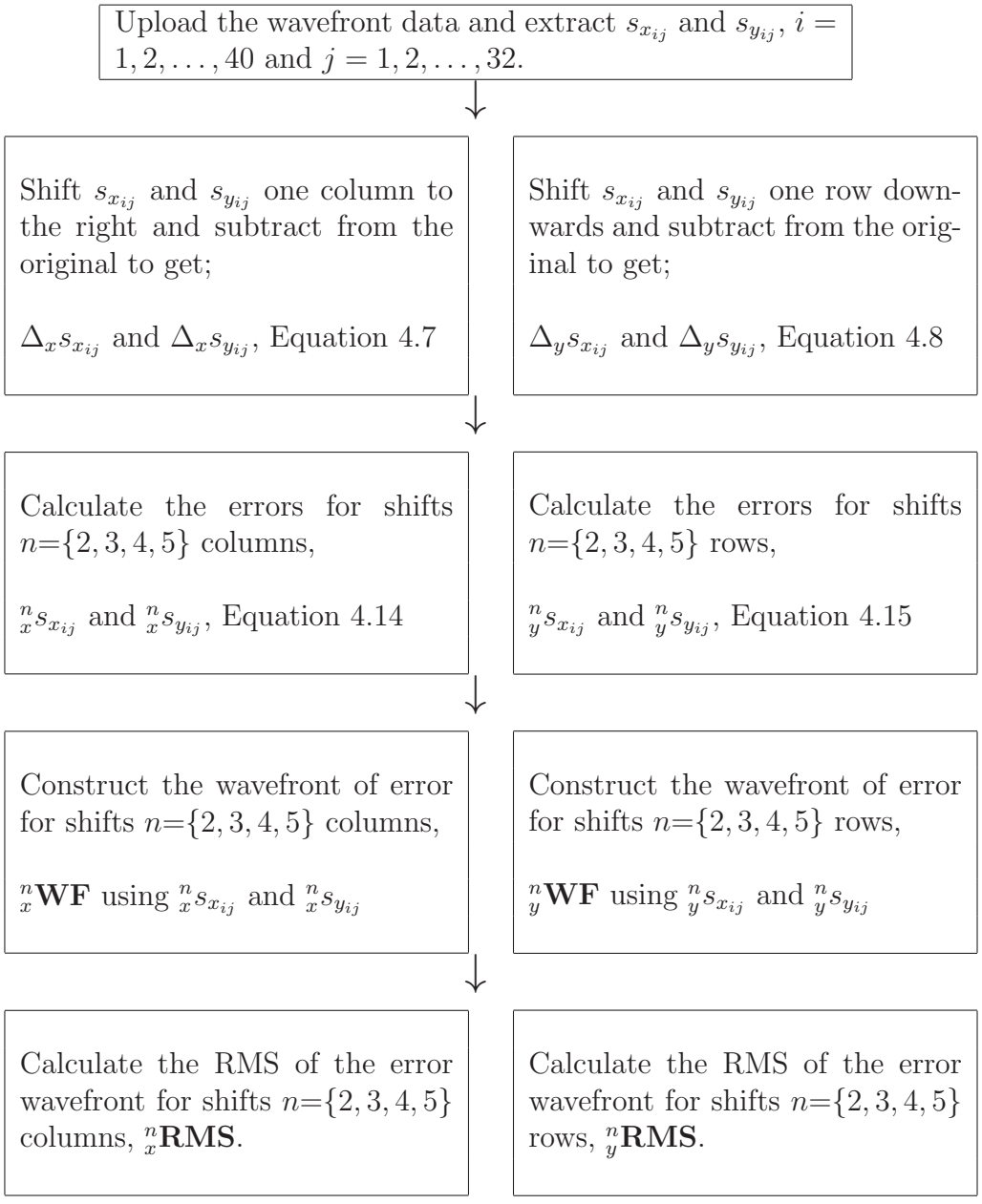

Table D.1: The algorithm to simulate the error related to the adaptive optics control algorithm based pupil tracing using real eye measurements.

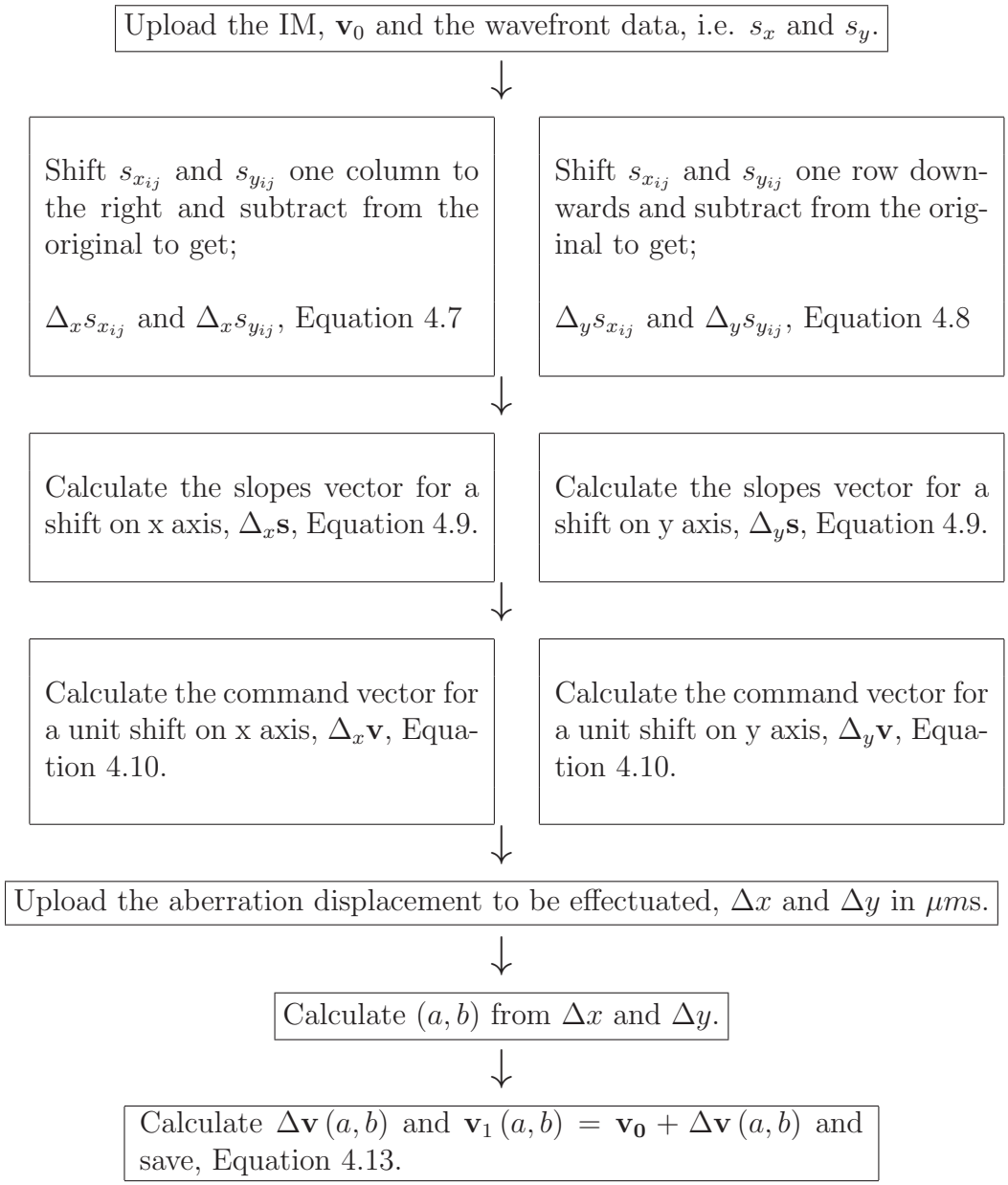

Table D.2: The algorithm for the preliminary experiments done using the retinal camera with Casao and the model eye.

Bibliography

[1] E. A. Boettner and J. R. Wolter. Transmission of the ocular media. *Invest. Ophthal.*, 1(6):776–783, 1962.

[2] N. J. Wade. Image, eye, and retina (invited review). *J. Opt. Soc. Am. A*, 24(5):1229–1249, 2007.

[3] K Grieve and A Roorda. Intrinsic signals from human cone photoreceptors. *Inves. Ophthal. Vis. Sci.*, 49(2):713–719, 2008.

[4] P. Godara, A. M. Dubis, A. Roorda, et al. Adaptive optics retinal imaging: Emerging clinical applications. *Optometry and Vision Science*, 87(12):930–941, 2010.

[5] H. Kolb, E. Fernandez, and R. Nelson. Simple Anatomy of the Retina. http://webvision.med.utah.edu/sretina.htmll, 2003. (Last accessed 12 December 2010).

[6] J Porter and H M Queener. *Adaptive optics for vision science: Principles, practices, design and applications*. Wiley-Interscience, 2006. ISBN: 0471679410.

[7] J. Keller. Adaptive optics blends the best of electronic and optoelectronic technologies. www.militaryaerospace.com, 2004. (Last accessed 19 Juin 2011).

[8] M. Hart. Recent advances in astronomical adaptive optics. *Applied Optics*, 49(16):D17–D29, 2010.

[9] N. Doble, S. S. Choi, et al. In vivo imaging of the human rod photoreceptor mosaic. *Optics Letters*, 36(1):31–33, 2011.

[10] M. Mujat, R. D. Ferguson, et al. Compact adaptive optics line scanning ophthalmoscope. *Optics Express*, 17(12):10242–10258, 2009.

[11] V. Lakshminarayanan. The human eye: A model system for teaching optics. In *Proc. The Education and Training in Optics and Photonics Conference*, 2009.

[12] F. W. Campbell and D. G. Green. Optical and retinal factors affecting visual resolution. *J. Physiol.*, 181:576–593, 1965.

[13] T. O. Salmon and L. N. Thibos. Videokeratoscope line–of–sight misalignment and its effect on measurements of corneal and internal ocular aberrations. *J. Opt. Soc. Am. A*, 19(4):657–669, 2002.

[14] J. Liang and D. R. Williams. Aberrations and retinal image quality of the normal human eye. *J. Opt. Soc. Am. A*, 14(11):2873–2885, 1997.

[15] W. T. Welford. *Aberrations of optical systems*. Taylor and Francis, 1986. ISBN: 0852745648.

[16] R. J. Noll. Zernike polynomials and atmospheric turbulence. *J. Opt. Soc. Am.*, 66(3):207–211, 1976.

[17] V. Lakshminarayanan and A. Fleck. Zernike polynomials: a guide. *Journal of Modern Optics*, 58(7):545–561, 2011.

[18] G. M. Dai. *Wavefront optics for vision correction*. SPIE, 2008. ISBN: 9780819469663.

[19] L. Thibos, R. A. Applegate, J. T. Schwiegerling, and R. Webb. Standards for reporting the optical aberrations of eyes. In *Proc. Vision Science and its Applications*, 2000.

[20] M. K. Smolek and S. D. Klyce. Zernike polynomial fitting fails to represent all visually significant corneal aberrations. *Inves. Opht. and Visual Science*, 44(11):4676–4681, 2003.

[21] M. Zhu, M. Collins, and D. R. Iskander. Microfluctuations of wavefront aberrations of the eye. *Ophthal. Physiol. Opt.*, 24:562571, 2004.

[22] T. O. Salmon and C. Pol. Normal–eye Zernike coefficients and root–mean–square wavefront errors. *Journal of Cataract and Refractive Surgery*, 32(12):2064–2074, 2006.

[23] J. F. Castejon-Mochon, N. L. Gil, A. Benito, et al. Ocular wave–front aberration statistics in a normal young population. *Vision Research*, 42:1611–1617, 2002.

[24] L. N. Thibos, X. Hong, A. Bradley, et al. Statistical variation of aberration structure and image quality in a normal population of healthy eyes. *J. Opt. Soc. Am. A*, 19(12):2329–2348, 2002.

[25] E. C. Campbell. Matrix method to find a new set of Zernike coefficients from an original set when the aperture radius is changed. *Journal of Optical Society of America*, 20(2):209–217, 2003.

[26] P. Artal, A. Benito, and J. Tabernero. The human eye is an example of robust optical design. *Journal of Vision*, 6:1–7, 2006.

[27] A. Cervino, S. L. Hosking, T. Ferrer-Blasco, et al. A pilot study on the differences in wavefront aberrations between two ethnic groups of young generally myopic subjects. *Ophthal. Physiol. Opt.*, 28:532–537, 2008.

[28] N. Maeda, T. Fujikado, T. Kuroda, et al. Wavefront aberrations measured with Hartmann–Shack sensor in patients with keratoconus. *Ophthalmology*, 109:1996–2003, 2002.

[29] J. Tabernero, A. Benito, E. Alcon, et al. Mechanism of compensation of aberrations in the human eye. *J. Opt. Soc. Am. A*, 24(10):3274–3283, 2007.

[30] P. Artal and J. Tabernero. Optics of human eye: 400 years of exploration from Galileos time. *Applied Optics*, 49(16):D123–D130, 2010.

[31] P. Prieto, F. Vargas-Martin, et al. Analysis of the performance of the Hartmann-Shack sensor in the human eye. *J. Opt. Soc. Am. A*, 17(8):1388–1398, 2000.

[32] F. W. Campbell and R. W. Gubish. Optical quality of the human eye. *J. Physiol.*, 186:558–578, 1966.

[33] P. Bedggood, M. Daaboul, et al. Characteristics of the human isoplanatic patch and implications for adaptive optics retinal imaging. *Journal of Biomedical Optics*, 13(2):024008(1–7), 2008.

[34] J. Tarrant and A. Roorda. The extent of the isoplanatic patch of the human eye. http://wildsoetlab.berkeley.edu/images/9/90/, 2006. Last accessed on 20 June 2011.

[35] E. M. Maida, K. Venkateswaran, J. Marsack, et al. What is the size of the isoplanatic patch in the human eye? http://cfao.ucolick.org/EO/internships/mainland/posters/erika.pdf. Last accessed 7 February 2011.

[36] A. Roorda. *Encyclopedia of imaging science and technology*, chapter Human visual system, pages 539–557. Wiley and Sons, 2002. ISBN: 0-471-33276-3. Accessed at http://vision.berkeley.edu/roordalab.

[37] J. M. Wanek, M. Mori, and M. Shahidi. Effect of aberrations and scatter on image resolution assessed by adaptive optics retinal section imaging. *J. Opt. Soc. Am. A*, 24(5):1296–1304, 2007.

[38] P. Artal, S. Manzanera, et al. Visual effect of the combined correction of spherical and longitudinal chromatic aberrations. *Optics Express*, 18(2):1637–1648, 2010.

[39] W. N. Charman and N. Chateau. The prospects for super–acuity: limits to visual performance after correction of monochromatic ocular aberration. *Ophthal. Physiol. Opt.*, 23:479–493, 2003.

[40] M. Zhu, M. Collins, and D. R. Iskander. Microfluctuations of wavefront aberrations of the eye. *Ophthal. Physiol. Opt.*, 24:562–571, 2004.

[41] P. E. King-Smith, B. A. Fink, J. J. Nichols, K. K. Nichols, et al. The contribution of lipid layer movement to thin film thinning and breakup. *Investigative Ophthalmology and Visual Science*, 50(6):2747–2756, 2009.

[42] M. Zhu, M. J. Collins, and D. R. Iskander. The contribution of accommodation and the ocular surface to the microfluctuations of wavefront aberrations of the eye. *Ophthal. Physiol. Opt.*, 26:439–446, 2006.

[43] C. Leahy and C. Dainty. A non–stationary model for simulating the dynamics of ocular aberrations. *Optics Express*, 18(20):21386–21396, 2010.

[44] R. Navarro. Monochromatic aberrations and point–spread functions of the human eye across the visual field. *J. Opt. Soc. Am. A*, 15(9):2522–2529, 1998.

[45] P. Prado, J. Arines, et al. Changes of ocular aberrations with gaze. *Ophthal. Physiol. Opt.*, 29:264–271, 2009.

[46] T. Nirmaier, G. Pudasaini, and J. Bille. Very fast wave–front measurements at the human eye with a custom CMOS–based Hartmann–Shack sensor. *Optics Express*, 11(21):2704–2716, 2003.

[47] N. Collins, M. alKalbani, G. Boyle, et al. Characterisation of the tremor component of fixational eye movements. In *14th European Conference on Eye Movements*, 2007. Abstract only. Last accessed on 21 June 2011 at http://www.jemr.org/online/1/s1.

[48] D. R. Iskander, M. J. Collins, et al. Analyzing the dynamic wavefront aberrations in the human eye. *IEEE Trans. Biomed. Eng.*, 51(11):1969–1980, 2004.

[49] K. Hampson, E. Mallen, and C. Dainty. Coherence function analysis of the higher–order aberrations of the human eye. *Optics Letters*, 31(2):184–186, 2006.

[50] K. M. Hampson and E. H. Mallen. Multifractal nature of ocular aberration dynamics of the human eye. *Biomedical Optics Express*, 2(3):464–477, 2011.

[51] J. Liang, D. R. Williams, and D. T. Miller. Supernormal vision and high–resolution retinal imaging through adaptive optics. *J. Opt. Soc. Am. A*, 14(11):2884–2892, 1997.

[52] H. Hofer, P. Artal, and B. Singer others. Dynamics of the eye's wave aberration. *J. Opt. Soc. Am A*, 18(3):497–506, 2001.

[53] E. J. Fernandez, I. Iglesias, and P. Artal. Closed–loop adaptive optics in the human eye. *Optics Letters*, 26(10):746–748, 2001.

[54] M. Glanc, E. Gendron, et al. Towards wide–field retinal imaging with adaptive optics. *Optics Communications*, 230:225–238, 2004.

[55] D. R. Neal, D. M. Topa, and J. Copland. Effect of lenslet resolution on the accuracy of ocular wavefront measurements. In *Proc. SPIE*, volume 4245, 2001.

[56] E. Moreno-Barriuso, S. Marcs, R. Navarro, et al. Comparing laser ray tracing, the spatially resolved refractometer, and the Hartmann–Shack sensor to measure the ocular wave aberration. *Optometry and Vision Science*, 78(3):152156, 2001.

[57] D. Debarre, E. J. Botcherby, et al. Image–based adaptive optics for two–photon microscopy. *Optics Letters*, 34(16):2495–2497, 2009.

[58] E. Grisan, F. Frassetto, V. de Deppo, et al. No wavefront sensor adaptive optics system for compensation of primary aberrations by software analysis of a point source image. 1. methods. *Applied Optics*, 46(25):6434–6441, 2007.

[59] B. Wang and M. J. Booth. Optimum deformable mirror modes for sensorless adaptive optics. *Optics Communications*, 282:4467–4474, 2009.

[60] H. Song, R. Fraanje, G. Shitter, et al. Model–based aberration correction in a closed–loop wavefront–sensor–less adaptive optics system. *Optics Express*, 18(23):24070–24084, 2010.

[61] J. W. Hardy. *Adaptive optics for astronomical telescopes*. Oxford University Press, 1998. ISBN:0195090195.

[62] E. J. Fernandez and P. Artal. Membrane deformable mirror for adaptive optics: performance limits in visual optics. *Optics Express*, 11(9):1056–1069, 2003.

[63] E. J. Fernandez, P. M. Prieto, and P. Artal. Wave–aberration control with a liquid crystal on silicon (LCOS) spatial phase modulator. *Optics Express*, 17(13):11013–11025, 2009.

[64] F. Harms, N. Chateau, et al. A new generation deformable mirror for ocular adaptive optics. In *Engineering the Eye II: Imaging the Retina*, 2006. Abstract only.

[65] R. D. Ferguson, Z. Zhong, et al. Adaptive optics scanning laser ophthalmoscope with integrated wide–field retinal imaging and tracking. *J. Opt. Soc. Am. A*, 27(11):A265–A277, 2010.

[66] R. Navarro, E. Moreno-Barriuso, et al. Phase plates for wave–aberration compensation in the human eye. *Optics Letters*, 25(4):236–238, 2000.

[67] D. Brousseau, E. Borra, et al. A new ferrofluid mirror for vision science applications. In *Frontiers in Optics*, 2009. Abstract only.

[68] J. Parent, E. F. Borra, D. Brousseau, et al. Dynamic response of ferrofluidic deformable mirrors. *Applied Optics*, 48(1):1–6, 2009.

[69] J. Girkin. Adaptive optics in deep optical sectioning microscopy of biological samples. In *Latin America Optics and Photonics Conference*, 2010. Abstract only.

[70] M. Jiang, X. Zhang, C. A. Puliafito, et al. Adaptive optics photoacoustic microscopy. *Optics Express*, 18(21):21770–21776, 2010.

[71] J. J. Hunter, B. Masella, et al. Images of photoreceptors in living primate eyes using adaptive optics two–photon ophthalmoscopy. *Biomedical Optics Express*, 2(1):139–148, 2011.

[72] F. Lacombe, M. Glanc, D. Lafaille, et al. Blood flow in retinal micro vessels. In *Invest Ophthalmol Vis Sci*, 2005. Abstract only.

[73] B. Hermann, C. Torti, E. J. Fernandez, et al. Towards in vivo imaging of photoreceptor morphology and function. In *Biomedical Optics*, 2008. Abstract only.

[74] W. Drexler, U. Morgner, R. K. Ghanta, et al. Ultrahigh–resolution ophthalmic optical coherence tomography. *Nat Med*, 7(4):502–507, 2001.

[75] W. Drexler. Where is retinal optical coherence tomography heading? SPIE Newsroom, 2009. (Last accessed on 7 Feb 2011 at http://spie.org/x34613.xml?ArticleID=x34613).

[76] R. J. Zawadzki, S. S. Choi, A. R. Fuller, et al. Cellular resolution volumetric in vivo retinal imaging with adaptive optics optical coherence tomography. *Optics Express*, 17(5):4084–4094, 2009.

[77] D. T. Miller. Retinal imaging and vision at the frontiers of adaptive optics. *Physics Today*, 53(1):31–36, 2000.

[78] J. Rha, R. S Jonnal, et al. Adaptive optics flood–illumination camera for high speed retinal imaging. *Optics Express*, 14(10):4552–4569, 2006.

[79] R. S. Jonnal, J. R. Besecker, et al. Imaging outer segment renewal in living human cone photoreceptors. *Optics Express*, 18(5), 2009.

[80] E. Dalimier. *Adaptive Optics Correction of Ocular Higher–Order Aberrations and the Effects on Functional Vision.* PhD thesis, Department of Experimental Physics, NUI, Galway, Ireland, 2007.

[81] K. M. Hampson, C. Paterson, et al. Adaptive optics system for investigation of the effect of the aberration dynamics of the human eye on steady–state accommodation control. *J. Opt. Soc. Am. A*, 23(5):1082–1088, 2006.

[82] C. Torti, B. Povazay, B. Hofer, et al. Adaptive optics optical coherence tomography at 120,000 depth scans/s for non–invasive cellular phenotyping of the living human retina. *Optics Express*, 17(22):19382–19400, 2009.

[83] M. Mujat, R. D. Ferguson, A. H. Patel, et al. High resolution multimodal clinical ophthalmic imaging system. *Optics Express*, 18(11):11607–11621, 2010.

[84] S. Martinez-Conde, S. L. Macknick, and D. Hubel. The role of fixational eye movements in visual perception. *Nature Reviews Neuroscience*, 5:229–240, 2004.

[85] D. Sliney, D. Aron-Rosa, et al. Adjustment of guidelines for exposure of the eye to optical radiation from ocular instruments: statement from a task group of the international commission on non–ionizing radiation protection. *Applied Optics*, 44(11):2162–2176, 2005.

[86] A. Charman, A. Hartwig, et al. Accommodation of myopes and emmetropes to peripheral stimuli. In *5th European Meeting on Visual and Physiological Optics*, 2010. Abstract only.

[87] R. T. Kintz and R. F. Witzel. Role of eye movements in the perception of apparent motion. *JOSA*, 62(10):1237–1238, 1972.

[88] A. Hartwig, E. Gowen, et al. Eye movements in myopes and non–myopes for near vision tasks. In *5th European Meeting on Visual and Physiological Optics*, 2010. Abstract only.

[89] R. M. Prichard. Stabilized images on the retina. *Sci. Am.*, 204:72–78, 1961.

[90] Z. M. Hafed, L. Goffart, and R. J Krauzlis. A neural mechanism for microsaccade generation in the primate superior colliculus. *Science*, 323:940–943, 2009.

[91] D. Richardson and M. Spivey. *Encyclopedia of Biomaterials and Biomedical Engineering, Eye Tracking: Characteristics and Methods*, chapter Eye Tracking: Characteristics and Methods. Informa Healthcare, 2008.

[92] C. Morimoto and M. Mimica. Eye gaze tracking techniques for interactive applications. *Computer vision and image understanding*, 98:4–24, 2005.

[93] D. Li, J. Babcock, and D. Parkhurst. Openeyes : A low cost head mounted eye–tracking solution. In *Proc. Eye Tracking Research and Applications*, pages 95–100, 2006.

[94] J. Agustin and A. Villanueva. Pupil brightness variation as a function of gaze direction. In *Proc. Eye Tracking Research and Applications*, page 49, 2006.

[95] A. Haro and M. Flickner. Detecting and tracking eyes by using their physiological properties, dynamics and appearance. In *Proc. IEEE Conference on Computer Vision and Pattern Recognition*, pages 163–168, 2000.

[96] Z. Zhu and Q. Ji. Combining Kalman filtering and mean shift for real time eye tracking under active IR illumination. In *Proc. IEEE International Conference on Pattern Recognition*, 2002.

[97] K. Schreiber and T Haslwanter. Improving calibration of 3–D video oculography systems. In *IEEE Trans. Biomed. Eng.*, volume 51, pages 676–679, 2004.

[98] N. A. Zabaronik. Eye tracking using fiber optics and computer vision techniques. Master's thesis, Bradley Department of Electrical Engineering Virginia Polytechnic Institute and State University, 1997.

[99] C. Hennesey, B. Noureddin, and P. Lawrence. A single camera eye–gaze tracking system with free head motion. In *Proc. Eye Tracking Research and Applications*, 2006.

[100] Z. Zhu, F. Fujimura, and J. Qiang. Real–time eye detection and tracking under various light conditions. In *Proc. Eye Tracking Research and Applications*, pages 139–144, 2002.

[101] J. Hiley and A. Redekopp. A low cost human computer interface based on eye tracking. In *Proc. IEEE Engineering in Medicine and Biology*, pages 3226–3229, 2006.

[102] T. Ohno. One point calibration gaze tracking method. In *Proc. Eye Tracking Research and Applications*, page 34, 2006.

[103] A. Talukder, J. M. Morookian, S. Monacos, et al. Eye–tracking architecture for biometrics and remote monitoring. *Applied Optics*, 44(5):693–700, 2005.

[104] J. Zhu and J. Yang. Subpixel eye gaze tracking. In *Proc. IEEE Automatic Face and Gesture Recognition*, page 131, 2002.

[105] A. Villanueva et al. Eye tracking system model with easy calibration. In *Proc. Eye Tracking Research and Applications*, page 55, 2004.

[106] T. Ohno, N. Mukawa, and A. Yoshikawa. FreeGaze: a gaze tracking system for everyday gaze interaction. In *Proc. Eye Tracking Research and Applications*, pages 125–132, 2002.

[107] T. Ohno and N. Mukawa. A free–head, simple calibration, gaze tracking system that enables gaze–based interaction. In *Proc. Eye Tracking Research and Applications*, pages 115–122, 2004.

[108] X. Lin and J. Craig. Accurately measuring the size of the pupil of the eye. http://www.citr.auckland.ac.nz/techreports/2003/CITR-TR-127.pdf, 2003. (Last accessed 12 December 2010).

[109] I. Miro, N. Lopez-Gil, and P. Artal. Pupil–meter and tracking system based in a fast image processing algorithm. In *Proc. SPIE*, volume 3591, pages 63–70, 1999.

[110] N. Patton, T. M Aslam, T. MacGillivray, et al. Retinal image analysis: Concepts, applications and potential. *Progress in Retinal and Eye Research*, 25:99–127, 2006.

[111] D. X. Hammer, R. D. Ferguson, C. E. Bigelow, et al. Adaptive optics scanning laser ophthalmoscope for stabilized retinal imaging. *Optics Express*, 14(8):3354–3367, 2006.

[112] A. Podoleanu. Combinations of techniques in imaging the retina with high resolution. *Progress in Retinal and Eye Research*, 27:464–499, 2008.

[113] A. Garcia-Rissmann, C. Kulcsar, et al. Adaptive prediction of human eye pupil position and effects on wavefront errors. In *Proc. of SPIE*, volume 7885, 2011.

[114] L. Diaz-Santana, C. Torti, et al. Benefit of higher closed loop bandwidths in ocular adaptive optics. *Optics Express*, 11(20):2597–2605, 2003.

[115] A. Mira-Agudelo, L. Lundstrom, and P. Artal. Temporal dynamics of ocular aberrations: monocular vs binocular vision. *Ophthal. Physiol. Opt.*, 29:256–263, 2009.

[116] A. Guirao, I. G. Cox, and D. R. Williams. Effect of rotation and translation on the expected benefit of an ideal method to correct the eye's higher order aberrations. *J. Opt. Soc. Am. A*, 18(5):1003–1015, 2001.

[117] A. Guirao, I. G. Cox, and D. R. Williams. Method for optimizing the correction of the eye's higher–order aberrations in the presence of decentrations. *J. Opt. Soc. Am A*, 19(1):126–128, 2002.

[118] E. Moreno-Barriuso et al. Ocular aberrations before and after myopic corneal refractive surgery: Lasik induced changes measured with laser ray tracing. *Inves. Ophthal. Vis. Sci.*, 42(6):1396–1403, 2001.

[119] S. G. Rosolen, B. Lamory, F. Harms, et al. Cellular–resolution in vivo imaging of the feline retina using adaptive optics: preliminary results. *Veterinary Ophthalmology*, 13(6):369–376, 2010.

[120] M. Zacharria. The eyes have it-adaptive optics approaches clinical ophthalmology. *BioOptics World*, 1(6):22–26, 2008.

[121] M. Zacharria, B.Lamory, and N. Chateau. Biomedical imaging: New view of the eye. *Nature Photonics*, 5(1):24–26, 2011.

[122] C. Viard, K. Nakashima, B. Lamory, et al. Imaging microscopic structures in pathological retinas using a flood–illumination adaptive optics retinal camera. In *Proc. SPIE*, volume 7885, 2011.

[123] ISO 15004-2. Ophthalmic instruments - Fundamental requirements and test methods - Part 2: Light hazard protection, 2007.

[124] N. Devaney, E. Dalimier, et al. Correction of ocular and atmospheric wavefronts: a comparison of the performance of various deformable mirrors. *Applied Optics*, 47(35):6550–6562, 2008.

[125] C. Paterson, I. Munro, and J. C. Dainty. A low cost adaptive optics system using a membrane mirror. *Optics Express*, 6(9):175–185, 2000.

[126] E. Dalimier and J. C. Dainty. Comparative analysis of deformable mirrors for ocular adaptive optics. *Optics Express*, 13(11):4275–4285, 2005.

[127] E. Odlund, H. F. Raynaud, and others. Control of an electromagnetic deformable mirror using high speed dynamics characterization and identification. *Applied Optics*, 49(31):G120–G128, 2010.

[128] A. Gomez-Vieyra and D. Malacara-Hernandez. Geometric theory of wavefront aberrations in an off–axis spherical mirror. *Applied Optics*, 50(1):66–73, 2011.

[129] A. Dubra, A. Gomez-Vieyra, D. Malacara-Hernandez, et al. First–order design of off–axis reflective ophthalmic adaptive optics systems using afocal telescopes. In *OSA-FiO*, 2009.

[130] W. H. Southwell. Wavefront estimation from wavefront slope measurements. *J. Opt. Soc. Am.*, 70(8):998–106, 1980.

[131] W. H. Press. Flicker noises in astronomy and elsewhere. *Comments Astrophys.*, 7(4):103–119, 1978.

[132] A. L. Goldberger, L. A. N. Amaral, et al. Fractal dynamics in physiology: alterations with disease and aging. *Proc. Natl. Acad. Sci. U.S.A.*, 99(3):2466–2472, 2002.

[133] P. Bak, C. Tang, and K. Wiesenfield. Self–organized criticality: an explanation of 1/f noise. *Phys. Rev. Let.*, 59(4):381–384, 1987.

[134] M. Wolf. 1/f noise in the distribution of prime numbers. *Physica A*, 241:493–499, 1997.

[135] E. Milotti. 1/f noise: a pedagogical review. *Arxiv preprint physics*, 0204403, 2002. arxiv.org.

[136] W. Ro and Y. Kwon. 1/f noise analysis of songs in various genre of music. *Chaos, Solitons and Fractals*, 42:2305–2311, 2009.

[137] A. L. Goldberger. Nonlinear dynamics, fractals, and chaos theory: Implications for neuroautonomic heart rate control in health and disease. http://www.anatomiafractal.com, 2000. (Last accessed 5 April 2011).

[138] P. C. Ivanov, L. A. N. Amaral, et al. From 1/f noise to multifractal cascades in heartbeat dynamics. *Chaos*, 11(3):641–652, 2001.

[139] P. C. Ivanov, L. A. N. Amaral, A. L. Goldberger, et al. Multifractality in human heartbeat dynamics. *Nature*, 399:461–465, 1999.

[140] B. J. West and M. F. Shlesinger. On the ubiquity of 1/f noise. *International Journal of Modern Physics B*, 3(6):795b–819, 1989.

[141] A. Eke, P. Herman, et al. Fractal characterization of complexity in temporal physiological signals. *Physiol. Meas.*, (23):R1–R38, 2002.

[142] L. Rosenberg, V. Punia, et al. The spontaneous vertical movements seen during fixation are chaotic. In *The Association for Research in Vision and Ophthalmology Annual Meeting*, 2010. Abstract only.

[143] P. J. Hampton, P. Agathoklis, et al. Closed–loop control of a woofer–tweeter adaptive optics system using wavelet–based phase reconstruction. *J. Opt. Soc. Am. A*, 27(11):A145–A156, 2010.

[144] S. Monirabbasi and S. Gibson. Adaptive control in an adaptive optics experiment. *J. Opt. Soc. Am. A*, 27(11):A84–A96, 2010.